Molecular Dynamics Simulation of Thin Film Liquid Boiling over Nanostructured Surfaces under Different Wetting Conditions

by

Sheikh Mohammad Shavik

A Thesis Submitted in Partial Fulfillment of the Requirements for the Degree of

MASTER OF SCIENCE IN MECHANICAL ENGINEERING

Department of Mechanical Engineering
BANGLADESH UNIVERSITY OF ENGINEERING AND TECHNOLOGY
Dhaka-1000, Bangladesh

July 2015

The thesis titled "**Molecular Dynamics Simulation of Thin Film Liquid Boiling over Nanostructured Surfaces under Different Wetting Conditions",** submitted by **Sheikh Mohammad Shavik,** Student no: 0412102032 P, Session: April, 2012 has been accepted as satisfactory in partial fulfillment of the requirement for the degree of MASTER OF SCIENCE IN MECHANICAL ENGINEERING on July 14, 2015.

BOARD OF EXAMINERS

1. ---------- Chairman

Dr. Mohammad Nasim Hasan
Associate Professor
Department of Mechanical Engineering
Bangladesh University of Engineering and Technology (BUET)
Dhaka-1000, Bangladesh.

2. ---------- Member

Dr. Md. Zahurul Haq (Ex-officio)
Professor
Department of Mechanical Engineering
Bangladesh University of Engineering and Technology (BUET)
Dhaka-1000, Bangladesh.

3. ---------- Member

Dr. A.K.M. Monjur Morshed
Assistant Professor
Department of Mechanical Engineering
Bangladesh University of Engineering and Technology (BUET)
Dhaka-1000, Bangladesh.

4. ---------- External

Dr. Md. Abdur Razzak Akhanda
Professor
Department of Mechanical and Chemical Engineering
Islamic University of Technology (IUT)
Gazipur, Bangladesh.

CANDIDATE'S DECLARATION

It is hereby declared that this thesis or any part of it has not been submitted elsewhere for any degree or diploma.

Sheikh Mohammad Shavik

Dedicated to My Parents

ACKNOWLEDGEMENT

I am greatly thankful to my supervisor, Dr. Mohammad Nasim Hasan, for all the time and efforts he has put in towards mentoring my dissertation work. I am indebted to him for his invaluable guidance, support and encouragement. This dissertation would not have been possible without guidance and help of him. His dedication and hard work towards the research will be an everlasting source of inspiration for me.

I express my sincere gratitude to Dr. A. K. M. Monjur Morshed for his precious advice and recommendations which have helped tremendously to improve this work.

I would like to thank the members of my thesis evaluation committee, Dr. Md. Abdur Razzak Akhanda, Dr. Md. Zahurul Haq and Dr. A.K.M. Monjur Morshed for their valuable comments and suggestions.

My utmost appreciation goes to my parents and family for their endless love and support which I have been blessed with in my life.

ABSTRACT

Molecular dynamics (MD) simulations have been performed to investigate the boiling phenomena of thin liquid film adjacent to a solid surface with particular emphasis on (i) the effect of material and wetting condition of the solid surface, and (ii) the effect of nanostructures under various surface wetting conditions. The molecular system consists of liquid and vapor argon, and solid wall. To examine the effect of surface material on boiling phenomena, three different solid materials have been considered which are platinum, silver and aluminum. The solid-liquid interfacial wettability, in other words whether the solid surface is hydrophilic or hydrophobic has been altered for different cases to examine its effect on boiling phenomena. To explore the effect of the nanostructures along with the surface wettability, nanostructures having the shape of rectangular block have been considered in this study and the height of the nanostructures has been altered for both hydrophilic and hydrophobic cases. The initial configuration of the simulation domain was equilibrated at 90 K and after equilibrium period, the wall temperature was suddenly increased to 130 K to resemble the evaporation of thin liquid film, while in another case it was set to 250 K (which is far above the critical point of argon) to initiate rapid or explosive boiling. The spatial and temporal variation of temperature and density as well as the variation of system pressure and energy with respect to time were closely monitored for each case. The heat flux normal to the solid surface was also calculated to illustrate the effectiveness of heat transfer under different cases. The results show that the wetting condition of surface has significant effect on both the normal and explosive boiling of the thin liquid film rather than surface material. The surface with higher wettability i.e. hydrophilic condition provides more favorable situation for boiling than the low-wetting surface (hydrophobic) and therefore, liquid argon responds quickly and shifts from liquid to vapor phase faster in case of hydrophilic surface. The change of system energy in case of evaporation after the increase of wall temperature from 90 K to 130 K were almost same for both hydrophilic and hydrophobic surface. Similarly, for explosive boiling case the jump of energy was same regardless of surface wetting condition but larger in magnitude. In conjunction with the wettability of the surface, the height of the nanostructures has significant effect on boiling phenomena. The magnitude of heat flux during the evaporation of the thin film liquid has been found to be in the same order of magnitude of the theoretical maximum value of heat flux as defined by Gambill and Lienhard [47]. But in case of explosive boiling, it was one order of magnitude greater than the theoretical maximum value of heat flux.

NOMENCLATURE

a_i	acceleration of atom i (eV.mole/gm.Å)
E	Energy (eV)
F_i	force of atom i (eV/Å)
k_b	Boltzmann constant (eV/K)
m_i	mass of atom i (gr/mole)
N	number of atoms
P	pressure (bar)
$q_{max,max}$	theoretical maximum heat flux (W/m^2)
r_{cut}	cut-off distance (Å)
r_i	position of atom i (Å)
r_{ij}	distance between molecule i and j (Å)
t	time (ps)
T	temperature (K)
v_i	velocity of atoms (Å/ps)
V	Volume ($Å^3$)
x	coordinate in x-direction
y	coordinate in y-direction
z	coordinate in z-direction

Greek Symbols

ε	energy parameter of LJ potential (eV)
κ	thermal conductivity (W/mK)
σ	length parameter of LJ potential (Å)
φ	short range potential energy (eV)
Φ	interaction potential (eV)

Subscripts

Ag	Silver
Al	Aluminum
Ar	Argon
Pt	Platinum
Kin	kinetic
Pot	potential
Tot	total

TABLE OF CONTENTS

LIST OF FIGURES

LIST OF TABLES

CHAPTER-1

INTRODUCTION

1.1 Background

Boiling is an important phase change phenomenon which has the potential advantage of being able to transfer a large amount of energy over a relatively narrow temperature range and thus, it is used in many engineering applications such as jet impingement quenching[1-2], formation of carbon dioxide bubbles on the anode of direct methanol fuel cells [3-4]; microfluidic devices such as bubble jet printing heads [5-7], valves [8], mixing in microfluidic channels induced by collapsing bubbles created by using a light absorbing fluid and a laser [9], and pumps [10]; sonoluminescence [11-12]; cooling of CPU's [13-15] and so on. It is defined as the process of change of phase from liquid to vapor by heating the liquid past its saturation temperature and is characterized by nucleation, growth and detachment of the vapor bubbles. As boiling process involves phase change and two phase systems, it is difficult to understand and control because of the multiple time and length scales that are involved with the nucleation process. Nucleation of a new phase occurs on atomic length scales and relatively short time scales (nanoscale), while the growth of the nuclei and their interaction with the rest of the system can occur on much larger length and time scales (miliscale).

1.1.1 Thin Film Evaporation

It has been widely reported in literature that the contact line at the base of the bubble in nucleate boiling can be divided into macro- and micro-regions. The micro region is the ultrathin liquid film between the solid surface and the evolving liquid-vapor interface. The macro region is the region occupied by vapor and liquid, except the micro-layer. The micro-region can be subdivided into two additional regions. Thus the three regions, as shown in Fig. 1.1, are:

a) Non-evaporating thin-film region – liquid is adsorbed on the heater surface and forms a non-evaporating layer with molecular forces having controlling influence.

b) Evaporating thin-film region – maximum evaporation and heat transfer occurs in this region and the liquid is fed in this region from the bulk liquid through the intrinsic meniscus region.

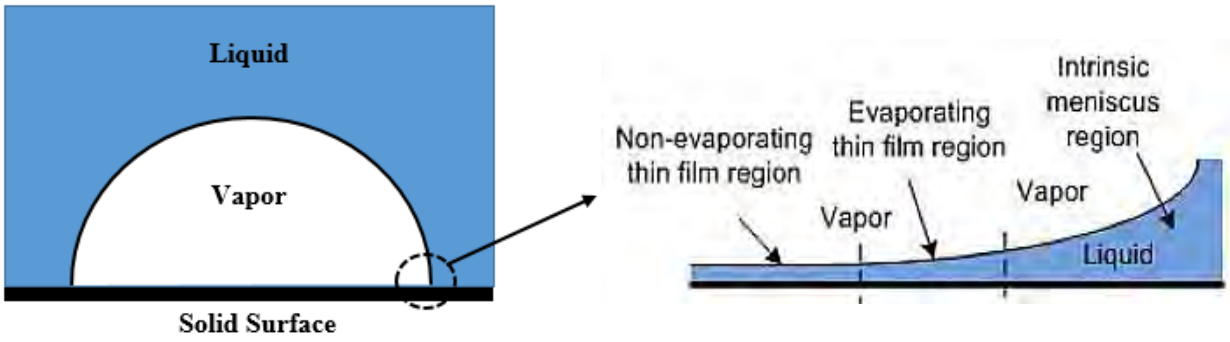

(a) (b)

Fig. 1.1. Schematic of bubble growth, (a) overall picture at macro-scale (shaded region depicts the area covered by non-evaporating thin film), and (b) zoomed in nano- and micro-scale regions at the three-phase contact line.

c) Intrinsic meniscus region – fluid mechanics in this region is governed by the conventional equation of capillarity.

There is a region between the non-evaporating thin film region and the evaporation thin film region over which the film varies in thickness and curvature to accommodate the transition between the two regions. This is called the interline region and is the thinnest portion of the meniscus over which vaporization can occur. Since it is the thinnest, it is also the location where the evaporation rate is the highest.

1.1.2 Explosive Boiling

Explosive boiling [16] is a special kind of boiling in which the phase transition from liquid to vapor occurs very rapidly. When the liquid is superheated to a degree much higher than the normal saturation temperature and approaching the thermodynamic critical temperature, homogeneous vapor bubble nucleation takes place at an extremely high rate, which lead to the near-surface region of the materials being ejected rapidly. There are a lot of special characteristics in explosive boiling, such as a high degree of superheat, explosive bubble nucleation and growth, bubble clusters formed by tiny bubbles and pressure shock wave in an extreme condition. The explosive boiling is also referred to as rapid boiling, vapor explosion,

phase flashing, thermal detonation, and rapid phase transitions. This phenomena is encountered in many newly emerging technologies in nuclear and chemical industries such as nano electromechanical systems, nano electronic cooling, laser surgery and laser steam cleaning of a solid surface, refrigeration, cryogenics, colloidal deposition on surface and so on [17-20].

1.1.3 Boiling over Nanotextured Surfaces

Nanotextured surfaces are defined as the surfaces covered with nano-sized structures. Nanostructures are an attractive option for researchers in the field of phase change heat transfer as use of nanostructured surface is a very effective method for enhancing boiling heat transfer. The development of nanoscience and nanotechnology has been exponentially increasing in the last twenty years and fast advancement of nanofabrication technology allows us to manufacture different kinds of novel nano-patterns on a flat surface. The most significant consequence of the nanostructures is the tremendous increase of surface area per unit volume of the object. Therefore, nanostructures significantly change the behavior of boiling due to the high surface-to-volume ratio in the system. Although these effects cause enhancement of heat transfer [21- 22] and change the wettability at liquid-solid interface [23-24], from a macroscopic point of view, nanostructures are kind of ultra-flat surfaces because their roughness are in nanoscale. However, due to the complexity of physical mechanism in the nanoscale, the difference between heat transfer mechanisms at macro scale and nanoscale is not fully understood so far. Geometry and size of nano-patterns are two of the main factors that generally affect the characteristics of boiling phenomena. Thus, many scientists and researchers are paying tremendous attention to the field of nanoscale heat transfer now-a-days to reveal its effect on characteristics of boiling phenomena.

1.1.4 Molecular Dynamics (MD) Simulation

As mentioned in the previous sections, because of its extensive applications in many engineering fields, boiling heat transfer phenomena has been studied extensively during the last few decades which include experimental work, and theoretical models to predict the exact nature of boiling in various conditions. Since the boiling process is very complex, its complete understanding still poses significant challenges and researchers have not converged on a definite precise model. Moreover, classical macroscopic theories based on thermodynamics cannot be used to describe the behavior of the bubble nucleation which

occurs at the molecular level in cases where nanostructures are involved in boiling phenomena especially in case of explosive boiling phenomena. Also, due to the very small scale, several difficulties occur in accurate experimentation of explosive boiling [25-26] and thus empirical correlations obtained from many experimental studies cannot sufficiently predict the characteristics of explosive boiling phenomena. Consequently, in recent times, researchers concentrated more on atomistic simulations to investigate the complex and highly non-equilibrium process of evaporation and explosive boiling in nanoscale. Non equilibrium molecular dynamics simulation (NEMD) has been popularly used to explore such phenomena. Recent studies involving Molecular Dynamics (MD) simulation of evaporation and explosive boiling are discussed later in literature review (Chapter-2).

1.2 Motivation of the Research

Many non-equilibrium molecular dynamics studies have been performed in the past to understand the behavior of the homogeneous and heterogeneous phase transition or nucleation of thin liquid layer [27-30, 34]. More recent studies focused on study of evaporation and explosive by involving nanostructures of different sizes and shapes to investigate its effect on boiling phenomena [40-42].These studies confirmed the significant effect of size and shape of the nanostructures on evaporation and explosive boiling. Along with the nanostructures, the study of the surface effects like change of solid-liquid surface wettability and surface material can add new dimensions to this research. Only a few of the previous studies performed by NEMD simulation in literature are found to be concerned with the effect of surface material and wettability on boiling phenomena. Therefore, in the present study, (i) the effect of surface material and wettability, (ii) effect of nanostructures and surface wettability on evaporation and explosive boiling have been closely investigated by NEMD simulation.

A very important factor in case of heat transfer phenomena is the heat flux. Among previous NEMD simulation studies, only a handful reported the values of heat flux evaluated during the evaporation and explosive boiling. The present study predicts the values of heat flux in case of both evaporation and explosive boiling for different cases which provides some useful comparative information and these values also found to be consistent with the theoretical model as predicted by Gambill and Lienhard [47].

1.3 Research Objectives

In the present study, by non-equilibrium molecular dynamics simulation (NEMD) explosive boiling of thin liquid argon film over solid surface has been carried out with (i) different solid surface material, (ii) different patterns of the nanostructure and (iii) different surface wettability. Based on surface wettability two cases are considered such as hydrophilic and hydrophobic. Flat platinum, silver and aluminum surface is considered to study the effect of surface material associated on boiling phenomena. Three different heights of rectangular shaped nanostructures are taken into account to assess the effect of nanostructure height along with the surface wetting condition on phase transition and other associated phenomena during evaporation and explosive boiling.

The specific objectives and outcome of the research work are as follows:

i. To develop a molecular model that represents the atomic structure of a three phase molecular system involving solid wall, liquid and vapor argon atoms.

ii. To validate the developed model by establishing thermal equilibrium for the molecular system by monitoring the various thermodynamic and transport properties (e.g. temperature, pressure, density, system energy, thermal conductivity etc.).

iii. To simulate the system for exploring the evaporation and explosive boiling of thin liquid argon film considering different solid-solid and solid-liquid interaction potentials.

iv. To reveal the characteristics of phase change phenomena by observing the temporal variation of pressure, temperature, system energy and net evaporation number of argon as well as the spatial distribution of temperature and number density of argon atoms for different solid-solid and solid-liquid interaction potentials.

v. To closely investigate the heat transfer characteristics for different solid-solid and solid-liquid interaction potentials by evaluating the wall heat flux for different cases of the study and to compare it with ultimate limit of maximum heat flux, $q_{max,max}$ as suggested by Gambill and Lienhard [47].

vi. To explore the effect of surface wettability and nanostructures embedded on flat surface on explosive boiling of thin liquid argon film.

1.4 Thesis Outline

The present thesis focuses on the study of evaporation and explosive boiling of thin liquid film over a nanostructured surface by molecular dynamics simulation considering the effect of the different surface material and surface wetting conditions. An outline of this thesis is presented below,

Chapter- 1: Introduction – a discussion about the key elements of this research, motivation behind this research work, and research objectives.

Chapter- 2: Literature Review – an account of previous research about molecular dynamics simulation on boiling phenomena.

Chapter- 3: Molecular Dynamics Simulation – a description of basic elements of molecular dynamics simulation, essentials of the simulator (LAMMPS) that is used in this study,

Chapter- 4: Results and Discussion – describes the simulation model of the present study, validation of the model and discussion about the results of the study.

Chapter- 5: Conclusion and Future Work – summarizes the outcomes of the current research and provides a framework about the future direction of this research.

CHAPTER-2

LITERATURE REVIEW

2.1 Introduction

Many researchers in the past have focused on revealing the characteristics of boiling phenomena which includes homogeneous and heterogeneous nucleation processes, evaporation and explosive boiling by atomistic simulation particularly, in recent years by performing non equilibrium molecular dynamics (NEMD) simulation. Molecular dynamics simulation has been a very effective method to investigate such phenomena in the nanoscale range or atomistic view point. Previously, in many molecular dynamics studies, researchers have given intensive focus on various issues of phase change process. In this section, relevant research works and their outcomes are discussed to provide an illustration of the contemporary molecular dynamics study on boiling phenomena.

2.2 Research on Homogeneous and Heterogeneous Nucleation

Homogeneous and heterogeneous nucleation have long been studied by the researchers both experimentally and numerically. In past two decades, molecular dynamics method has become a well-accepted method to study these phenomena from a nanoscale point of view.

Yasuoka and Matsumoto carried out the direct MD simulations of the nucleation process for Lennard-Jones liquid and water molecules [27, 28]. They found the nucleation rate and cluster size and observed that nucleation rate is seven orders of magnitude larger than the prediction of a classical nucleation theory for Lennard-Jones fluid.

Kinjo and Matsumoto [29] carried out molecular dynamics simulations of a Lennard‐Jones fluid under negative pressure to investigate the inception of vapor phase in the liquid (i.e.,

cavitation) and properties of liquid under negative pressure. From their study they found that the system reaches a kinetic limit of metastability at some stages and the nucleation rate calculated was eight orders of magnitude larger than that predicted by the classical nucleation theory.

Kimura and Maruyama [30] simulated heterogeneous nucleation of argon liquid droplet on a solid surface modeled as a constant temperature heat bath using phantom molecules. They observed nucleation rate, critical nucleus size and free energy needed for cluster formation were not much different from the prediction of the classical heterogeneous nucleation theory in case of smaller cooling rate but the discrepancy became considerable with the increase of cooling rate.

Nagayama et al. [31] carried out MD simulations to examine the bubble behavior confined in a nanochannel with emphasis on nucleation phenomenon. A metastable liquid confined in a nanochannel with an inlet driving force was simulated. Nano-sized bubbles were observed at different conditions of solid–liquid interfacial wettability. The authors also found that the vapor pressure inside the nano-bubble disagrees with the macroscopic Young–Laplace equation.

Sekine et al. [33] simulated liquid-vapor nucleation of Lennard-Jones fluid by molecular dynamics method for understanding the initial stage of process such as cavitation, boiling and phreatic explosion and calculated the nucleation rate at three different temperatures by survival probability of the bubble-free state. The results show that the nucleation rate was seven to nine orders of magnitude greater than that estimated by the classical nucleation theory and the ratio of the nucleation rate obtained by molecular simulation to that as predicted by the classical theory depends on the temperature.

Novak et al. [34] studied the homogeneous and heterogeneous bubble nucleation of Lennard Jones liquid using molecular dynamics simulation. They observed a clear enhancement in nucleation rate for heterogeneous cases compared to homogenous cases and also found that void formation was favored as the attraction between the liquid and solid was decreased.

2.3 Research on Evaporation and Explosive Boiling on Flat Surface

Yu and Wang [32] performed molecular dynamics simulation for understanding the evaporation process of thin liquid film near the triple-phase contact line. They evaluated the

net mass flux and compared it with Hertz–Knudsen–Schrage equation which is based on kinetic theory of gases (KTG). In their study, they found a very thin non-evaporating layer in case of evaporation and compared it with theoretical models.

Wu and Pan [35] simulated a thin argon film evaporation on a Pt surface in vacuum. Their model did not include the step wall temperature jump. They obtained the evaporation/condensation coefficient, and noticed mean temperature for the interface region to be 2–3 K lower than that inside the liquid. Also the evaporation heat transfer coefficient was very high which demonstrates very high heat transfer capability of evaporation from an ultra-thin liquid film.

Yi et al. [36] studied the evaporation of a thin liquid argon layer on a Pt surface in an argon vapor atmosphere. The Pt surface was modeled as constant temperature using the Langevin thermostat. The wall was heated to two temperatures of 150 K and 300 K, respectively, from an initial equilibrium temperature of 110 K. In the former case a gradual evaporation of the liquid film occurred, while in the latter the Leidenfrost phenomenon was observed. In both the cases, a complete evaporation of the liquid film was obtained.

Gu et al. [37] studied the explosive boiling of thin liquid-argon on a metal surface. For thin films with thickness below seven monolayers, the liquid argon completely is vaporized and dissolved into a mixture of small clusters, while for higher film thickness only the Ar layers near to the surface were vaporized.

Yamamoto and Matsumoto [38] studied the initial stage of nucleate boiling of Lennard-Jones liquid on ideally smooth surface using molecular dynamics simulation. They examined two cases, the overall heating where the surface temperature was kept constant all over the area, and the partial (spot) heating where two regions of heating and cooling are placed and revealed that nucleation is possible from the smooth surface without the presence of preexisting nuclei. Also the inception time of nucleation was found to be affected by surface wettability as well as the surface temperature.

Maroo and Chung [39] performed molecular dynamics simulation of platinum heater and associated nano-scale liquid argon film evaporation and colloidal adsorption characteristics. They showed that both evaporation and heat flux rates exponentially decreased with time. With increasing the height of nanochannel, both net heat and evaporation fluxes increase.

Zou et al. [62] studied the energy conversion in the homogeneous nucleation processes of the explosive boiling induced by laser heating considering liquid nitrogen and water as the working fluid by molecular dynamics simulation. They found that, the influence of the heat quantity on the energy conversion of liquid nitrogen is the same in trend as that of water and the influence of the initial equilibrium temperature and the area of the heating zone on the liquid nitrogen is less than that of water.

Mao and Zhang [63] used molecular dynamics simulation to study the rapid boiling of liquid water film heated by a hot copper plate in a confined space and observed that liquid water molecules close to the plate are instantly overheated and undergo a rapid phase transition. They also detected a non-vaporization molecular layer, with a constant density of 0.2 g/cm 3, tightly attached to the surface of the plate.

Dou et al. [64] investigated the separation of water films adjacent to a hot metal surface by molecular dynamics simulation. They observes that the water layers nearest to the surface overheat and undergo explosive boiling and for thick films, the expansion of the vaporized molecules near the surface forces the outer water layers to move away from the surface.

Abovementioned studies were performed particularly to understand the behavior of the phase transition of thin liquid film during evaporation and explosive boiling on a flat solid surface.

2.4 Research on Evaporation and Explosive Boiling on Nanostructured Surface

In recent experimental and numerical studies on explosive boiling, it has been confirmed that the rate of heat transfer during the phase transition can be significantly increased if nanostructures are embedded over the flat solid surface. Both the geometry and the size of the nanostructures have great effect on boiling phenomena. Therefore, a number of research have already been done involving different shape and size of the nanostructures to study its effect on explosive boiling. Majority of these studies are computer simulation particularly non equilibrium molecular dynamics simulation.

Morshed et al. [40] studied the effect of nanostructures on evaporation and explosive boiling of thin liquid argon films over platinum wall through molecular dynamics simulation. They considered cylindrical nanoposts and found that heat transfer during explosive boiling is significantly affected by size of the nanoposts. A non-evaporating layer was found for the

low temperature case when evaporation occurred, but for high temperature case explosive boiling occurred with no trace of non-evaporating layer.

Seyf and Zhang studied the effect of spherical nanostructures [41] as well as conical nanostructures [42] on explosive boiling of argon. Their studies also confirmed the significant effect of size and shape of the nanostructures on explosive boiling. In the later study, they also considered the effect of solid surface material and found that the boiling phenomena is not much sensitive to the type of surface materials.

2.5 Research Focused on the Surface Wettability

Along with the effect of nanostructure, the study of the surface effects like change of solid-liquid surface wettability accompanied with nanostructures can add new dimensions to this research. On the basis of solid-liquid surface wettability, surfaces are frequently termed as hydrophilic or hydrophobic. (Though by definition these two terms refer to water as the liquid but in previous literature the term ‘hydro’ has been frequently used in cases of other liquids as well [31, 38, 45]). The nature of solid surface (hydrophilic or hydrophobic) has great effect on explosive boiling. Some studies concerned with the surface wettability have also been performed.

Maruyama and Kimura [43] simulated a heterogeneous nucleation of argon vapor bubble on a solid Pt surface and measured the apparent contact angle. Liquid argon was placed between parallel solid platinum surfaces. Volume of the system was gradually expanded until a vapor bubble was nucleated. The wettability of the lower surface was varied by changing the potential parameter between argon and solid molecule.

Park et al. [44] studied formation of bubble using molecular dynamics with the liquid initially in metastable condition. Solid surfaces were not included in this simulation. The surface tension of the bubble, calculated from the density profile and from the normal and transverse components of pressure tensor, was found to increase very slightly with decrease of bubble radius.

Nagayama et al. [45] performed NEMD simulations to study the effect of the interface wettability on the pressure driven flow of a Lennard-Jones (LJ) fluid in a nanochannel. They found that the non-uniform temperature and pressure profiles near the solid walls are owing to the effect of interface wettability.

Hens et al. [46] performed MD simulation of liquid argon film to understand the mechanism of bubble nucleation with particular emphasis on surface texture. They considered hydrophilic, neutral and hydrophobic flat solid platinum surface and found that the boiling phenomena is considerably affected by the surface wettability.

CHAPTER 3

MOLECULAR DYNAMICS SIMULATION

3.1 Introduction

Usually, molecular dynamics (MD) refers to the computational method that calculates statistical properties of an ensemble of particles by tracking the trajectories of each particle in the system. This idea is a combination of the old mechanistic tradition dating back to Pierre Simon de Laplace and the new concept of atoms (as well as molecules) revealed at the beginning of the 20th century. The molecular dynamics method began to thrive with the development of modern computers, first in the studies of equilibrium properties of liquid composed of hard spheres [48, 49], while today it is applied in various disciplines from physics to biology [50]. Since the molecular dynamics method is often used as a digital experiment or simulation of real materials and systems, it is often known as the molecular dynamics "simulation".

In the past, the researchers by modeling and simulating the physical phenomena by various numerical methods have studied many problems of fluid mechanics and heat transfer. These works predominantly solved the Navier-Stokes and Energy Equation and modeled the flow and heat transfer characteristics of the system. However, in recent times many systems of interest have become small enough to be modeled discretely on an atomic scale. In these situations, a purely continuum description of fluid motion is obviously inappropriate. How a system is to be modeled usually begins by judging the length scale of the problem. Several important physical models with their corresponding length and time scales are shown below in Fig. 3.1.

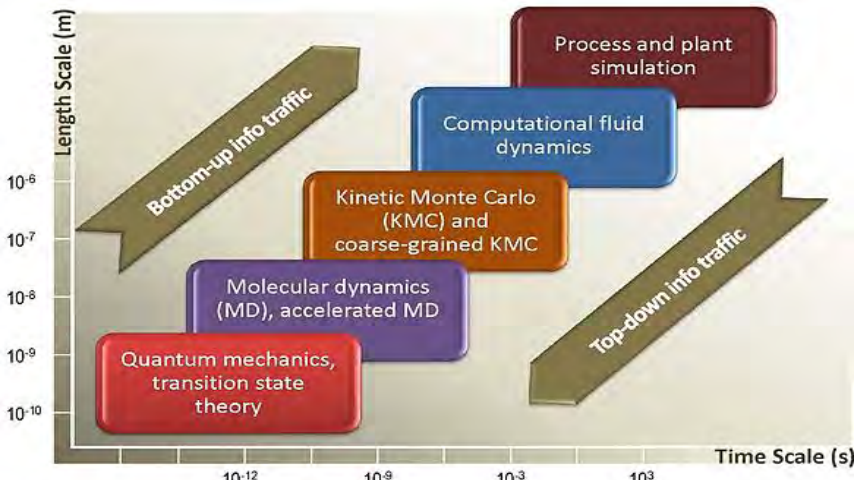

Fig. 3.1. Modeling methods in discrete and continuum regimes.

The computational fluid dynamics and heat transfer have been widely used to solve the continuum problems. The Monte Carlo (MC) method is mainly used for rare field gas dynamics. Molecular Dynamics (MD) is used for atomic modeling of a system where atoms are treated like hard balls, and their motions are described by Newton's laws and typically fall into nanometer length scale and nanosecond timescale. Quantum Modeling is done by solving the wave functions of the various subatomic particles and for describing the characteristics of an atomic system it would be more accurate but practically it is not used because of its tremendous computational cost especially when interphase phenomena are modeled. Therefore, for modeling the atomic behavior of interphase phenomena like evaporation or explosive boiling non equilibrium molecular dynamics simulation is becoming a very popular tool for the researchers. The MD simulation is now widely used for studying the nanoscale phase change phenomena as accurate experimentation in this very small length and time scale is very difficult. Furthermore, MD simulation is used to systemically investigate and proof or disproof any hypothesis for these systems.

In a molecular dynamics simulation, the system under study is modeled as an ensemble of interacting particles, including molecules, fractions of molecules, and atoms. The dynamics of the system is well approximated by the classical motion of the molecule's nuclei [51], which are considered as mass points and their motion is governed by the Newtonian Equations of motion. The mathematical formula of their interactions depends on the type of particles involved. In most cases it is a potential (or mathematically a functional) of all the nuclei's positions.

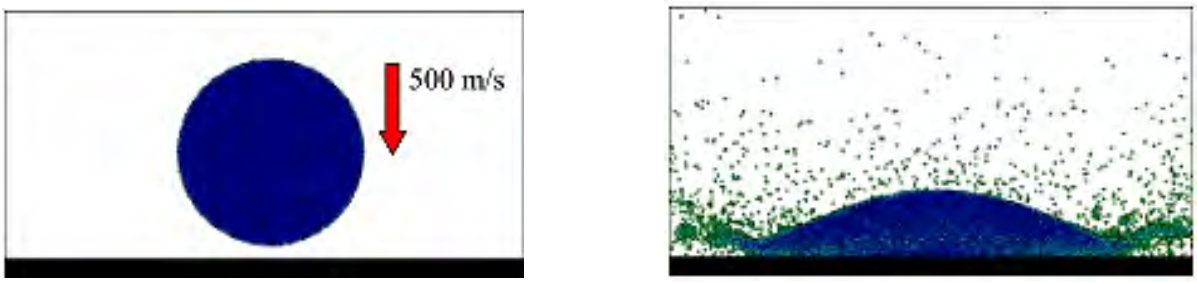

(a) (b)

Fig. 3.2. An example of MD simulation – collision of a droplet with a substrate, (a) Initial conditions are specified at $r_i(t_0)$ and $v_i(t_0)$, (b) Snapshot of domain at time t = 100 ps.

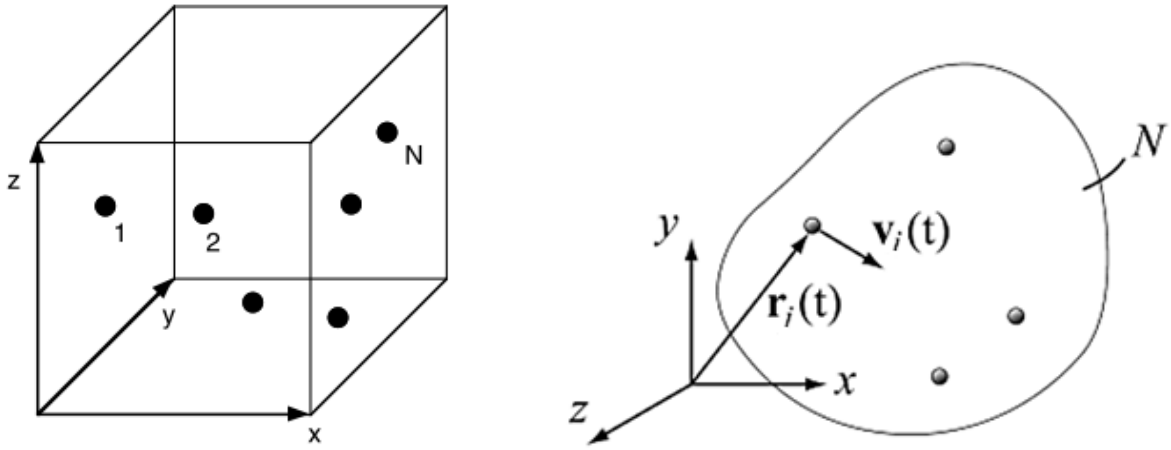

Fig. 3.3. MD simulation system as a collection of N particles contained in a volume

For a system composed of *N* particles (Figure-3.2), the equations of motion are,

$$m_i \dot{v}_i = -\frac{\partial \Phi}{\partial r_i}, \quad i = 1, 2, 3\ldots\ldots, N \tag{3.1}$$

$$\dot{r}_i = v_i, \quad i = 1, 2, 3\ldots\ldots, N \tag{3.2}$$

Where, m_i is the mass of the i-th particle, r_i is its position, v_i is the velocity, and Φ is the interaction potential of the entire system. Note that both r_i and v_i here are three-dimensional vectors. In this way, the dynamics of the system is depicted by the $6N$ first-order Newtonian ordinary differential equations. Various algorithms which can be used to solve the equation of motion is discussed in section 3.3. There are two key ingredients to conduct a successful molecular dynamics simulation for real materials: (1) robust and efficient numerical algorithms which solve the $6N$ Newtonian ordinary differential equations, and (2) sophisticated potentials which depict the interactions between particles accurately.

3.2 Potential Function

In order to simulate practical molecules, the determination of the suitable potential function is very important. In MD simulation Intermolecular interactions are modeled by a potential. The potential function $\Phi (r_1,r_2, ..., r_N)$ describes how the potential energy of a system of N atoms depends on the coordinates of the atoms, $r_1, r_2, ..., r_N$. Usually the potential function is obtained by following methods:

- Assuming a functional form for the potential function and then choose the parameters to reproduce a set of experimental data. These are known as empirical potential functions (e.g. Lennard-Jones [59], Morse [71], Born-Mayer, etc.).
- Calculating the electronic wave function for fixed atomic positions. This is difficult for a system of many atoms. Different approximations are used and analytic semi empirical potentials are derived from quantum-mechanical arguments (e.g. Embedded Atom Method (EAM) by Foiles, Baskes, and Daw [65-66], Glue Model by Ercolessi et al. [67], bond order potentials by Tersoff and Brenner [68-69], etc.).
- Performing direct electronic-structure (quantum-mechanics-based) calculations of forces during ab-initio MD simulation (e.g., Car-Parrinello method using plane wave pseudo potentials [70])

The true interatomic interactions are quantum mechanical in nature, and there is no known way in which the true interactions described by the Schrödinger equation or Dirac equation for all electrons and nuclei could be cast into an analytical functional form. Hence all analytical interatomic potentials are by necessity approximations.

When choosing potential function for a MD model following characteristics should be considered:

- **Accuracy** (reproduce properties of interest as closely as possible)
- **Transferability** (can be used to study a variety of properties for which it was not fit)
- **Computational speed** (calculations are fast with simple potentials)

The choice of the interatomic potential depends on the area of intended application. For example, high accuracy is typically required in computational Chemistry and computational speed is often critical in Materials Science (processes have a collective character and big

systems should be simulated for long times), therefore appropriate potentials are selected based on these criteria.

Practically all atomistic simulations are based on the Born-Oppenheimer adiabatic approximation which separates the electronic and nuclear motions. Since electrons move much more quickly because of their smaller mass, during their motion one can treat the nuclei as fixed in instantaneous positions, or equivalently the electron wave functions follow the nuclear motion adiabatically. As a result, the electrons are treated as always in their ground state as the nuclei move.

For the nuclear motions considered, an expansion of Φ in terms of one-body, two-body,....., N-body interactions:

$$\Phi(r^{3N}) = \sum_{j=1}^{N} \phi_1(r_j) + \sum_{i<j}^{N} \phi_2(r_i, r_j) + \sum_{i<j<k}^{N} \phi_3(r_i, r_j, r_k) \tag{3.3}$$

The first term, the sum of one-body interactions, is usually absent unless an external field is present to couple with each atom individually. The second sum is the contribution of pure two-body interactions (pairwise additive). For some problems only this term is sufficient to be an approximation to Φ. The third sum represents pure three-body interactions, and so on.

3.2.1 Pair Potentials

The potential functions representing the non-bonded energy are formulated as a sum over interactions between the particles of the system. The simplest choice, employed in many popular force field, is the "pair potential", in which the total potential energy can be calculated from the sum of energy contributions between pairs of atoms. The potential, Φ can often be reasonably obtained by summing up the effective pair potential, $\phi(r_{ij})$,

$$\Phi = \sum_i \sum_{i<j} \phi(r_{ij}) \tag{3.4}$$

Some common pair potential functions are discussed below:

- **Hard/soft spheres –** the simplest potential without any cohesive interaction. Useful in theoretical investigations of some idealized problems.

$$\phi(r_{ij}) = \begin{matrix} \infty, & for\ r_{ij} \le r_0 \\ 0, & for\ r_{ij} \ge r_0 \end{matrix} \text{, Hard spheres} \tag{3.5}$$

$$\phi(r_{ij}) = \left(\frac{r_{ij}}{r_0}\right)^{-n} \text{ , Soft spheres} \tag{3.6}$$

- **Ionic –** Coulomb interaction of charges, strong, long range repulsion or attraction. Is often added to other functional forms to account for charge-charge interaction or polarization.

$$\phi(r_{ij}) = \frac{q_i q_j}{r_{ij}} \tag{3.7}$$

- **Lennard-Jones potential** – The best known pairwise potential function is the Lennard-Jones (LJ) potential [59]. This function was originally proposed for liquid argon. For a pair of atoms *i* and *j* located at r_i and r_j, the distance between two atoms is r_{ij} and the potential energy as defined by the LJ potential is:

$$\phi(r_{ij}) = 4\varepsilon\left\{\left(\frac{\sigma}{r_{ij}}\right)^{12} - \left(\frac{\sigma}{r_{ij}}\right)^{6}\right\} \quad \text{for, } r_{ij} < r_{cut} \tag{3.8}$$

$$\phi(r_{ij}) = 0 \quad \text{for, } r_{ij} > r_{cut} \tag{3.9}$$

Where, the parameter ε governs the strength of the interaction, and σ defines a length scale. The interaction repels at close range, then attracts, and is eventually cut off at some separation r_{cut} (known as the cut-off radius) to reduce computational cost while serving as a reasonable approximation and still providing good accuracy to the simulations. The LJ potential is the most widely used potential for molecular simulations, and provides accurate representation for the properties of argon [52] and used for all the cases in this study.

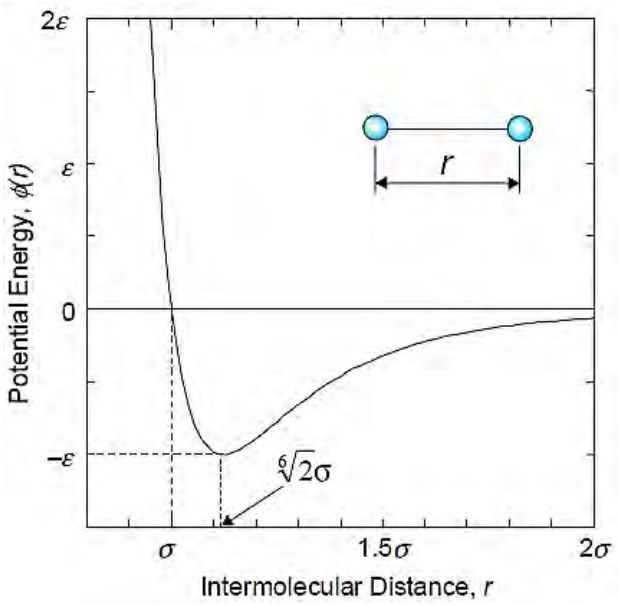

Fig. 3.4. Lennard-Jones (LJ) potential

- **Morse potential** – similar to Lennard-Jones but is a more "bonding-type" potential and is more suitable for cases when attractive interaction comes from the formation of a chemical bond [71]. It was a popular potential for simulation of metals that have face centered cubic (fcc) and hexagonal closed packed (hcp) structures.

$$\phi(r_{ij}) = \varepsilon\left[e^{-2\alpha(r_{ij}-r_0)} - 2e^{-\alpha(r_{ij}-r_0)}\right] \tag{3.10}$$

Here, r_{ij} is the distance between the atoms, r_0 is the equilibrium bond distance, and α controls the width of the potential.

- **6-exp (Buckingham) potential** – exponential term (Born-Mayer) provides a better description of strong repulsion due to the overlap of the closed shell electron clouds, which is important in simulation of bombardment by energetic atoms or ions, etc.

$$\phi(r_{ij}) = Ae^{-r_{ij}/R_{BM}} - \frac{B}{r_{ij}^6} \tag{3.11}$$

Here, A, B, and R_{BM} are constants. The two terms on the right-hand side constitute a repulsion and an attraction, because their first derivatives with respect to r are negative and positive, respectively. Buckingham proposed this as a simplification of the Lennard-Jones potential, in a theoretical study of the equation of state for gaseous helium, neon and argon [72].

3.2.2 Many Body Potentials

In many-body potentials, the potential energy includes the effects of three or more particles interacting with each other. In simulations with pairwise potentials, global interactions in the system also exist, but they occur only through pairwise terms. In many-body potentials, the potential energy cannot be found by a sum over pairs of atoms, as these interactions are calculated explicitly as a combination of higher-order terms.

Some many body potentials models are briefly discussed below:

- **The Stilinger-Weber potential** – is a potential [73] that has a two-body and three-body terms of the standard form,

$$V_{TOT} = \sum_{i,j}^{N} V_2(r_{ij}) + \sum_{i,j,k}^{N} V_3(r_{ij}, r_{ik}, \theta_{ijk}) \quad (3.12)$$

  Where, the three-body term describes how the potential energy changes with bond bending. It was originally developed for pure silicon, but has been extended to many other elements and compounds and also formed the basis for other silicon potentials.

- **Embedded Atom Model** – Metals are very commonly described with what can be called "EAM-like" potentials, i.e. potentials that share the same functional form as the embedded atom model [65-66]. In these potentials, the total potential energy is written as,

$$V_{TOT} = \sum_{i}^{N} F_i\left(\sum_j \rho(r_{ij})\right) + \frac{1}{2}\sum_{i,j}^{N} V_2(r_{ij}) \quad (3.13)$$

  Where, F_i is embedding function that is a function of the sum of the electron density $\rho(r_{ij})$. V_2 is a pair potential that usually is purely repulsive. In the original formulation the electron density function $\rho(r_{ij})$ was obtained from true atomic electron densities, and the embedding function was motivated from density-functional theory as the energy needed to 'embed' an atom into the electron density.

- **Bond order potentials** – Covalently bonded materials are often described by bond order potentials, sometimes also called Tersoff-like [68] or Brenner-like [69] potentials. These have a general form that resembles a pair potential:

$$V_{ij}(r_{ij}) = V_{repulsive}(r_{ij}) + b_{ijk} V_{attractive}(r_{ij}) \quad (3.14)$$

  Where, the repulsive and attractive part are simple exponential functions similar to those in the Morse potential. However, the strength is modified by the environment of

the atom *i* via the b_{ijk} term. If implemented without an explicit angular dependence, these potentials can be shown to be mathematically equivalent to some varieties of EAM-like potentials. The bond-order potential formalism has been implemented also for many metal-covalent mixed materials.

3.3 Time Integration Algorithm

The equation of motion needs to be integrated in order to obtain the positions and velocities of the atoms at every time step. In MD simulation unlike the simulation of fluid dynamics, simpler and straightforward integration scheme is usually preferred. A good integration algorithm should have the following characteristics,

- Small propagation error (allowing large time step)
- Small velocity propagation error
- Time reversibility
- Energy conservation

Some time integration algorithm schemes which are frequently used in MD simulation are discussed below:

3.3.1 Verlet Algorithm

In this simple integration scheme [74], position of atoms at $t + \Delta t$ is calculated based on the current positions, $r(t)$ and forces, $F(t)$ and the previous positions, $r\ (t - \Delta\ t\ )$. The Verlet algorithm for MD integration is a straightforward application of the two equations given below which are derived from Taylor's series expansion,

$$r(t + \Delta t) = 2r(t) - r(t - \Delta t) + a(t)(\Delta t)^2 \tag{3.15}$$

$$v(t) = \frac{r(t+\Delta t) - r(t-\Delta t)}{2\Delta t} \tag{3.16}$$

Where, acceleration $a(t) = F(t)/m$. The velocities are actually not needed to compute the trajectories, but they are useful for calculating observables like the kinetic energy etc.

Advantages:

1. Integration does not require the velocities, only position information is taken into account.

2. Only a single force evaluation per integration cycle. (Force evaluation is the most computationally expensive part in the simulation).

3. This formulation, which is based on forward and backward expansions, is naturally reversible in time (a property of the equation of motion).

Disadvantages:

1. The velocities, which are required for energy evaluation are calculated in an approximate manner only through the equation (3.15) (large errors).

2. Need to know $r(t+\Delta t)$ to calculate $v(t)$.

3.3.2 Leap-Frog Algorithm:

To obtain both the positions and velocities from readily available quantities, the leap- frog scheme can be applied. The updating equations are:

$$v\left(t+\frac{\Delta t}{2}\right) = v\left(t-\frac{\Delta t}{2}\right) + \mathrm{a(t)}\Delta t \tag{3.17}$$

$$r(t+\Delta t) = r(t) + v\left(t+\frac{\Delta t}{2}\right)\Delta t \tag{3.18}$$

The velocities are updated at half time steps and 'leap' ahead the positions. The current velocities can be obtained from,

$$v(t) = \frac{v\left(t+\frac{\Delta t}{2}\right)+v\left(t-\frac{\Delta t}{2}\right)}{2} \tag{3.19}$$

Advantages:

1. Improved evaluation of velocities.

2. Direct evaluation of velocities gives a useful handle for controlling the temperature in the simulation.

3. Reduces the numerical error problem of the Verlet algorithm.

Disadvantages:

1. The velocities at time *t* are still approximate.

2. Computationally a little more expensive than Verlet.

3.3.3 Velocity-Verlet Algorithm

An algorithm that yields the positions, velocities and forces at the same time is given by the Velocity-Verlet scheme [75]. After calculating the force acting on each atom *i* from the potential function, using the acceleration, the position and velocities are obtained via the integrator method for time $t + \Delta t$. The positions and velocities are updated according to,

$$r(t + \Delta t) = r(t) + v(t)\Delta t + \frac{1}{2}a(t)(\Delta t)^2 \tag{3.20}$$

$$v(t + \Delta t) = v(t) + a(t)\Delta t \tag{3.21}$$

Expressing the velocity at mid interval as $v(t + \frac{\Delta t}{2})$:

$$v\left(t + \frac{\Delta t}{2}\right) = v(t) + a(t)\frac{\Delta t}{2} \tag{3.22}$$

$$r(t + \Delta t) = r(t) + \ v\left(t + \frac{\Delta t}{2}\right)\Delta t \tag{3.23}$$

$$a(t + \Delta t) = F(r(t + \Delta t))/m \tag{3.24}$$

$$v(t + \Delta t) = \ v\left(t + \frac{\Delta t}{2}\right) + a(t + \Delta t)\frac{\Delta t}{2} \tag{3.25}$$

The advantage of this method is that the calculation of velocities is in phase with that of the positions. Also, this method calculates the velocities more accurately than the other common Verlet and leap-frog methods [52]. Thus, after the new positions and velocities are obtained at time $t + \Delta t$, the whole process is repeated again i.e. force computation from linked cell algorithm, using Newton's second law and then integrator method to advance the system in time. Flowchart of Fig. 3.5 shows the implementation of velocity-Verlet algorithm.

Advantages:

1. Improved evaluation of velocities.

2. Secure the energy conservation (kinetic energy portion), especially for canonical ensemble.

3. Higher stability than predictor-corrector methods

Disadvantages:

1. Computationally more expensive than leap-frog algorithm.

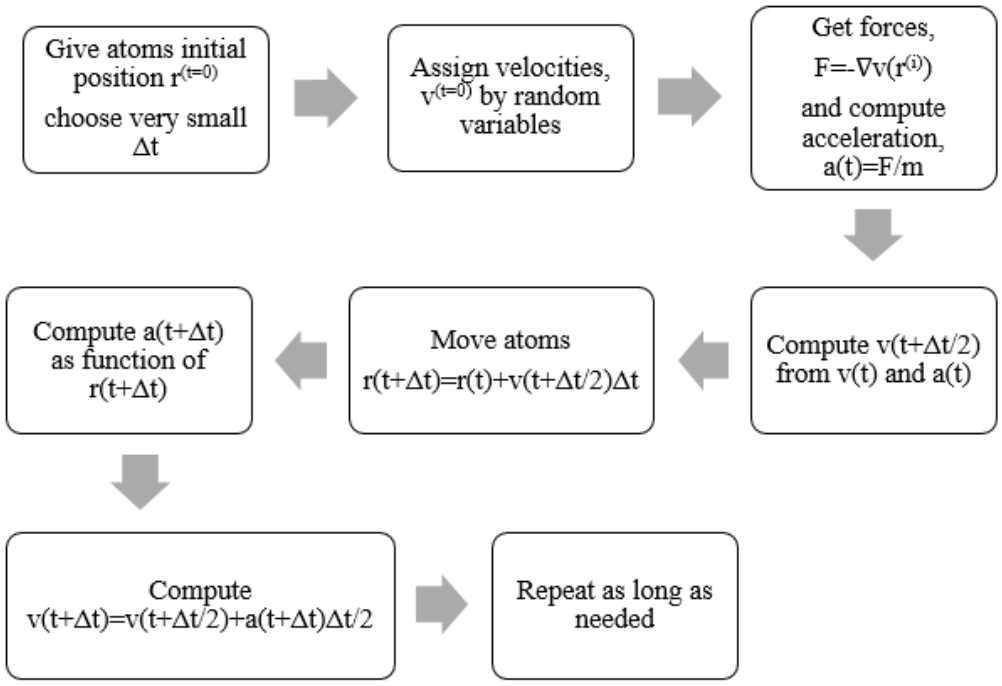

Fig. 3.5. Flowchart showing the implementation of velocity-Verlet method.

3.3.4 Predictor-Corrector Methods

These methods implies two steps to time integrate the equation of motion:

• A **predictor** step providing an initial approximation to the propagated solution

• A **corrector** step yielding a refined approximation.

Predictor-corrector methods provide higher accuracy than the Verlet method but require extra computations and memory. Therefore, they are sometimes employed depending on the

complexity of the potential function and the demand of the accuracy of motion in each time step.

3.4 Boundary Conditions

Since the spatial and temporal scale handled with the MD method is extremely small compared to the scale of macroscopic heat transfer phenomena, the most important point of the design of a MD simulation applied to the macroscopic problem is the boundary condition. In the present work, the computational domains are in the form of a cuboid. This imposes a total of six boundaries, two each in the x, y and z directions. Three boundary conditions are used in this work depending on the problem simulated.

3.4.1 Boundary Conditions for Atomic Motion

A. Periodic Boundary Condition

A system that is bounded but free of physical walls can be constructed by using this boundary condition. This is equivalent to considering an infinite, space-filling array of identical copies of the simulation region. An atom that leaves the simulation region through a particular boundary face immediately reenters the region through the opposite face. Also, atoms lying within the cutoff distance of a boundary interact with atoms near the opposite boundary. Thus, periodic boundaries have to be in multiples of two.

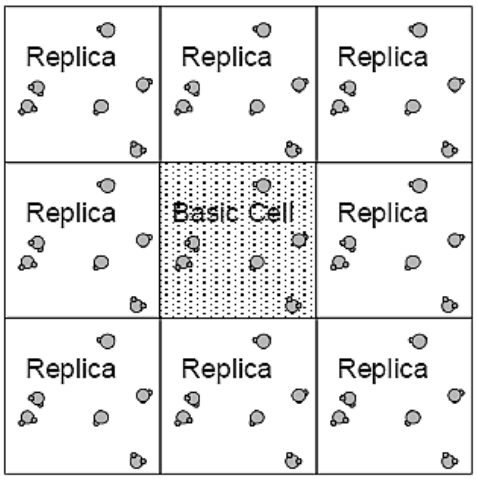

Fig. 3.6. Periodic boundary condition

B. Fixed Boundary Condition

In certain cases non-periodic or fixed boundary is used so that particles do not interact across the boundary and do not move from one side of the simulation box to the other. Fixed boundary condition should be used carefully because, if an atom moves outside the face it may be lost.

C. Mirror Boundary Condition

This boundary condition simulates an imaginary adiabatic wall. The collision of atom with this wall is perfectly elastic; momentum and energy are conserved. If an atom, which is close to the wall at time t, crosses this boundary at atom $t + \Delta t$, it will be placed inside the boundary as if it has been reflected by a mirror. The atom will be assigned the same position as it was at time t with the velocity directed away from the wall.

3.4.2 Thermostatting and Barostatting

Thermostatting means controlling the temperature of particles in a molecular dynamics simulation. Barostatting means controlling the pressure. Since the pressure includes a kinetic component due to particle velocities, both these operations require calculation of the temperature. Typically a target temperature (T) and/or pressure (P) is specified for a system, and the thermostat or barostat attempts to equilibrate the system to the requested T and/or P.

Temperature is computed as kinetic energy divided by some number of degrees of freedom and the Boltzmann constant. Since kinetic energy is a function of particle velocity, there is often a need to distinguish between a particle's advection velocity which results due to some aggregate motion of particles and its thermal velocity. The sum of the two is the particle's total velocity, but the latter is often what is wanted to compute a temperature.

In the present study, LAMMPS is used as the molecular dynamics simulator which is broadly discussed in sections 3.7-3.11. There are several methods for thermostatting the system are available in LAMMPS, which are Nose-Hoover (NVT), Berendsen, CSVR, Langevin, and direct rescaling. Langevin thermostat has been used in this study for all the cases for controlling the temperature of group of atoms. In addition, two barosttating methods are currently available in LAMMPS which are Nose-Hoover (NPT and NPH) and Berendsen methods.

3.5 Property Calculation from MD Simulation by Statistical Sampling

Statistical mechanics provides the link between thermodynamics and random atomic behavior. Molecular dynamics simulation is microscopic in nature, i.e., length and time scale are very small. The conversion of this microscopic information to macroscopic observables such as pressure, energy, heat capacities, etc., requires statistical mechanics.

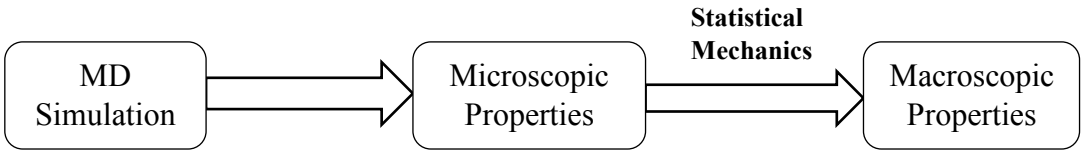

Fig. 3.7. Application of statistical mechanics in MD.

3.5.1 Statistical Ensembles

A key concept in statistical mechanics is the ensemble. An ensemble is a collection of microstates of system of molecules, all having one or more common extensive properties. Additionally, an ensemble defines a probability distribution accords a weight to each element (microstate) of the ensemble. A microstate of a system of molecules is a complete specification of all positions and momenta of all molecules (*i.e.*, all atoms in all molecules). This is to be distinguished from a thermodynamic state, which entails specification of very few features, *e.g.* just the temperature, density and total mass. Most frequently properties like the total energy, the total volume, and/or the total number of molecules (of one or more species, if a mixture) are encountered in a system as extensive properties. Thus an ensemble could be a collection of all the ways that a set of N molecules could be arranged (specifying the location and momentum of each) in a system of fixed volume.

If a particular extensive variable is not selected as one that all elements of the ensemble have in common, then all physically possible values of that variable are represented in the collection. The likelihood of observing a given element of an ensemble—its physical relevance—comes into play with the probability distribution that forms part of the definition of the ensemble. Any extensive property omitted from the specification of the ensemble is replaced by its conjugate intensive property. So, for example, if the energy is not specified to

be common to all ensemble elements, then there is a temperature variable associated with the ensemble. These intensive properties enter into the weighting distribution. It is common to refer to an ensemble by the set of independent variables that make up its definition. Thus the *NVT* ensemble collects all microstates of the same volume and molecular number, and has temperature as the third independent variable. The more important ensembles have specific names given to them. These are,

- Micro canonical ensemble (NVE)
- Canonical ensemble (NVT)
- Isothermal-isobaric ensemble (NPT)
- Grand-canonical ensemble (VTμ)

3.5.2 Ensemble Average

Ensemble (Thermodynamic) average is an average over all the points in the phase space at a single or definite time. For a given *N* and *V*, an element of an ensemble corresponds to a point in classical phase space, *Γ*. Phase space refers to the (highly dimensional) space of all positions and momenta of (all atoms of) all molecules:

$$\Gamma = (\mathbf{r}^N, \mathbf{p}^N) \tag{3.26}$$

Each molecule occupies a space of dimension *d*, meaning that each *r* and *p* is a *d*-dimensional vector, and *Γ* is then a 2*dN*-dimensional space (*e.g.*, for 100 atoms occupying a three-dimensional space, *Γ* form a 600-dimensional space). Consider an observable *A(Γ)* defined for each point in phase space, for example the total intermolecular energy. For a discrete set of microstates, the ensemble average of *A* is,

$$\langle A \rangle = \sum A_i \pi_i \tag{3.27}$$

Where, π is probability distribution for a certain statistical ensemble.

To calculate the thermodynamic or ensemble average we need to know the probability of finding the system at each point (state) in phase space. Ensemble (thermodynamic) average of observable $A(r^N,p^N)$:

$$\langle A\rangle_{ens} = \iint dp^N dr^N A(r^N p^N)\pi(r^N p^N) \tag{3.28}$$

3.5.3 Time or Dynamic Average

If the average of a quantity is taken at a single point of phase space over all times then it is known as the time or dynamic average. Let $<A>$ denote a time average over the trajectory generated by MD, where A is a dynamical variable, $A(t)$, then we can write,

$$\langle A\rangle_{time} = \lim_{\tau\to\infty} \frac{1}{\tau}\int_{t=0}^{\tau} A(r^N(t), p^N(t))dt \tag{3.29}$$

with t taken to be as long as possible. In terms of discrete time steps, Eq.(3.29) becomes,

$$\langle A\rangle_{time} = \frac{1}{M}\sum_{t=1}^{M} A(r^N, p^N) \tag{3.30}$$

Where, τ is the simulation time, M is the number of time steps in the simulation and $A(r^N,p^N)$is the instantaneous value of A.

3.5.4 Ergodic Hypothesis

According to Ergodic hypothesis, a large number of observations made on a single system at N arbitrary instants in time have the same statistical properties as observing N arbitrarily chosen systems at the same time. So, for infinitely long trajectory, thermodynamic or ensemble average can be considered equal to time or dynamic average,

$$\langle A\rangle_{time} = \langle A\rangle_{ens} \tag{3.31}$$

So, in molecular dynamics simulation, thermodynamic averages can be calculated via time averaging,

$$\langle A\rangle \approx \frac{1}{N}\sum_{i=1}^{N} A(t_i) \tag{3.32}$$

For example, the average potential and kinetic energy can be calculated by following equations,

Average potential energy,

$$\langle U \rangle \approx \frac{1}{N} \sum_{i=1}^{N} U(t_i) \tag{3.33}$$

Average kinetic energy,

$$\langle k \rangle \approx \frac{1}{N} \sum_{i=1}^{N} \sum_{j=1}^{M} \frac{m_j}{2} v_j(t_i) v_j(t_i) \tag{3.34}$$

3.6 Molecular Dynamics Simulation on Multiphase Heat Transfer Phenomena

Molecular level phenomena and their investigation are becoming very important in heat and mass transfer research because of its applicability in some new and forthcoming engineering applications in the areas of micro and nanotechnologies and also to understand the characteristics of certain fundamental phenomena.

More specifically, studies of basic mechanisms of heat transfer such as phase change phenomena demand the understanding of liquid-solid contact phenomena (such as wetting and nucleation) at the nanoscale level. Heat transfer in three-phase lines (evaporation or condensation of liquid on a solid surface, or solidification of a molten droplet on a surface) is a singular problem at the macroscopic level. The nucleation theory of a liquid droplet in vapor or of a vapor bubble in a liquid sometimes needs to take into account nuclei of the size of molecular clusters. The effect of the surfactant on the heat and mass transfer through liquid-vapor interface is also an example of the direct effect of molecular scale phenomena on the macroscopic problem. Even though much effort has been spent in extending macroscopic analyses to microscopic conditions in space (micrometer scale down to nanometer scale), time (microsecond, nanosecond and picosecond scales), and rate (extremely high heat fluxes of the order of Gigawatts), there is a clear limitation to these extrapolations. On the other hand, the development of the molecular dynamics (MD) computer simulation technique has demonstrated the possibility of tackling such phenomena from the opposite direction, by following a bottom up approach. The MD methods have long been used and are well developed as tools in statistical mechanics and chemistry [50, 55]. However, it is a new challenge to employ the method to the spatial and temporal scale of microscopic heat transfer phenomena and systems [56, 57]. At the same time, technologies such as, the thin film

manufacturing developed in the semiconductor industry, nanotube manufacturing and characterization, and the development of novel materials demand the prediction of heat transfer characteristics at the nanometer scale [58].

Two areas which are vital in many engineering applications where marked advances in molecular dynamics have already been made are phase change processes (vaporization/condensation and freezing/melting) and heat conduction (exemplified by the determination of thermo physical properties of thin films).

3.7 LAMMPS – Large Atomic Molecular Massively Parallel Simulator

LAMMPS is an open source, classical molecular dynamics code developed by Sandia National Laboratories, USA. It is a code that models an ensemble of particles in a liquid, solid, or gaseous state. It can model atomic, polymeric, biological, metallic, granular, and coarse-grained systems using a variety of force fields and boundary conditions. LAMMPS can model systems with only a few particles up to millions or billions. The current version of LAMMPS is written in C++.

Although LAMMPS runs efficiently on single processor workstations, it is designed for parallel applications. The maximum number of atoms that can be modeled in a simulation is dependent on computational power. In most atomic systems, the time required for computing scales linearly with the number of atoms in the system. The same linear scaling does not hold for the number of processors and limitations occur when any code runs in parallel on a multiprocessor machine. The overhead associated with communicating between processors becomes important and, given enough processors, will eventually dominate the computational time. A maximum of only four processors was used at any time in this work, meaning that most of the runtime is spent on molecular dynamics rather than processor communication.

In the most general sense, LAMMPS integrates Newton's equations of motion for collections of atoms, molecules, or macroscopic particles that interact via short- or long-range forces with a variety of initial and/or boundary conditions. For computational efficiency LAMMPS uses neighbor lists to keep track of nearby particles. The lists are optimized for systems with particles that are repulsive at short distances, so that the local density of particles never becomes too large. On parallel machines, LAMMPS uses spatial-decomposition techniques to partition the simulation domain into small 3d sub-domains, one of which is assigned to each

processor. Processors communicate and store "ghost" atom information for atoms that border their sub-domain. LAMMPS is most efficient (in a parallel sense) for systems whose particles fill a 3d rectangular box with roughly uniform density. Plimpton provides an explanation of the specific time integration method used by LAMMPS [53].

3.8 LAMMPS Operation

As an input, LAMMPS requires a list of initial atomic coordinates and molecular topology information such as mass and force field coefficients for each atom. This information can be either entered at the LAMMPS input script or generated by a custom code which is called when LAMMPS reads the input script. In either method, a simulation box is defined and filled with atoms whose positions and properties are determined by the user. Thermodynamic properties are controlled by defining an ensemble and/or holding some properties constant. Microscopic mechanical characteristics such as velocity and momentum can be explicitly assigned to individual or groups of atoms.

Since the number or position of atoms within the LAMMPS simulation box is not restricted in any way, an ensemble of atoms may be produced in any phase. Care must be taken to assure that the fluid's properties yield the desired location on the phase diagram.

Once the system constraints are set, LAMMPS updates the system by the time integration scheme over a predetermined number of timesteps. Integration is prematurely stopped if values stored in the program, such as a thermodynamic property, become unphysically large.

3.9 LAMMPS Pre- and Post-processing

Several features are available within LAMMPS that automatically generate lattices and simple geometric shapes. A built-in preprocessor can produce sets of atom coordinates that correspond to different three-dimensional shapes. The LAMMPS preprocessor takes user input for the specific shape and assigns the required atomic coordinates to a text file. More complex geometries can be created by bypassing the default preprocessor and inputting atomic coordinates via a text file. However, any geometric figure must always built from a collection of individual atoms which are positioned by the user.

The atoms must be positioned very carefully to create the desired simulation domain as any two atoms placed unnaturally close together can produce a near infinite repulsive force,

which leads to a large temperature on the following time step. The unexpectedly large force originates from the steep slope of the LJ potential near r = 0 and is completely avoidable by a proper choice of atomic spacing. Despite its simplicity, this is a common problem. Each atomic position is defined by an algorithm that writes Cartesian coordinates to a text file, thereby assuming atoms to exist only as points. The algorithm is chosen to space these points properly but exceptions can occur near boundaries of two geometric regions or on the border of the simulation box when periodic boundary conditions are applied. Most commonly, an atom located on one plane of the simulation box is accidentally imposed over another atom on the opposite side by periodic boundary conditions. The proximity of the two atoms produces a large temperature that crashes the program. Locating the offending atom(s) is not always trivial and the details of the input script can become important in resolving these conflicts.

No post-processing operations are available with LAMMPS. Post-processing duties are handled by a multi-functional code created by the author. This code allows the user to find the instantaneous properties like temperature, pressure, density etc. over a range of time steps. These quantities and related data are printed to a text file so that further analysis can be performed with a spreadsheet program.

3.10 Visual Molecular Dynamics

A visual output is vitally important in molecular dynamics. Although several good visualization codes exist, Visual Molecular Dynamics (VMD) is used throughout this work. VMD is specifically designed for visualizing biological and molecular systems and, like LAMMPS, it is adequately equipped to visualize the molecular systems. The Theoretical Biophysics Group at the University of Illinois at Champaign developed this open source code for public use [54].

VMD provides a way of animating the collection of data which LAMMPS provides as the coordinates for all the atoms of the simulation over a series of timesteps in the form of a properly-formatted text file. Because the atoms are represented by only a set of coordinates, a common approach to visualizing an atom is to assign a radius from the coordinate and fill the volume inside this radius with a solid color. VMD has a large variety of color schemes and visualization styles. The user may choose to work with the excellent VMD graphical interface or use the command prompt.

3.11 Application of LAMMPS in the Present Study: General Methodology

In the present study, the phase change phenomena of thin argon liquid film has been studied for different surface material, wettability and also by embedding nanostructures over the flat surface by MD simulation. The general methodology of simulating phase change phenomena by molecular dynamics has been established by closely reviewing the well-established literature and research works in this field. An overview of the methodology is presented in a flowchart as shown in figure 3.8.

At first a molecular system is set up by placing the sample atoms with desired lattice structure considering the phase and density of the material. For phase change phenomena, generally three phase system is defined which consists of solid atoms (generally a solid metal wall), liquid atoms adjacent to the solid wall and vapor atoms which reside just above the liquid atoms. Suitable potential function and boundary conditions for the system must be selected and also a time integration algorithm is used to advance the system with time.

After the initial stage of simulation, equilibrium molecular dynamics simulation is carried out to ensure that the whole system reaches to thermal equilibrium. At first the whole system is kept at a certain temperature (the equilibrium temperature, in case of this study it was 90 K) by thermostatting the solid, liquid and vapor atoms. In LAMMPS thermostatting can be done by a number of methods. In this study, the langevin thermostat is used for this purpose. The whole system is kept at this condition for a while and when the total energy of the system does not change anymore, the langevin thermostat applied to argon atoms (liquid and vapor) is removed. Then the system is allowed to reach at a desired equilibrium condition (temperature, pressure, energy, density). The thermal conductivity is also calculated during the equilibrium period.

At the final stage of simulation, non-equilibrium MD simulation is performed during which suddenly the temperature of the solid wall is increased by setting the langevin thermostat at a higher temperature. Non-equilibrium response of the liquid layer is analyzed in subsequent time steps. Both time averaged and spatial averaged data can be written in output files from which different properties of the system can be calculated and plotted. The state of the system can also be visualized by different software.

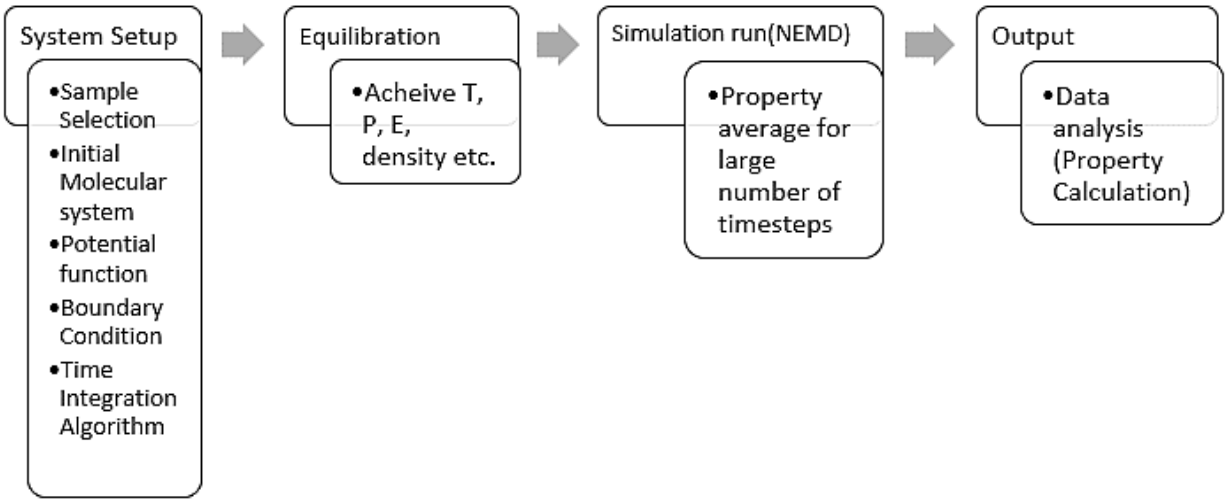

Fig. 3.8. A general description of MD simulation method applied to simulate phase change phenomena.

CHAPTER-4

RESULTS AND DISCUSSION

4.1. NEMD Simulation of Thin Film Liquid on Flat Surface

In the present study, two different cases have been considered based on the two different wall temperature (130 K and 250 K) to understand the evaporation (low temperature case) and explosive boiling (high temperature case) phenomena respectively. The wettability of surface was considered as hydrophilic when $\varepsilon_{liquid\text{-}solid} > \varepsilon_{liquid\text{-}liquid}$ and hydrophobic when $\varepsilon_{liquid\text{-}solid} < \varepsilon_{liquid\text{-}liquid}$. Three different materials namely platinum (Pt), silver (Ag) and aluminum (Al) were considered as the solid wall material.

4.1.1 Simulation Method and Validation of the Present Model

The simulation domain considered in this study contains liquid argon layers placed over a solid wall and argon vapor which resides over the liquid layers. As three different materials were considered, the solid wall contained platinum (Pt), silver (Ag) or aluminum (Al) atoms

for different cases. The initial configuration of the simulation domain is shown in Fig. 4.1, where the simulation cell is a cuboid having a dimension of 7.35 nm × 70.0 nm × 7.35 nm (x × y × z). At the bottom of the simulation box eight monolayers of solid (Pt or Ag or Al) atoms are placed which are arranged in a FCC (1 0 0) lattice. For all the cases, the solid wall has a total height of 1.505 nm. Different layers of the solid wall had different functions; the bottom layer of the wall was kept fixed to avoid any movement of sample; next two layers were set as the heat source and Langevin thermostat was applied to these two layers of the solid wall and the remaining five layers on top were considered as the solid wall through which heat is transferred to the adjacent liquid argon layers. The liquid argon layer has a total thickness of 3.01 nm and placed over the solid wall corresponding to its density of 1.367×10^3 kg/m^3 at 90 K having 3718 atoms. The rest of the space is filled with 475 argon vapor atoms corresponding to its vapor density of argon at 90 K. The total number of atoms in the system varied for different cases as each solid material has different density as tabulated in table-4.1.

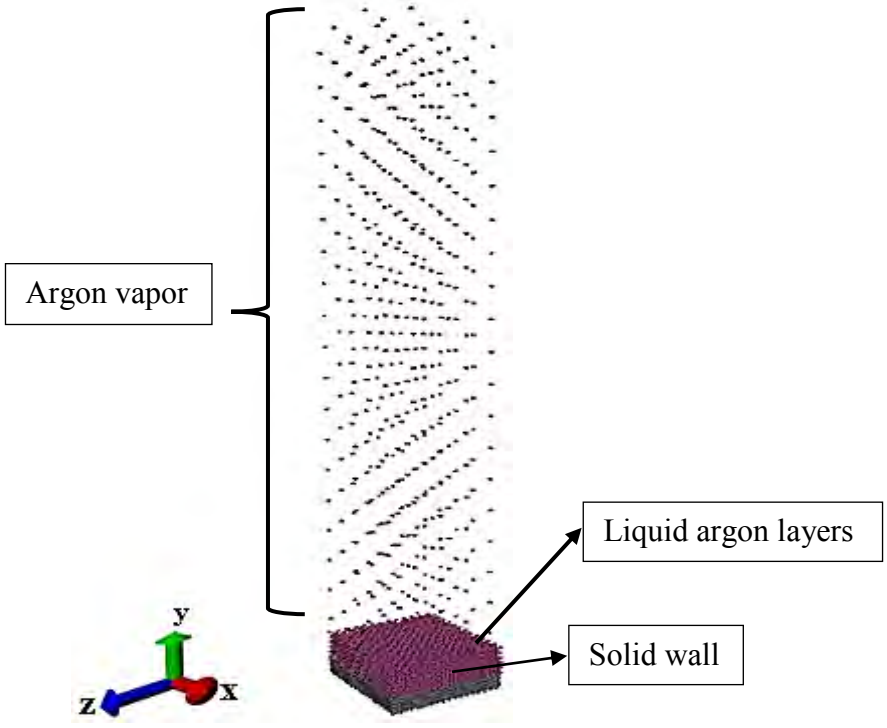

Fig. 4.1. Initial configuration of the simulation domain.

Table-4.1. Summary of molecular system

Materials	**Density kg/m^3**	**No. of Atoms**		
		Solid	**Argon**	**Total**

Pt	21450	5476	4193	9669
Ag	10500	5184	4193	9377
Al	2700	5004	4193	9197

The intermolecular forces for all atoms within the simulation domain was determined by the well-known Lennard-Jones (LJ) 12-6 potential [59]:

$$\phi(r_{ij}) = 4\varepsilon\left\{\left(\frac{\sigma}{r_{ij}}\right)^{12} - \left(\frac{\sigma}{r_{ij}}\right)^{6}\right\} \quad \text{for, } r_{ij} < r_{cut} \tag{4.1}$$

$$\phi(r_{ij}) = 0 \quad \text{for, } r_{ij} > r_{cut} \tag{4.2}$$

The values of energy parameter, ε and length parameter, σ for the liquid-liquid, solid-solid and liquid-solid interaction potentials are tabulated in tables 4.2 and 4.3. The energy parameter $\varepsilon_{liquid\text{-}solid}$ of solid-liquid interaction potential is varied to change the wettability of solid surface. As surface wettability is mostly defined by the contact angle, Hens et al. [46] showed in their study that when solid- liquid interaction potential is changed the contact angle of argon placed over flat solid platinum surface changes accordingly as shown in Fig. 4.2. The change of the contact angle suggested that when $\varepsilon_{liquid\text{-}liquid} < \varepsilon_{liquid\text{-}solid}$, the surface can be considered as hydrophilic and when $\varepsilon_{liquid\text{-}liquid} > \varepsilon_{liquid\text{-}solid}$, surface can be considered as hydrophobic. Based on their study [46] two different types of surfaces have been considered in the present study. When $\varepsilon_{liquid\text{-}liquid} / \varepsilon_{liquid\text{-}solid} = 0.5$, the surface is considered as hydrophilic, when $\varepsilon_{liquid\text{-}liquid} / \varepsilon_{liquid\text{-}solid} = 2$, surface is considered as hydrophobic.

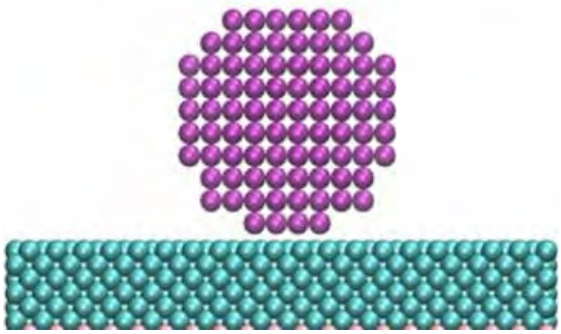

(a)

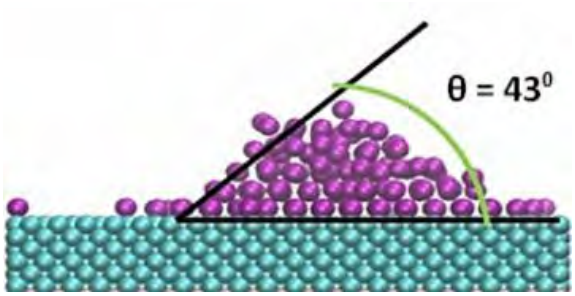

(b)

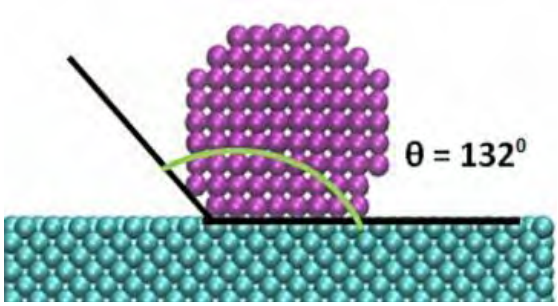

(c)

Fig. 4.2. Solid-liquid interfacial wettability and equilibrium contact angles (θ) of nanodroplet on solid surface(a) Initial state, (b) $\varepsilon_{liquid\text{-}liquid} < \varepsilon_{liquid\text{-}solid}$, θ =43° and hydrophilic, (c) $\varepsilon_{liquid\text{-}liquid} > \varepsilon_{liquid\text{-}solid}$, θ = 132° and hydrophobic (Adopted from Hens et al. [46]).

Table - 4.2. Liquid-liquid and solid-solid potential parameters for both hydrophilic and hydrophobic cases.

Interaction	***σ (nm)***	***ε (eV)***
Ar-Ar	0.3400	0.0104
Pt-Pt	0.2475	0.5200
Ag-Ag	0.2574	0.3510
Al-Al	0.2551	0.4080

Table - 4.3. LJ potential parameters for solid-liquid interface in different cases.

Interaction	***σ (nm)***	***ε (eV)***	
		hydrophilic	hydrophobic
Ar-Pt	0.2870	0.0208	0.005
Ar-Ag	0.2987	0.0208	0.005
Ar-Al	0.2975	0.0208	0.005

The equation of motion for each particle is integrated using velocity-Verlet algorithm with 5 femtosecond time step. Periodic boundary conditions were applied in the x and z directions, whereas a simple non periodic fixed boundary condition is assumed in the y-direction with adiabatic and elastic boundary at the top i.e. the argon atoms are reflected back to the simulation domain from the top boundary without any change of momentum and kinetic

energy. A cut off distance of $4\sigma_{Ar\text{-}Ar}$ is used for the potential functions to increase the computational efficiency.

The simulations of this study for all cases are carried out in three different stages. At the first stage, starting from the initial configuration of the simulation domain the entire system is set at a uniform temperature of 90 K by using Langevin thermostat. At this condition simulation was run for 1 ns.

Once the total energy and temperature in the simulation domain does not change anymore, the simulation enters to the second stage. The thermostat is removed for the fluid domain and the system was run for 1 ns. However, the temperatures of solid surface was still fixed at 90 K by the thermostat in this stage. Empirically, if the temperature and energy are stable during the subsequent timesteps at stage two, the system can be treated as in the thermal equilibration state. To check whether the system was in the equilibrium state or not, the thermodynamic states i.e. temperature, energy, pressure and density of argon atoms were closely monitored during this period. At the equilibrium period, the temperature of the argon and solid wall fluctuated around 90 K for all the cases.

The thermal conductivity, κ is a measure of the propensity of a material to transmit heat energy in a diffusive manner as given by Fourier's law,

$$J = -\kappa \nabla(T) \tag{4.3}$$

Where, J is the heat flux in units of energy per area per time and $\nabla(T)$ is the spatial gradient of temperature. Thermal conductivity of a material can be calculated by MD simulation in many ways. In this study, thermal conductivity is measured based on the Green-Kubo (GK) formula which relates the ensemble average of the auto-correlation of the heat flux to thermal conductivity, κ as given by the equation (4.4).

$$\kappa = \frac{V}{3k_B T^2} \int_0^\infty \langle J(0).J(t) \rangle \, dt \tag{4.4}$$

The heat flux vector, J can be calculated from the fluctuations of per-atom potential and kinetic energies and per-atom stress tensor in a steady-state equilibrated simulation.

$$J = \frac{1}{V} (\sum_i e_i v_i - \sum_i S_i v_i) \tag{4.5}$$

Where, e_i is the per-atom energy (potential and kinetic) and Si is the per-atom stress tensor.

Thermal conductivity of liquid argon was calculated during the equilibrium period which was compared with the thermal conductivity of argon at saturation temperature of 90 K as obtained by Younglove et al. [60] as listed in table-4.4.

Figures 4.3, 4.4 and 4.5 shows the number density profile of argon on hydrophilic platinum, silver and aluminum surface respectively during the equilibrium period. The number density profile is compared with the phase diagram of the Lenard Jones system [37, 61], and previously reported studies [40, 42] as shown in Fig. 4.6 and 4.7. From the comparison, it can be said that the system is indeed in thermal equilibrium. For hydrophobic case similar profiles are found.

Table - 4.4. Thermal conductivity of liquid argon

Temperature (K)	**Thermal Conductivity (W/mK)**		
	Present MD simulation	Younglove et al.[60]	Thermodynamic property Table (REFPROP)
90	0.1225	0.124	0.1245

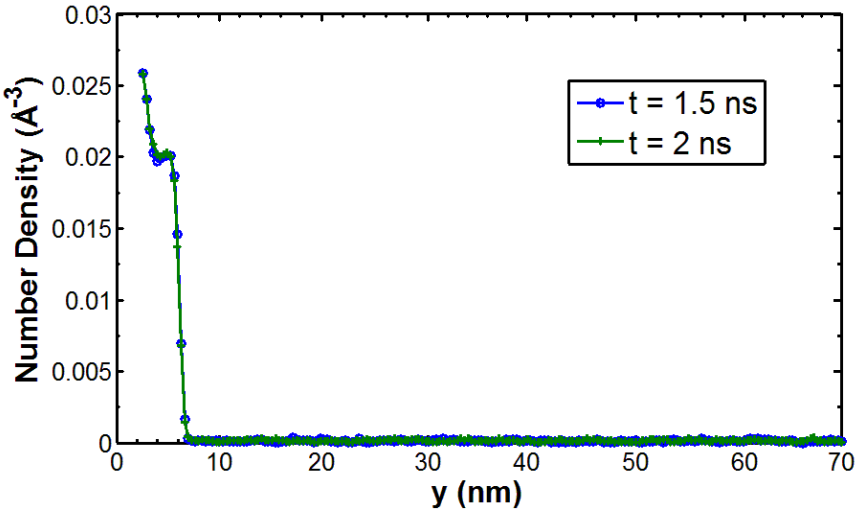

Fig. 4.3. Number density profile of argon on hydrophilic Pt-surface during equilibrium.

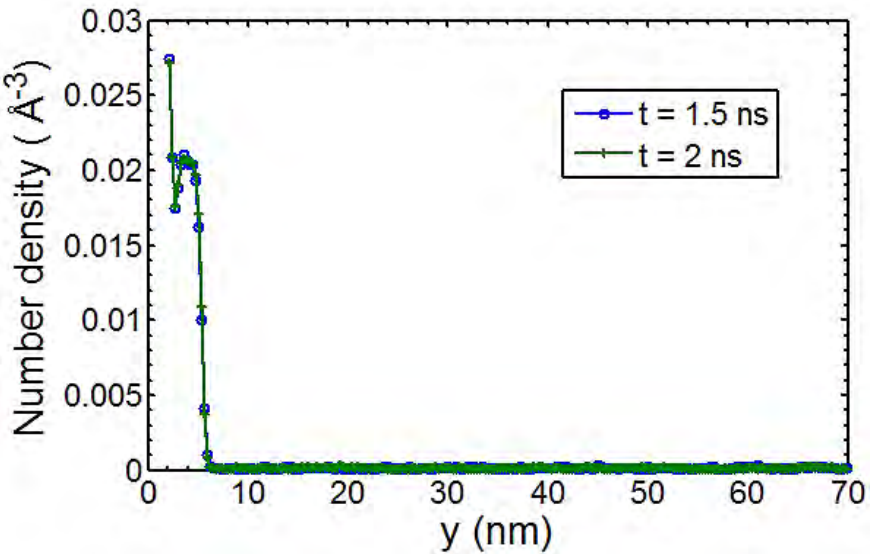

Fig. 4.4. Number density profile of argon on hydrophilic Ag-surface during equilibrium.

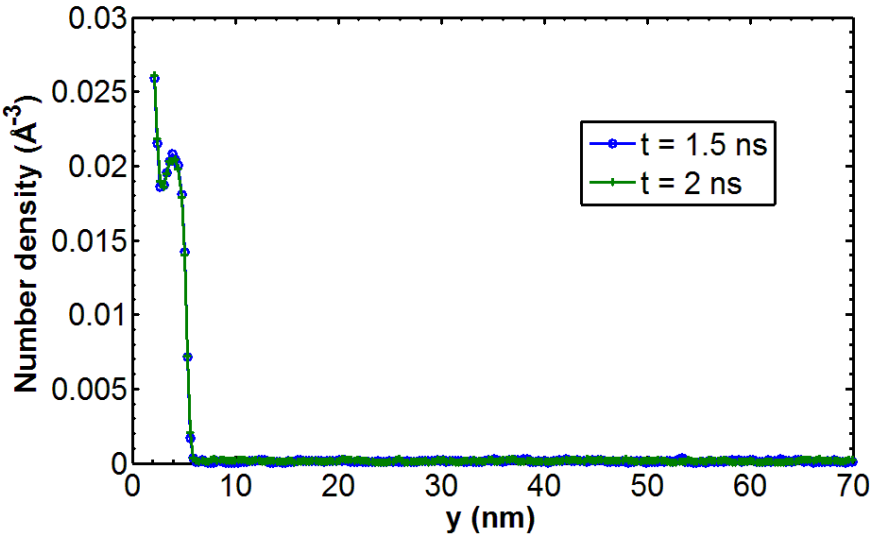

Fig. 4.5. Number density profile of argon on hydrophilic Al-surface during equilibrium.

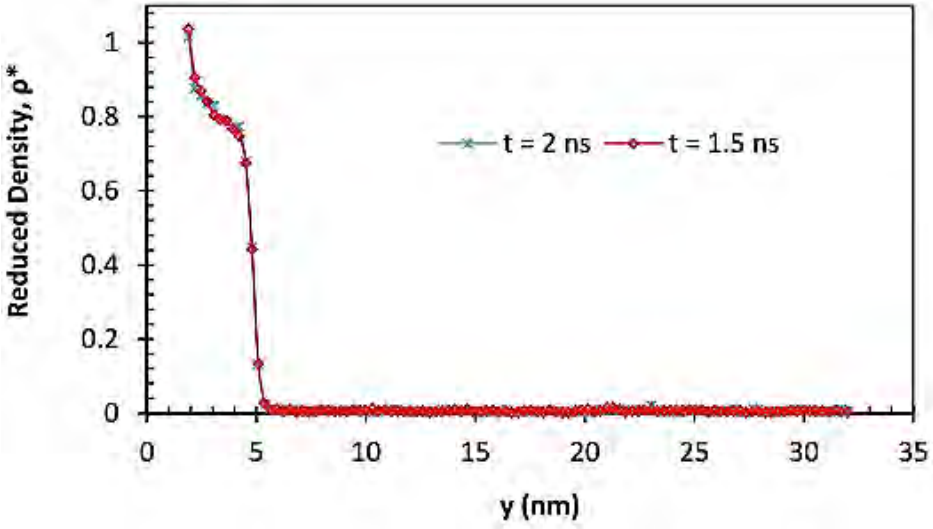

Fig. 4.6. Reduced density profile of argon on a flat surface during equilibrium as depicted in Morshed et al. [40].

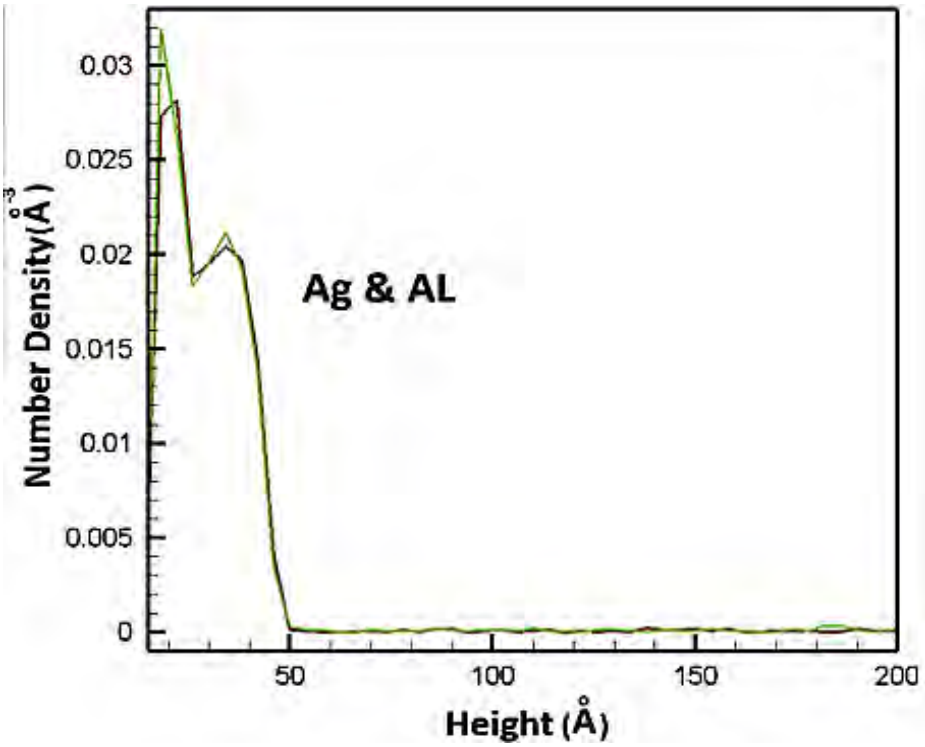

Fig. 4.7. Variation of density of argon with height of computational domain during equilibrium period as found by Seyf and Zhang [42].

After the attainment of the equilibrium, to initiate the boiling phenomena the Langevin thermostat of solid wall was set to rise to 130 K for the evaporation case and 250 K for the explosive boiling case. The upper three layers of the wall responded quickly and reached the target temperature within 50 ps. The simulation in this condition was run for 5 ns. Figure 4.8, 4.9 and 4.10 shows the temporal variation of total system energy per atom for both hydrophilic and hydrophobic cases with platinum, silver and aluminium surface respectively. The total energy E of the domain can be obtained by adding up the kinetic, E_{kin} and potential, E_{pot} energies. The kinetic energy can be computed from the individual momenta of the atoms, while the potential energy is the sum of interatomic interactions.

$$E_{kin} = \frac{1}{2}\sum_i^N mv_i^2 \tag{4.6}$$

$$E_{pot} = \sum_i \sum_{i<j} \phi(r_{ij}) \tag{4.7}$$

The system energy during equilibrium period for all the cases fluctuates around a mean value. The values of the system energy per atom during equilibrium period for a particular surface (hydrophilic or hydrophobic) are same which indicates that the simulation domain for different cases were equilibrated properly at 90 K. After the equilibration, the temperature of the solid wall was set to jump from 90 K to 130 K for evaporation case and 250 K for explosive boiling case. In the system energy profiles as shown in Figs. 4.8, 4.9 and 4.10, there is a steep rise of energy within a short time just after the solid wall temperature is increased from the equilibrium temperature. It should be noted that, the value of energy during equilibrium period is higher in case of hydrophobic surface and lower in case of hydrophilic surface, but increase of energy after the leap of the temperature is almost same. Figure 4.8, 4.9 and 4.10 confirm that rate of increase of energy is more rapid and much higher in case of explosive boiling than the evaporation.

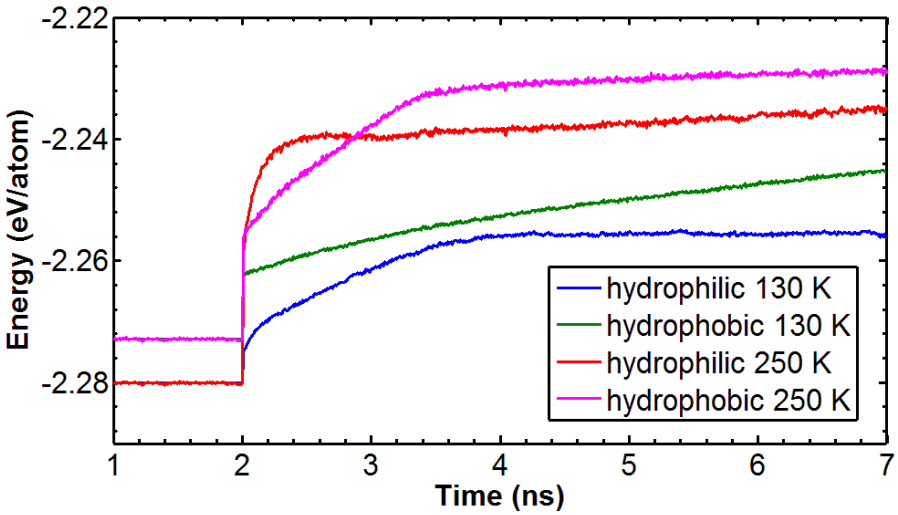

Fig. 4.8. System energy profile for evaporation and explosive boiling of argon over Pt-surface

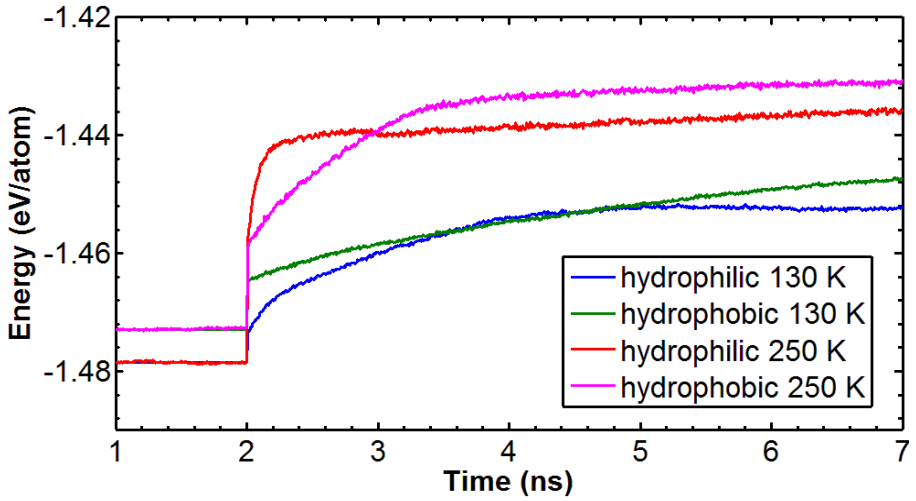

Fig. 4.9. System energy profile for evaporation and explosive boiling of argon over Ag-surface

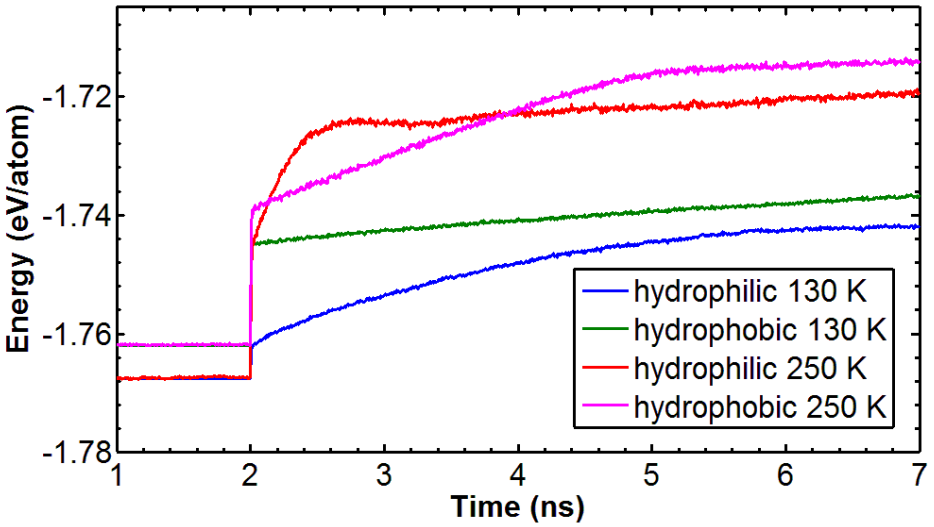

Fig. 4.10. System energy profile for evaporation and explosive boiling of argon over Al-surface

4.1.2 Low Temperature Case

In low temperature case, the temperature of solid wall is increased from 90 K to 130 K; snapshots of the simulation domain in this case for hydrophilic and hydrophobic Pt, Ag and Al-surface respectively are shown in Figs. 4.11 and 4.12. At initial stages there is no significant movement of argon atom from liquid to vapor region but as the time progresses liquid argon atoms gradually escapes from the top layer into the vapor region as individual atom or evaporation takes place. In case of hydrophilic surface this phenomena occurs rapidly than the hydrophobic surface. For hydrophobic surface the number of atoms that leave the liquid layer and enter the vapor region is quite few and from Figs. 4.11 and 4.12, it can be observed that, after 7 ns the thickness of argon atom layers adjacent to the hydrophobic solid

surface is much larger than the hydrophilic surface which clearly suggests that hydrophilic surface presented more favourable condition for evaporation. Figure 4.11 and 4.12 also suggests that the effect of surface material on evaporation is much less than the surface wettability. From these snapshots, the effect of change of solid surface material is not readily observable as it was in the case of change of wettability of surface.

The temperature history of the argon and solid wall during evaporation for all the cases is shown in Fig. 4.13 and 4.14 respectively. The temperature of the system is calculated from the kinetic energy of atoms. For N atoms, each with three degrees of freedom, the temperature of the domain is given by:

$$T = \frac{2E_{kin}}{3Nk_B} = \frac{1}{3Nk_B}\sum_i mv_i \tag{4.8}$$

Where, k_B is the Boltzmann constant. Temperature gradient along the height of the domain can be computed by dividing the height into equal slices, and computing the average temperature of each slice.

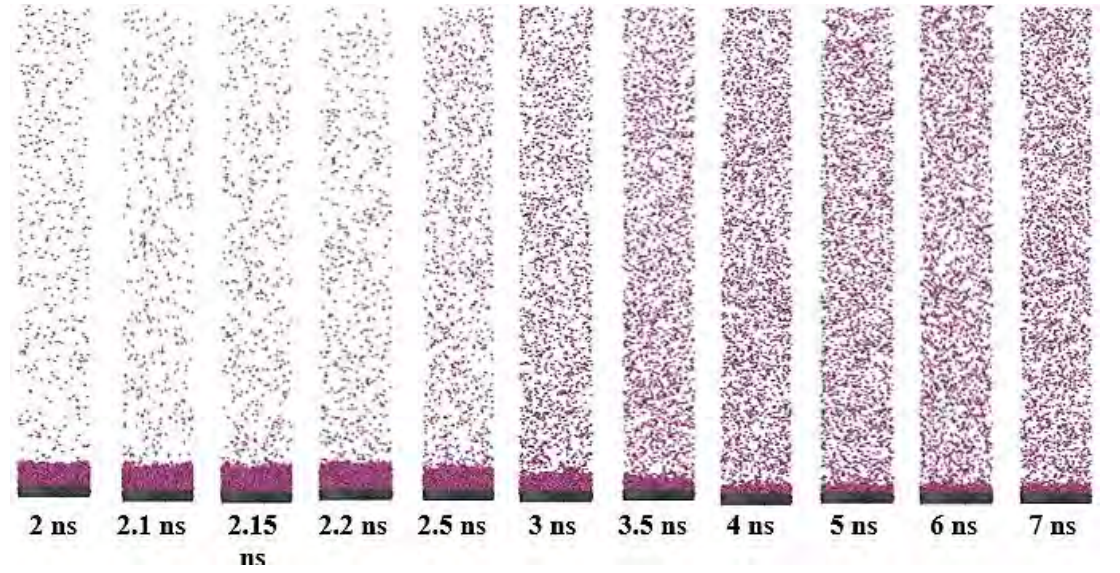

(a)

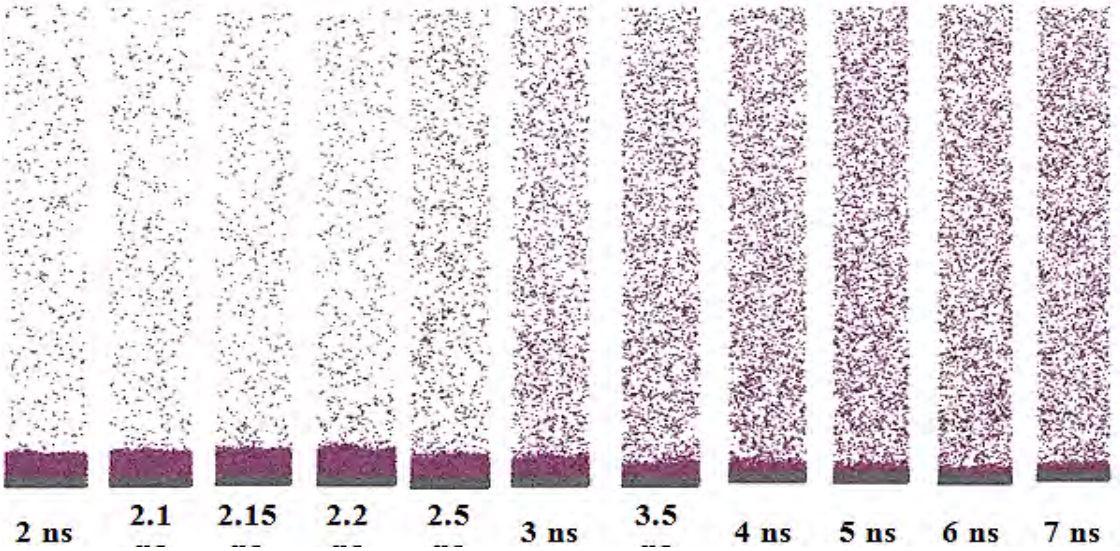

(b)

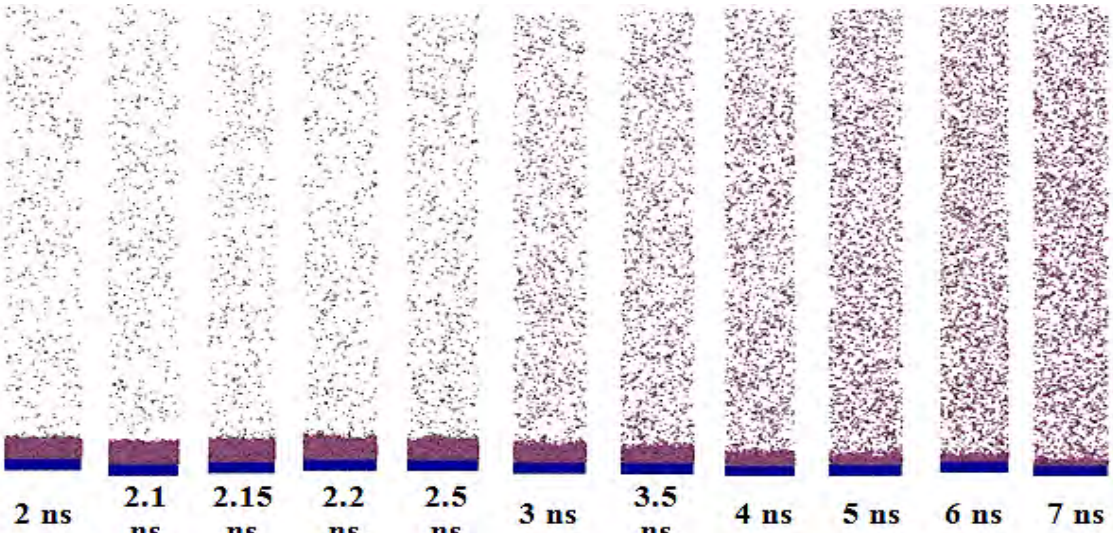

(c)

Fig. 4.11. Snapshots from the simulation domain for hydrophilic (a) Pt, (b) Ag, and (c) Al-surface for low temperature case.

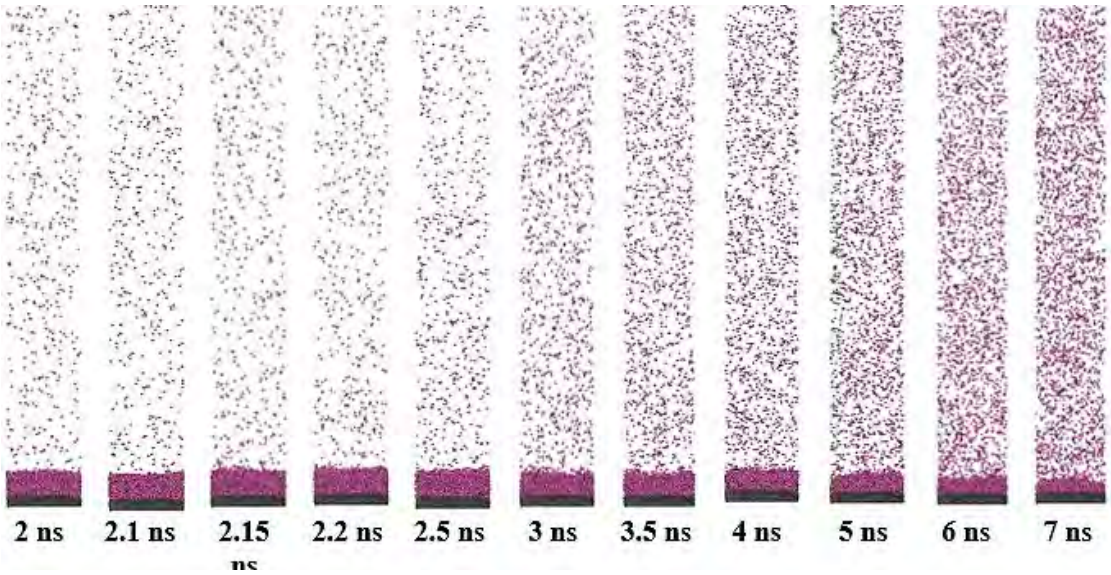

(a)

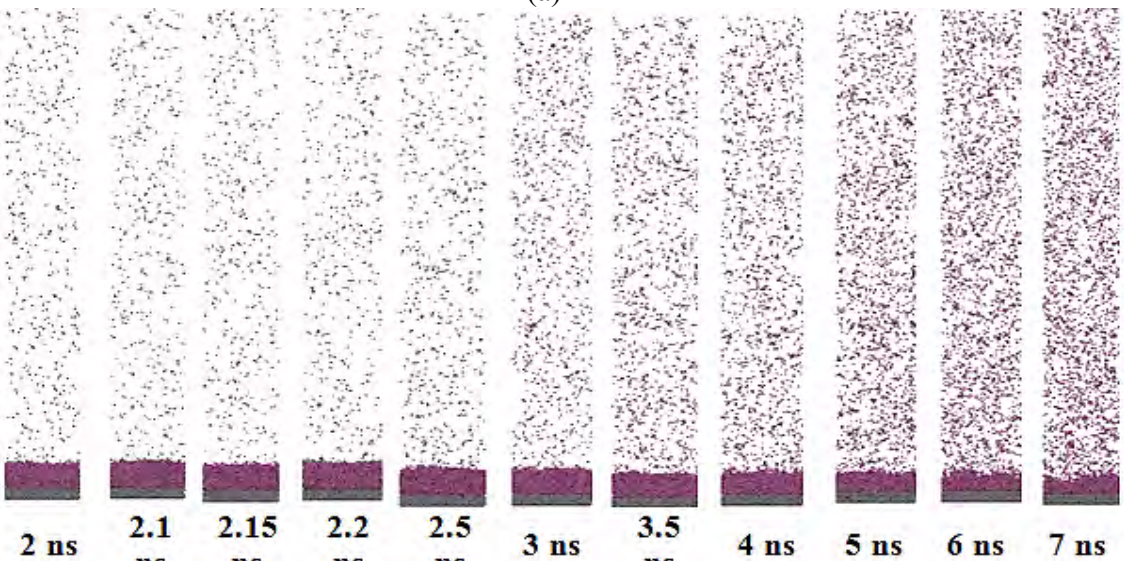

(b)

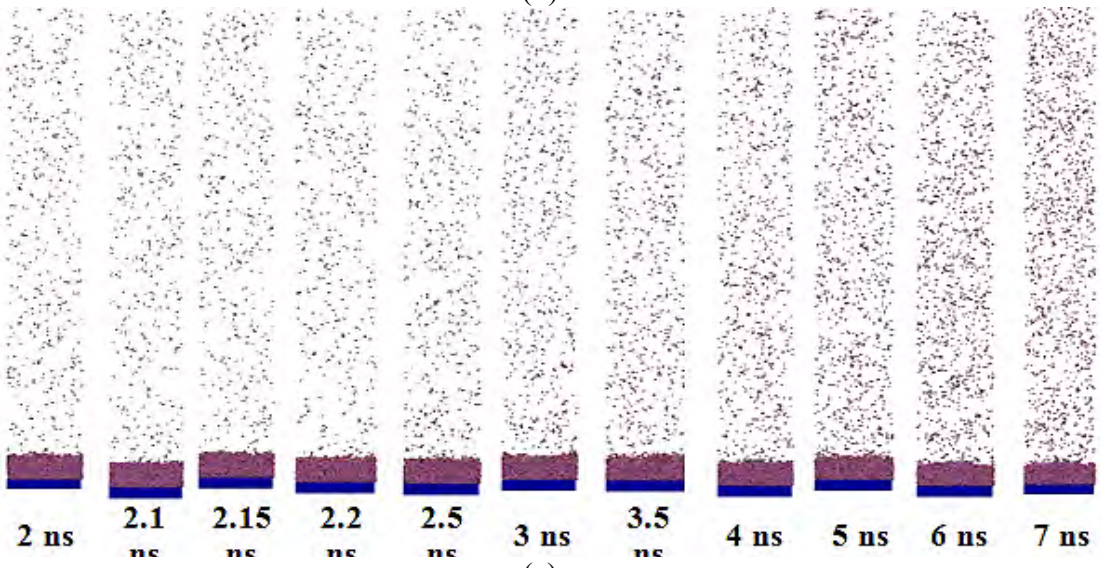

(c)

Fig. 4.12. Snapshots from the simulation domain for hydrophobic (a) Pt, (b) Ag, and (c) Al-surface for low temperature case.

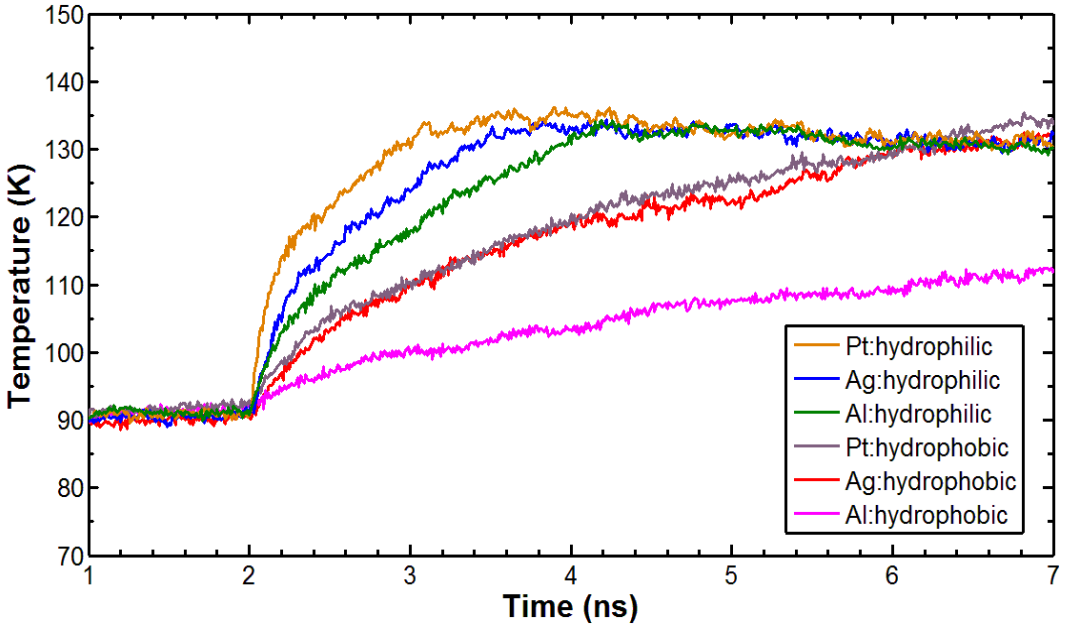

Fig. 4.13. Temperature history of argon for low temperature case.

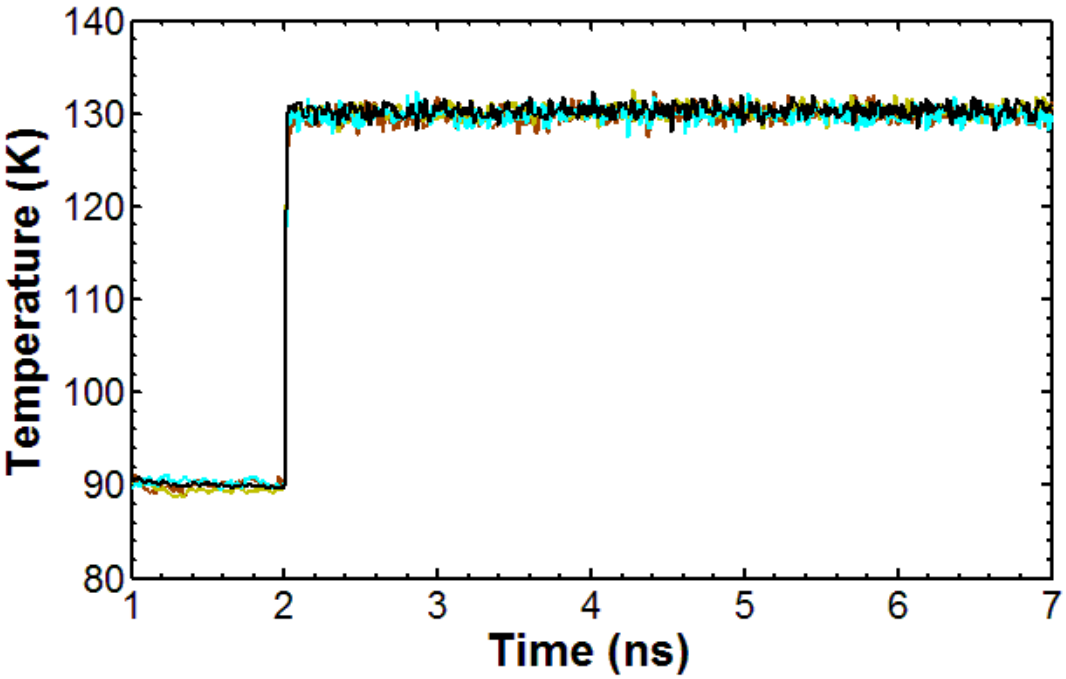

Fig. 4.14. Temperature history of solid wall for low temperature case.

It can be readily observed from Fig. 4.13 that the temperature of liquid argon reaches to equilibrium with the solid wall much quicker in case of hydrophilic surface than hydrophobic surface. The rapid increase of temperature in case of hydrophilic surface suggests that the energy is transferred from the solid surface to the liquid argon layer much quickly due to the higher solid-liquid interactions. Figure 4.13 suggests that, for both hydrophilic and

hydrophobic cases, the temperature of argon reaches to equilibrium with the solid surface first for Pt, then for Ag and last for Al-surface.

Figure 4.15 shows the pressure history of the system for all the cases in case of evaporation. The pressure is another useful property to monitor through a simulation. Its average value will provide information on the mechanical state of the system, i.e. if the system is compressed or expanded with respect to its equilibrium volume at the temperature of the simulation. The pressure of the system can be found by the virial formula:

$$P = \frac{N}{V} k_B T - \frac{1}{3V} \left(\sum_i \sum_{i<j} \frac{\partial \phi}{\partial r_{ij}} . r_{ij} \right) \tag{4.9}$$

Where, V is the volume of the system. As the volume of the system is constraint with the increase of the temperature pressure increases and follows similar trend of temperature as shown in Fig. 4.15 for all the cases.

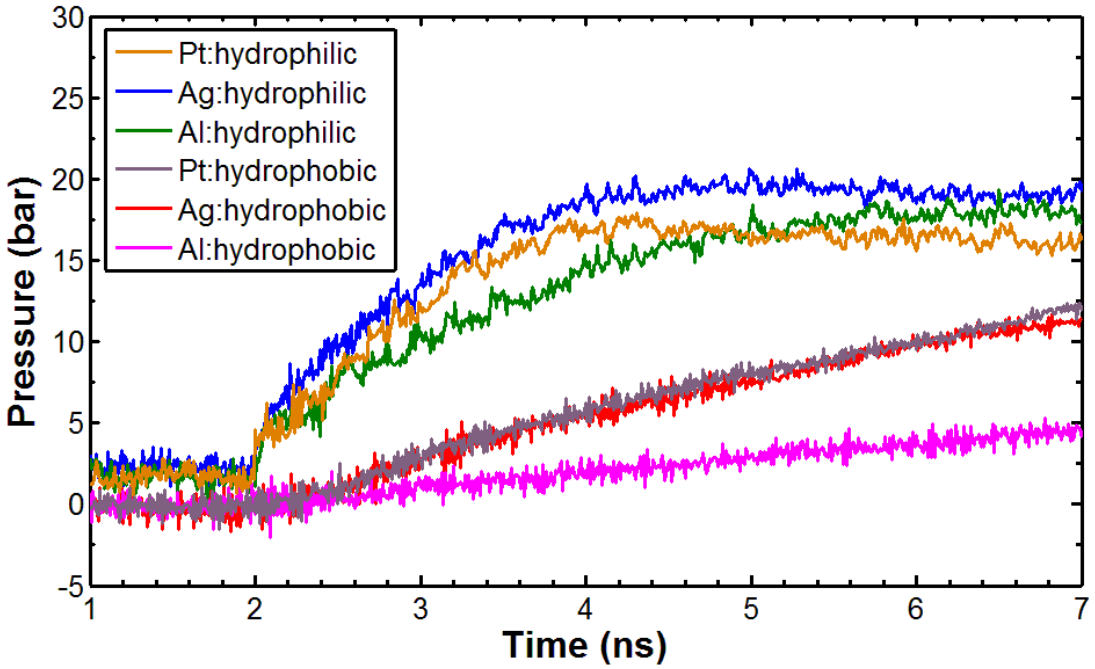

Fig. 4.15. Pressure history of the simulation domain for low temperature case.

With phase change being the main focus in this work, calculation of density becomes very important. The domain is divided into equal slices in y-direction and the number of atoms in each slice is counted to compute the density. Hence, if the slice thickness is Δy and N_i is the number of atoms in slice i, then the instantaneous density of that slice can be found out as:

$$\rho(y_i) = \frac{mN_i}{l_x l_z \Delta y} \tag{4.10}$$

Where, *lx* and *lz* are the *x* and *z* dimensions of the domain respectively, and *m* is the mass of the atom. The average density can be computed by time-averaging the instantaneous density. The average density can be plotted along the height (*y*-direction) of the domain to see the density gradient at different times. Number density calculates the average number of atoms in a slice, and can be found out using the same equation as above but without the term *m*.

Figure 4.16 and 4.17 show the number density profile of argon on Pt-surface for hydrophilic and hydrophobic case respectively. As expected, for both cases the argon atoms leaving the liquid layer to the vapor region with time and number density of argon atoms adjacent to solid wall (liquid layers) gradually decreases. By observing the snapshots of the simulation domain for Pt-surface as shown in Fig. 4.11, it was mentioned that, for hydrophilic the number of argon atoms leaving the liquid layers is much greater than the hydrophobic surface or evaporation takes place more rigorously in case of hydrophilic surface. This fact is confirmed by the number density profile of argon as shown in Figs. 4.16 and 4.17. From these figures, it can be readily observed that, as time progresses, the number density of argon atoms in liquid layers or adjacent to the solid wall is smaller in case of hydrophilic surface than the hydrophobic surface. Snapshots of Fig. 4.11 and number density profiles of Fig. 4.16 reveals the fact that, for hydrophilic surface after 5 ns, the number of atoms leaving liquid argon layers are very few or evaporation reaches to somewhat stagnant condition and the rest of the argon atoms in liquid layers remains adjacent to the solid Pt-surface as 'non-evaporating layers'. It is noteworthy to mention that Yu and Wang [32] and many other researchers [40-42] in their study found the existence of non-evaporating layer adjacent to the solid surface like the present study which is characterized by the crystal-like layer that has denser atoms than the liquid layer. For Ag and Al-surface similar characteristics of number density profile are observed.

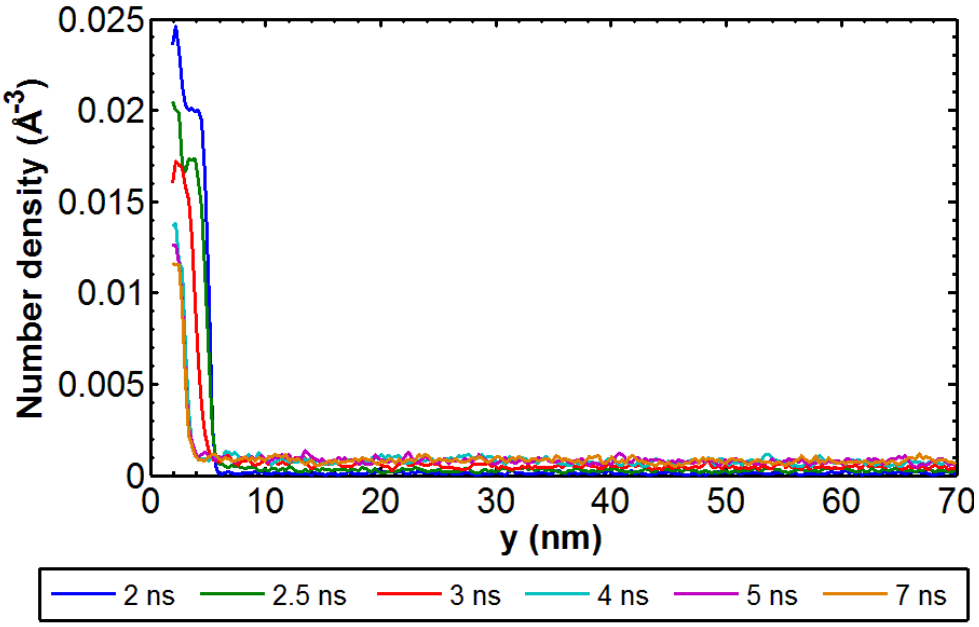

Fig. 4.16. Number density profile of argon on hydrophilic Pt-surface for low temperature case.

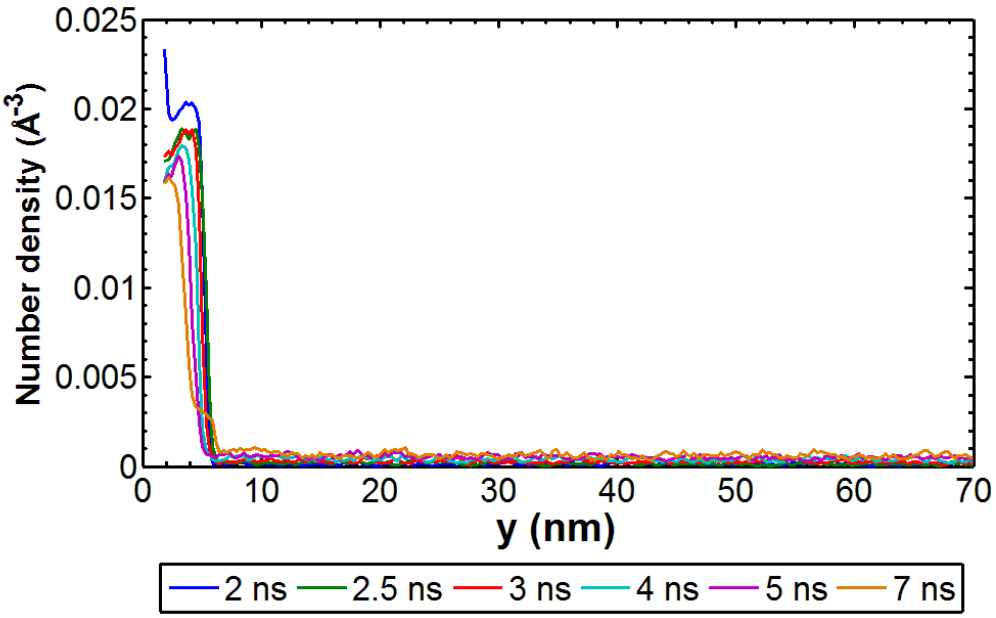

Fig. 4.17. Number density profile of argon on hydrophobic Pt-surface for low temperature case.

To investigate the effect of surface material more closely, the spatial temperature and number density profiles at a particular time, 3 ns for hydrophilic and hydrophobic condition of Pt, Ag and Al-surface has been plotted in Fig. 4.18 and 4.19 respectively. From these figures, it is evident that surface material has small effect on the evaporation phenomena compared to the wettability of surface. After closely examining the Fig. 4.18 and 4.19, it can be observed that, for both the cases Al-surface has the highest number density of argon atoms adjacent to solid wall, so among the three materials Al-surface provides least favorable condition for

evaporation. Number density profiles of argon in case of Pt and Ag-surface are very close to each other for both cases. The spatial temperature profiles of argon at 3 ns as shown in Fig. 4.18 and 4.19 show that in both cases, Pt-surface provides higher average temperature among the three materials while in case of Al-surface , the average temperature of argon is lowest among these three. From temporal variation of temperature of argon as shown in Fig. 4.13, at 3 ns for hydrophilic surface the average temperature of argon is around 130 K for Pt-surface, 125 K for Ag-surface and 120 K for Al-surface respectively.

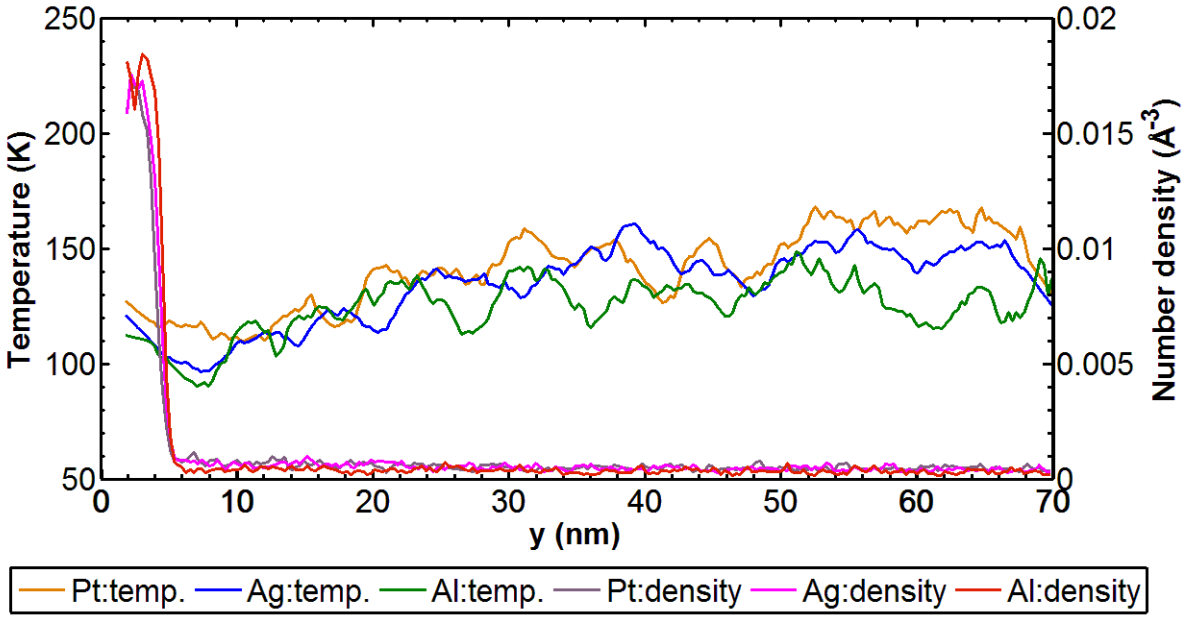

Fig. 4.18. Spatial distribution of temperature and number density of argon on Pt, Ag and Al-surface respectively for hydrophilic case at 3 ns for low temperature case.

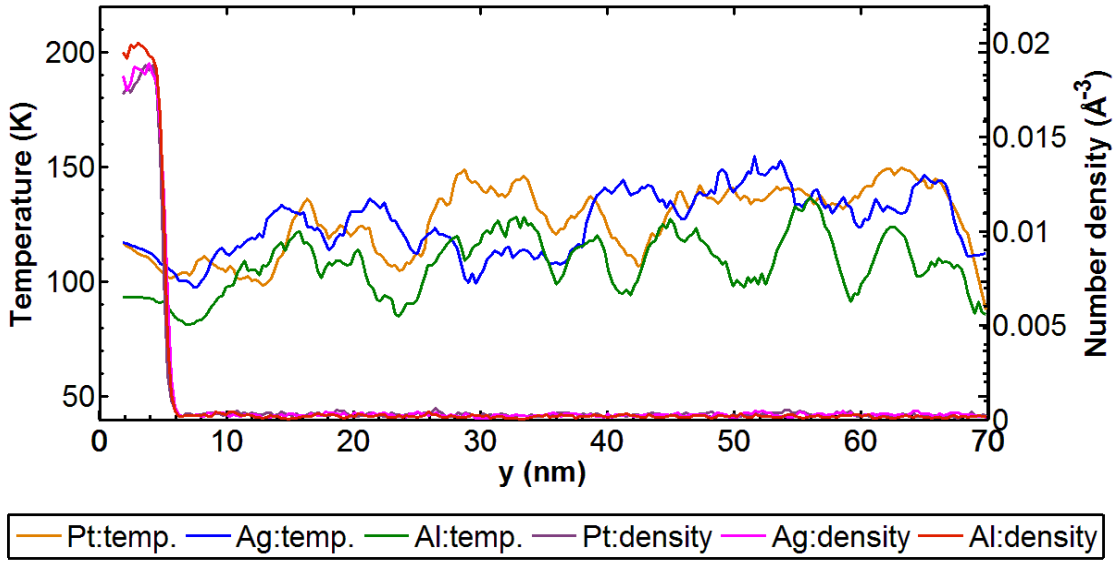

Fig. 4.19. Spatial distribution of temperature and number density of argon on Pt, Ag and Al-surface respectively for hydrophobic case at 3 ns for low temperature case.

For hydrophobic surface, the average temperature of argon was around 110 K for both Pt and Ag-surface, and 100 K for Al-surface. The spatial temperature profiles of Figs. 4.18 and 4.19 are in good agreement with these values. For hydrophilic case, as shown in Fig. 4.18, the average temperature of argon increases with the height of the simulation domain. Near the liquid layers which reside adjacent to the solid wall, temperature of argon atoms is low as their movements is less, which results low kinetic energy and temperature. If we move upwards, at the liquid- vapor interface, there are more movements of argon atoms which results higher temperature. At the vapor region or in the upper portion of simulation domain only argon vapor atoms exists, and their rapid movement from liquid layers towards the upper wall results high kinetic energy and temperature. In case of hydrophobic surface, as shown in Fig. 4.19, the gradient of temperature of argon along the height of the simulation domain is much less which suggests the movement of argon atoms in this case is much slower than the hydrophilic case.

For heat transfer phenomena, heat flux is an important tool for quantifying the effectiveness of heat transfer. In this study heat flux is calculated by two methods. In the first method, heat flux vector, J along the normal direction to the solid surface through the liquid film is calculated using Eq. (4.11) after estimating the per atom kinetic energy, per atom potential energy and per atom stress tensor.

$$J = \frac{1}{V}(\sum_i e_i v_i - \sum_i S_i v_i) \tag{4.11}$$

Where, e_i in the first term of the equation for J is the per-atom energy (potential and kinetic) and Si in the second term of the equation for J is the per-atom stress tensor. In this study, heat flux normal to the solid wall is calculated from the per atom potential energy, the per atom kinetic energy and per atom stress tensor as mentioned above. Figure 4.20 depicts the heat flux normal to the solid wall (xz plane) for all the cases during evaporation. For all the cases the trend of the profiles are same. Just after the jump of temperature of Langevin thermostat from 90K to 130K, a high heat flux is added within a short time. After this stage the heat flux decreases and oscillates about a mean value. The profiles of the heat flux are in good agreement with a previous study conducted by Yamamoto and Matsumoto [38]. For both hydrophilic and hydrophobic cases, Al-surface provides least amount of heat flux. The values of heat flux for Pt and Ag-surface are quite similar for both the cases. As expected the

hydrophilic case has the larger values of heat flux which are close to 3.3×10^{-5} eV/A^{2}ps or 560 MW/m^2 for Pt-surface,

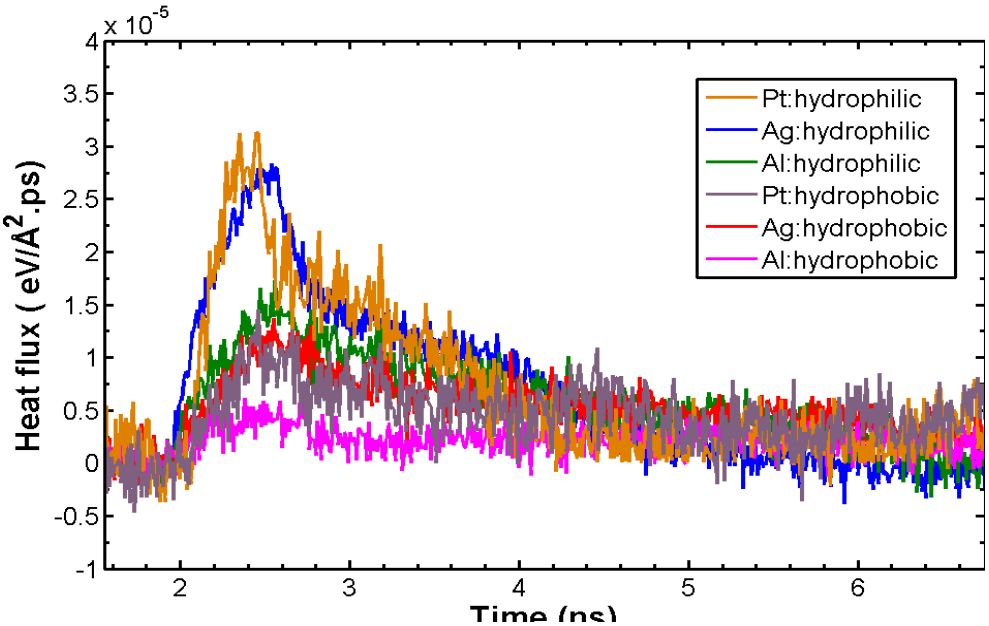

Fig. 4.20. Heat flux normal to solid wall for low temperature case.

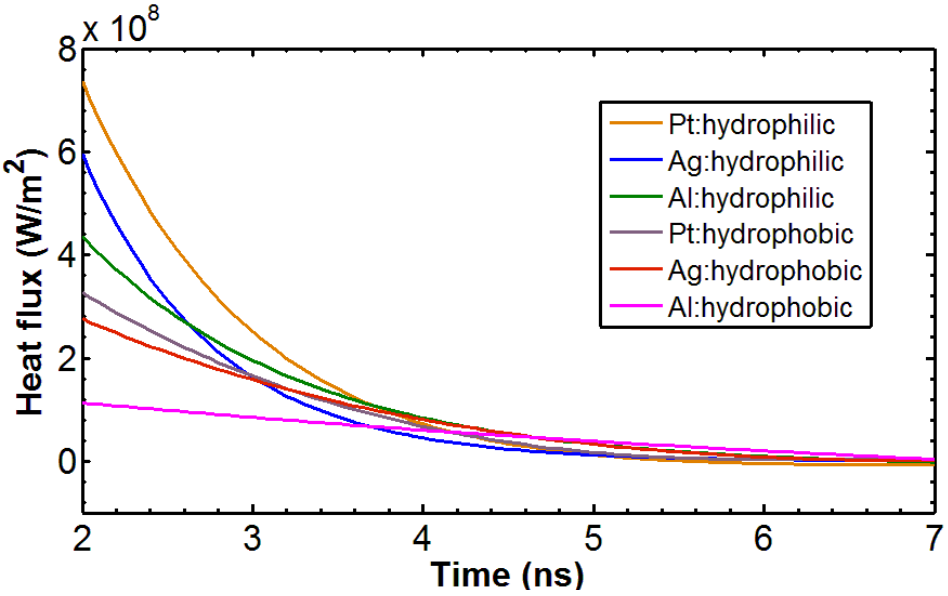

Fig. 4.21. Heat flux calculated from energy of the liquid for low temperature case.

2.8×10^{-5} eV/A^{2}ps or 460 MW/m^2 for Ag-surface and 1.8×10^{-5} eV/A^{2}ps or 288 MW/m^2 for Al- surface. For hydrophobic case, the magnitudes of the heat flux are much less 1.3×10^{-5} eV/A^{2}ps or 210 MW/m^2 for Pt-surface, 1.5×10^{-5} eV/A^{2}ps or 240 MW/m^2 for Ag-surface and 0.5×10^{-5} eV/A^{2}ps or 80 MW/m^2 for Al-surface. The magnitudes of heat flux in both hydrophilic and hydrophobic condition are in the order of theoretical maximum value of heat flux as defined by Gambill and Lienhard [47].

In the second method heat flux is calculated from slope of the total energy profile added of argon atoms [39]. The shape of the energy profile is similar to the system energy profiles as

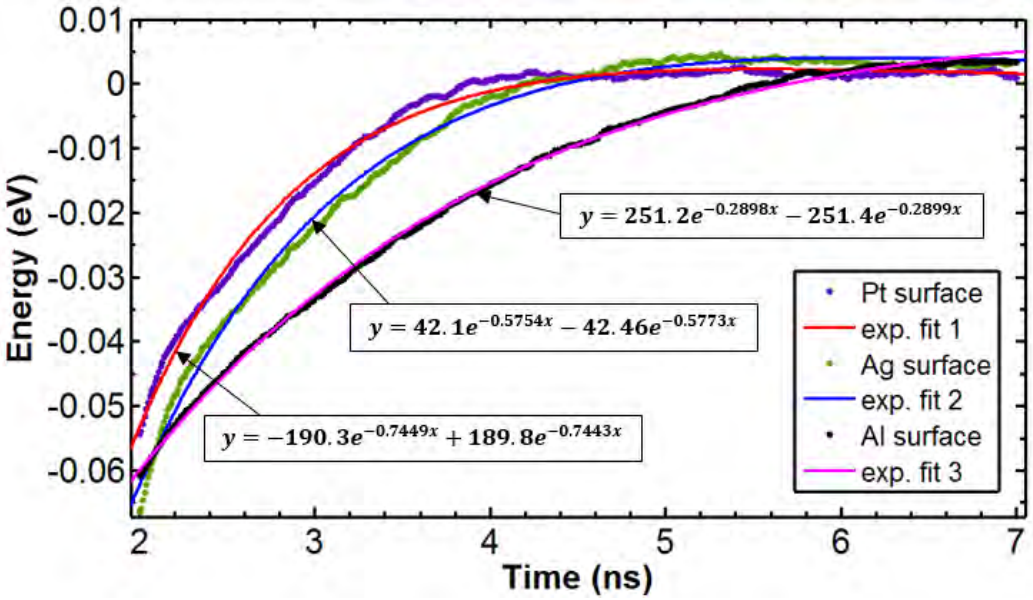

Fig. 4.22. Total energy of argon for hydrophilic Pt, Ag and Al-surface for low temperature case

shown in Figs. 4.8, 4.9 and 4.10. Figure 4.22 shows the total energy profiles of liquid argon for hydrophilic Pt, Ag, and Al surface for low temperature case. To find out heat flux, at first the best fit curves of the energy profiles have been drawn as shown in Fig. 4.22. Then the rate of change of energy is calculated by differentiating the equations of the best fit curves. Finally the rate of change of energy is divided by the cross-sectional area of the simulation domain (x-z plane) to find out the values of heat flux. The heat flux calculated from the energy of the liquid for low temperature case is shown in Fig. 4.21. The energy level of liquid suddenly jumps when the Langevin thermostat is switched to 130K from 90K, therefore, maximum heat flux occurs just at that time (at 2 ns). Heat flux then decreases with time very sharply. The value of the heat flux is larger for hydrophilic case. Comparing Fig. 4.21 with Fig. 4.20, it is observed that the magnitudes of heat flux found from the total energy added to the liquid are in same order to that of first method but larger in values. Also, the values are in the same order of magnitude of theoretical maximum value of heat flux, $q_{max,max}$, as defined by Gambill and Lienhard [47]. An important observation from the both heat flux profiles of Fig. 4.21 and 4.22 is that, the heat flux decreases at a slower rate or with much larger time in case of hydrophobic case rather than hydrophilic case, which suggests that rate of evaporation is much less in case of hydrophobic surface and supports the earlier discussion of trajectories

of atoms as shown in Figs. 4.11 and 4.12, and number density profiles as shown in Fig. 4.16 and 4.17.

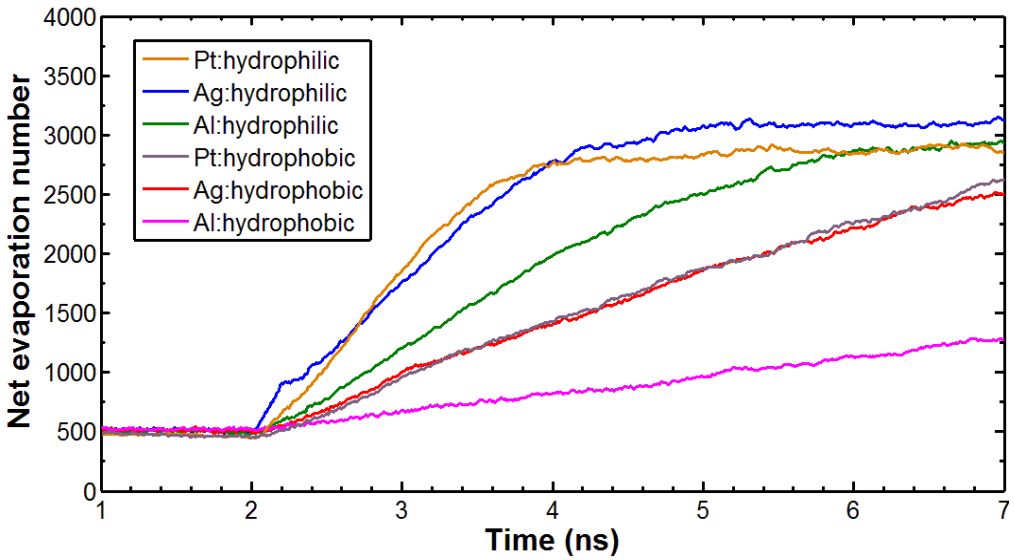

Fig. 4.23. Net evaporation number for low temperature case.

Figure 4.23 shows the net evaporation number in case of hydrophilic and hydrophobic surface in case of evaporation. The net evaporation number was calculated by counting the change of argon atoms in the vapor region. The evaporation numbers for all the surfaces in both cases remain constant up to 2 ns (during equilibrium period). For hydrophilic case as depicted in Fig. 4.23, for all surfaces under consideration, the net evaporation number increases at a higher rate than hydrophobic surface as soon as the wall temperature is increased from 90 K to 130 K. It is evident from Fig. 4.23 that for both cases, Pt-surface has the highest rate of evaporation and Al-surface has lowest rate of evaporation. For hydrophilic Ag-surface after time, t = 3.8 ns, for Pt-surface after time, t = 4.5 ns and for Al-surface after time, t = 6 ns, the number of atoms in vapor region does not change much with time which indicates that no significant the evaporation rate drastically drop after this. From the snapshots of Fig. 4.11 for hydrophilic case the thickness of non-evaporating layer is the lowest for Ag-surface and thus net evaporation number is highest for this case. As reflected in the snapshots of Fig. 4.12(c), for hydrophobic Al-surface the rate of evaporation is very low and net evaporation number verifies this fact.

4.1.3 High Temperature Case

In this case, the temperature of the solid wall was set to jump from 90K to 250K, which is far greater than the critical temperature of liquid argon. The snapshots of simulation domain during explosive boiling for hydrophilic and hydrophobic Pt, Al and Ag-surface are shown in Figs. 4.24, 4.25 respectively. From the snapshots, it is very clear that the explosive boiling phenomena occurs in case of hydrophilic surface as liquid layers are lifted up like clusters of

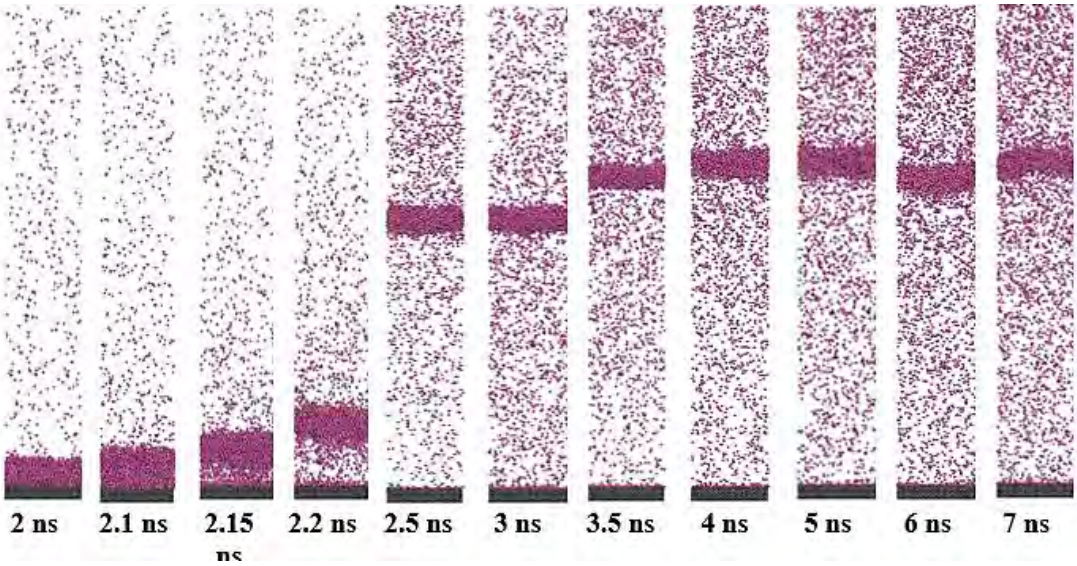

(a)

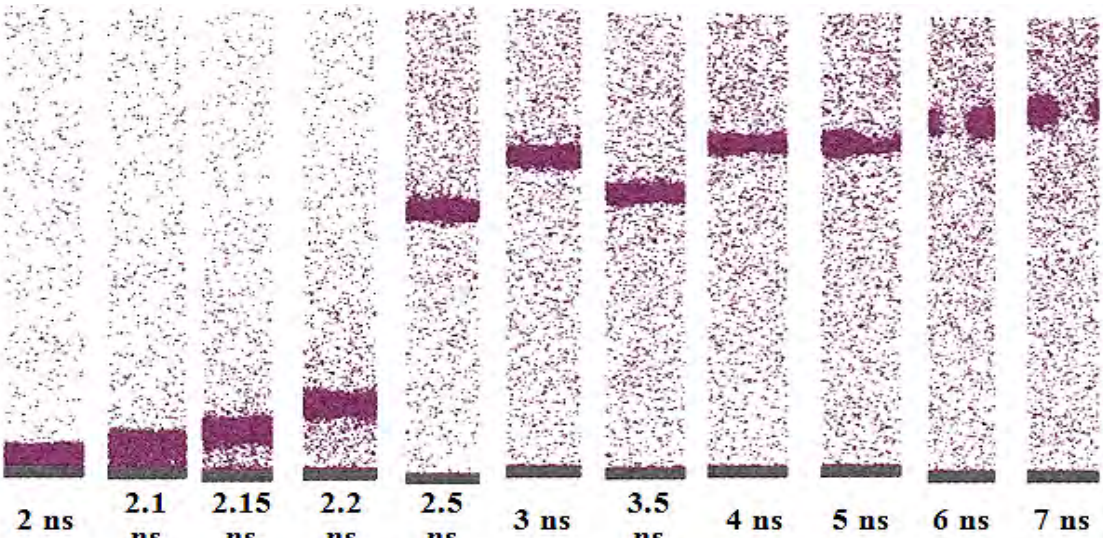

(b)

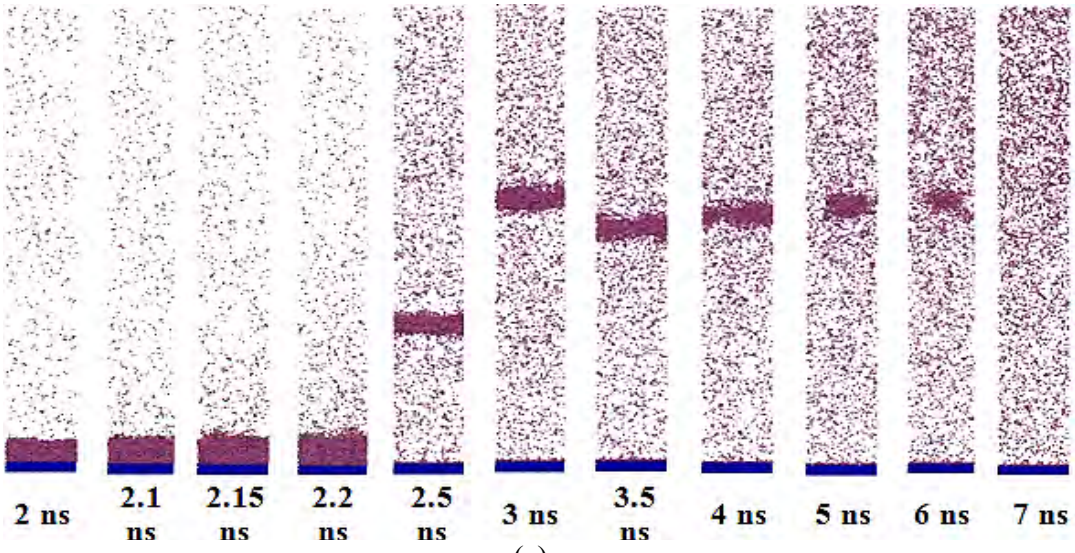

(c)

Fig. 4.24. Snapshots from the simulation domain for hydrophilic (a) Pt, (b) Ag, and (c) Al-surface for high temperature case.

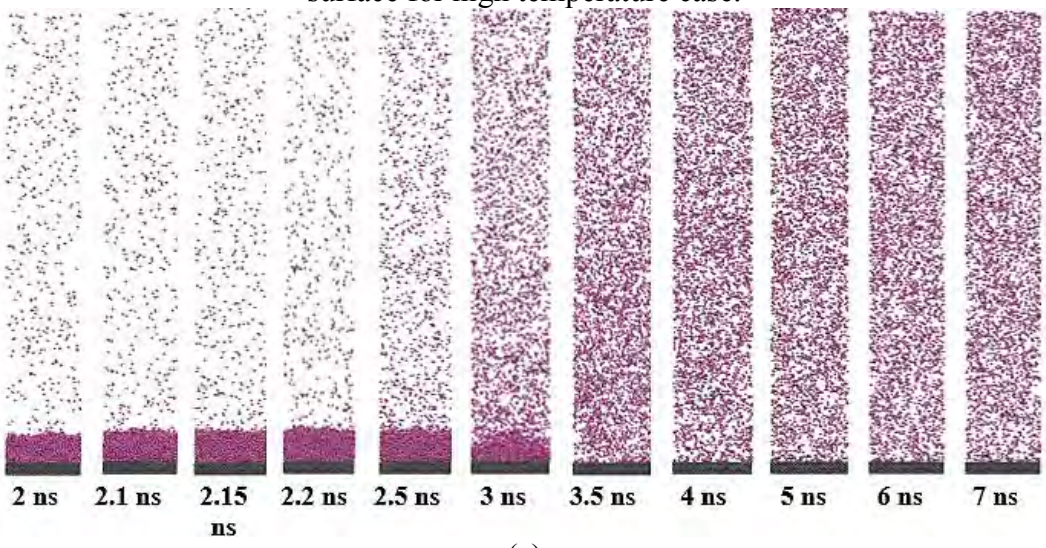

(a)

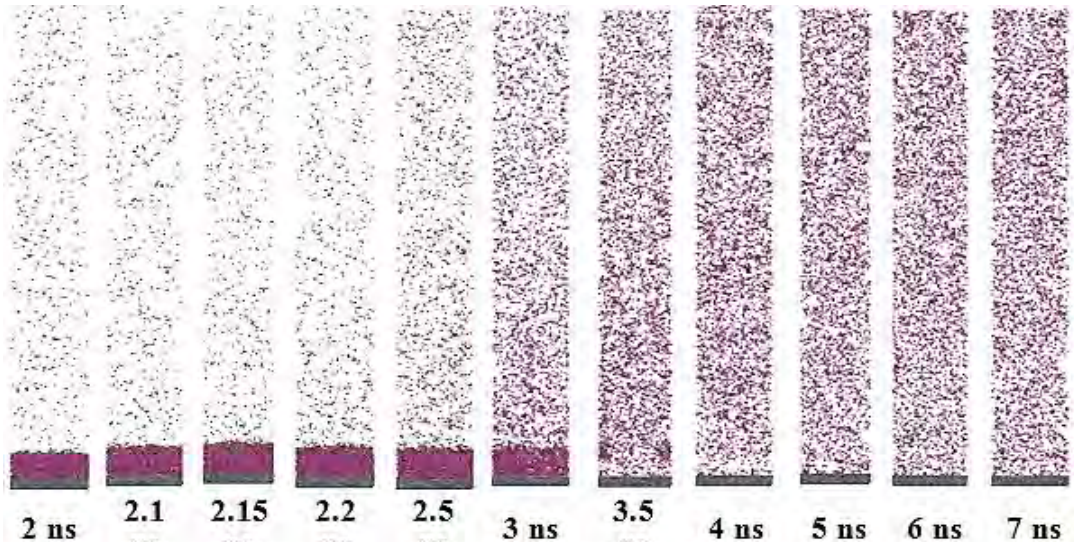

(b)

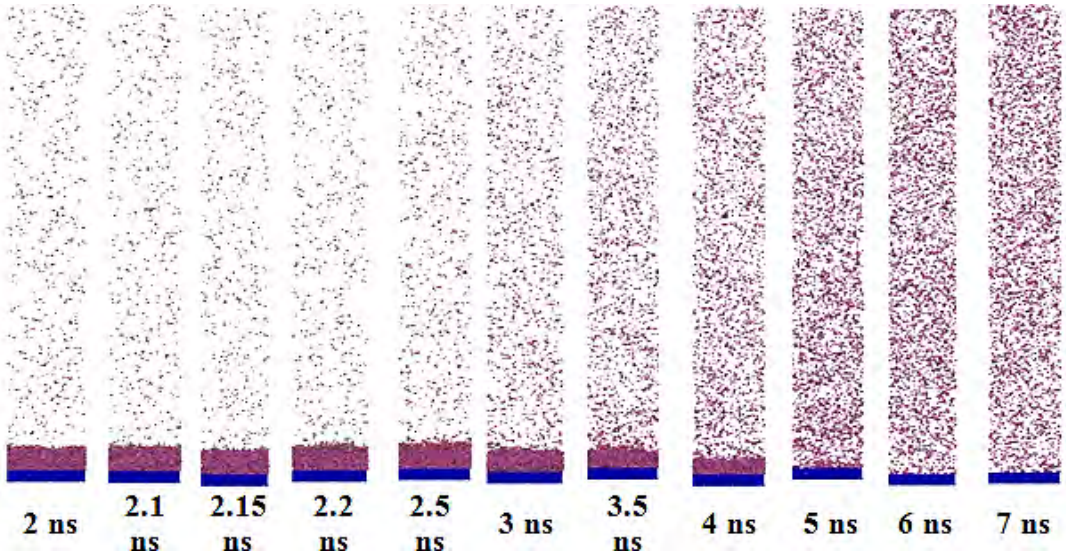

(c)

Fig. 4.25. Snapshots from the simulation domain for hydrophobic (a) Pt, (b) Ag, and (c) Al-surface for high temperature case.

atoms. In case of hydrophobic surface this phenomena explosive boiling does not occur and argon atoms leave the liquid layers as individual atoms similar to the low temperature or evaporation case.

For hydrophilic surface as shown in Fig. 4.24, as the temperature of the solid wall suddenly increased from 90 K to 250 K, liquid argon changes phase rapidly i.e. explosive boiling occurs; liquid layer adjacent to solid wall exceeds the critical temperature and instantly vaporizes while other layers above are still in the liquid phase. The pressure of this vaporized layer pushes the liquid above it and therefore, liquid layers separate from the solid wall as a large liquid cluster. From the snapshots, it is difficult to find out for which surface material the explosive boiling phenomena occurs quickly but a closer look suggests that it occurs first in case of Ag-surface, then for Pt-surface and last for Al-surface. From the number density profile of argon which is discussed later in this section this fact can be verified. In case of hydrophobic surface as shown in Fig. 4.25 the explosive boiling phenomena does not occur and argon atoms enter the vapor region as individual atom like the low temperature case or evaporation occurs but in higher rate.

The temperature history of the system for different cases is shown in Fig. 4.26. For hydrophilic surface, initially the temperature of the liquid increases very sharply, but after some time it starts decreasing. The temperature starts to decrease because of the separation of the liquid argon layer from the solid wall. As the temperature of the solid wall is increased

very rapidly from 90K to 250K, the liquid layer adjacent to the solid wall exceed the critical temperature and instantly vaporize while other layers above are still in the liquid phase. The pressure of this vaporized layer pushes the liquid above it and therefore liquid layers separate from the solid wall. The energy flow from the solid wall to the liquid is hindered by the low density vapor region adjacent to the solid wall therefore the temperature of the liquid region falls temporarily. As expected, for hydrophilic case, the quicker the occurrence of explosive boiling, the lower is the temperature of liquid argon because, if the liquid layer is detached from the solid surface quickly by the adjacent vapor layer, then less amount of energy will be transferred to the argon atoms located above. For hydrophobic surface, the temperature profiles follows the same trend as the low temperature or evaporation case, i.e. with time temperature of argon increases gradually and approaches the solid wall temperature of 250 K. For this case, the argon attains highest temperature for Pt-surface while lowest temperature is obtained for Al-surface.

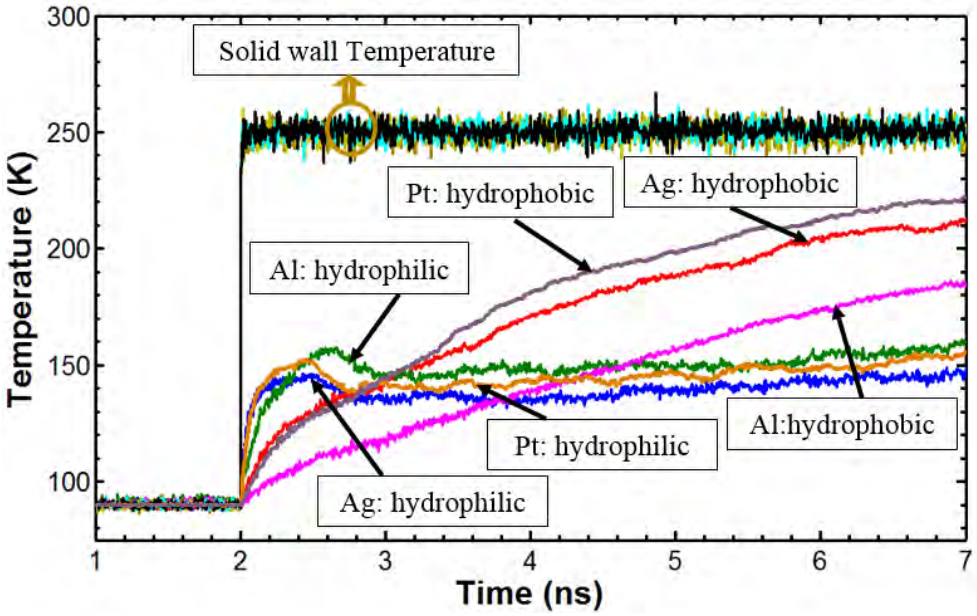

Fig. 4.26. Temperature history of argon and solid wall for high temperature case.

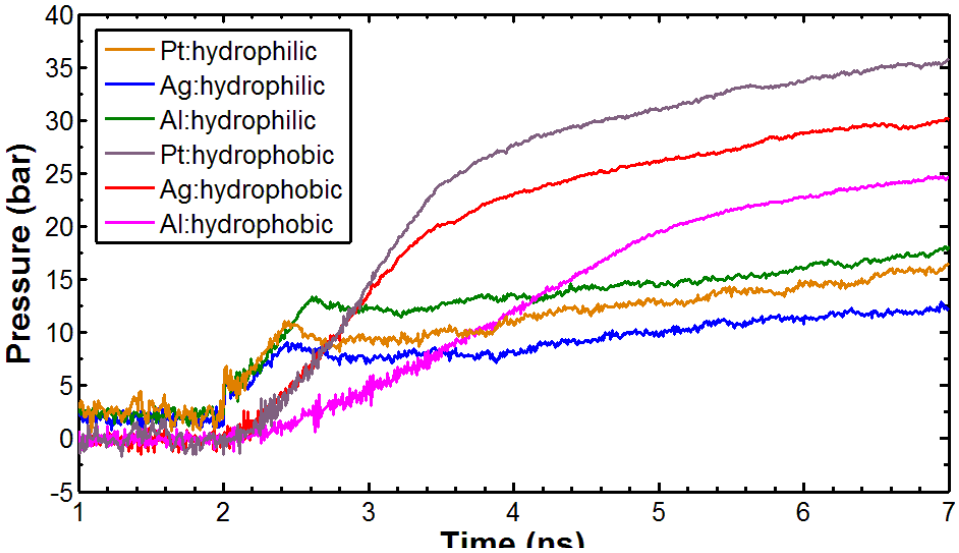

Fig. 4.27. Pressure history of the simulation domain for high temperature case.

Figure 4.27 shows the pressure history of the system for all the cases. Like the low temperature case, as the volume of the system is constraint, the pressure profiles for all the cases exactly follows the same trend of temperature profiles.

Figures 4.28, 4.29 and 4.30 show the number density profile of argon for hydrophilic Pt, Ag and Al-surface along the height of the simulation domain respectively. Irrespective of which solid surface material is used, for all the cases, as time progresses a cluster of liquid moves away from the solid surface. The region of high density peaks appearing in the curve show the locations of liquid argon cluster. As shown in Figs. 4.28, 4.29 and 4.30, a cluster of liquid starts to move away from the solid surface at time, t = 2.2 ns for Pt surface, for Ag-surface at this time the cluster had moved some distance away from the surface and for Al-surface the liquid

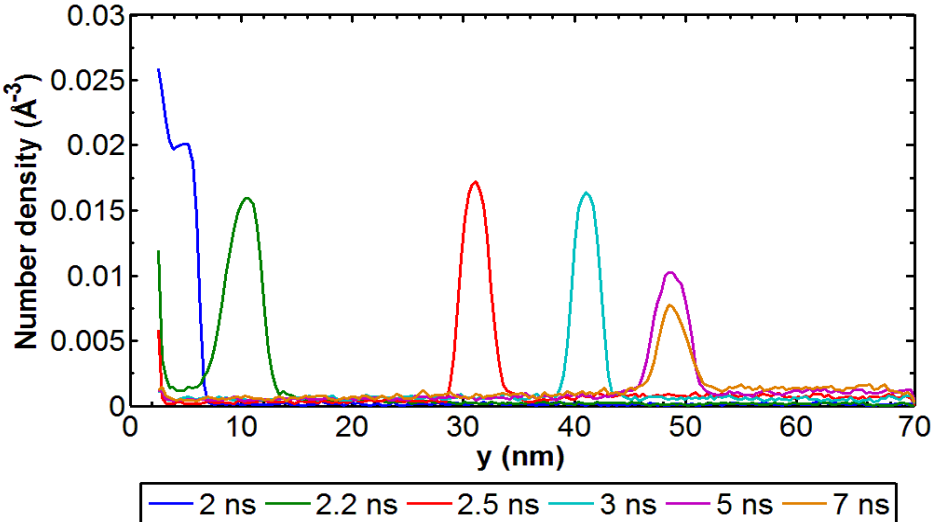

Fig. 4.28. Number density profile of argon on hydrophilic Pt-surface for high temperature case

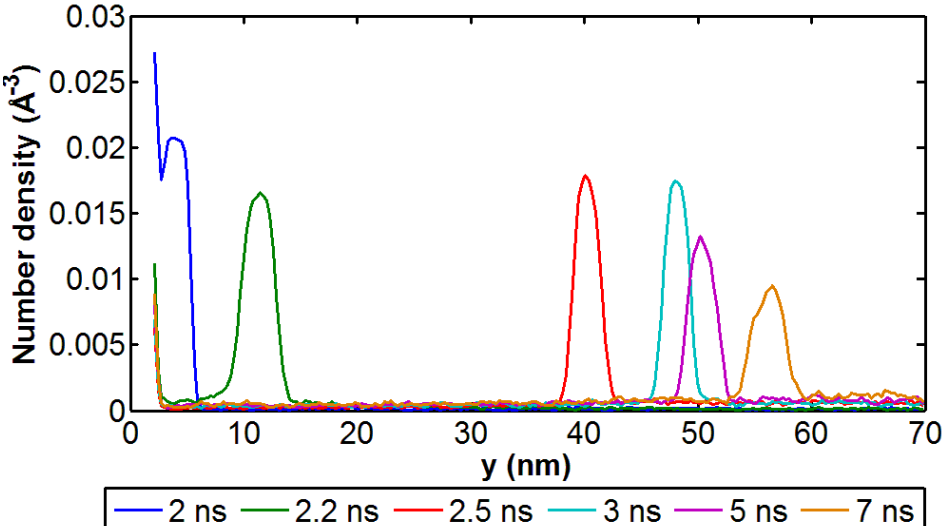

Fig. 4.29. Number density profile of argon on hydrophilic Ag-surface for high temperature case

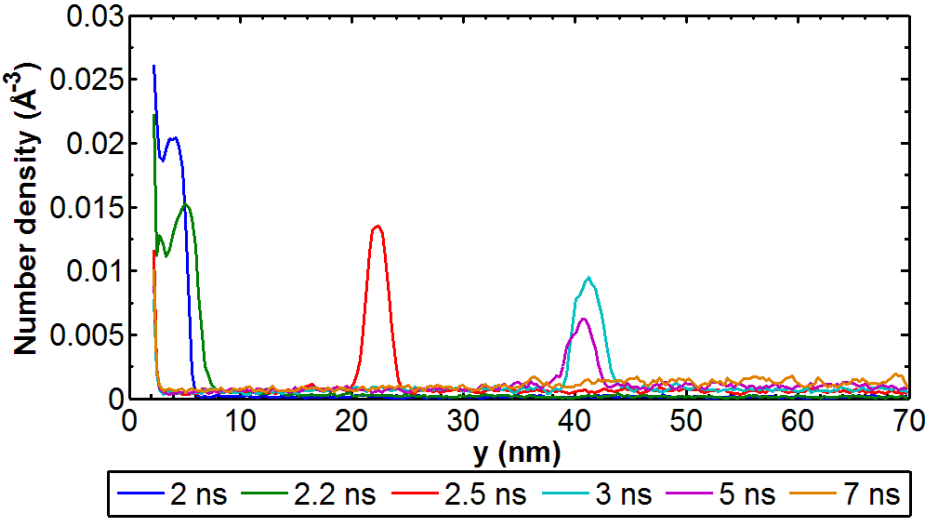

Fig. 4.30. Number density profile of argon on hydrophilic Al-surface for high temperature case

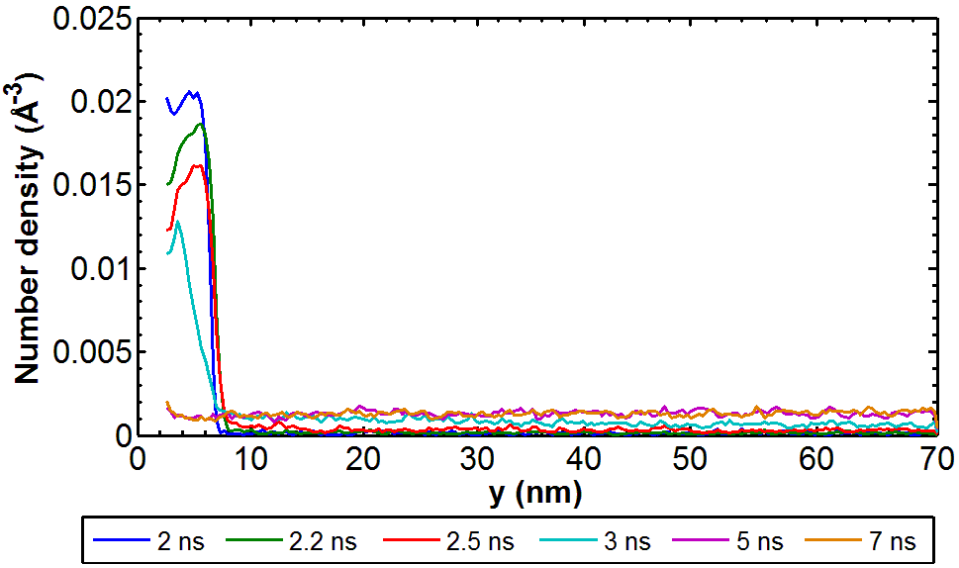

Fig. 4.31. Number density profile of argon on hydrophobic Pt-surface for high temperature case.

cluster is still adjacent to the solid surface at this time. The height of the density peaks decreases with time as argon atoms disperse from the liquid cluster to the vapor region.

Figure 4.31 shows the number density profile of argon on hydrophobic Pt-surface for high temperature case. From the figure, it is evident that, no liquid cluster is formed like the hydrophilic case rather liquid argon atoms moves away from the solid surface as individual atoms just like the low temperature or evaporation case. As higher temperature of 250 K is imposed in this case, the rate of evaporation is definitely higher than the low temperature case. Snapshots of Fig. 4.25 suggests that, the density of argon atoms becomes uniform after 3.5 ns for Pt-surface, 4 ns for Ag-surface and 5 ns for Al-surface. Figure 4.30 shows that, at t = 5 ns and 7 ns, density of argon has become uniform.

To get a closer look on effect of surface material on boiling phenomena the spatial distribution of temperature and number density of argon hydrophilic and hydrophobic Pt, Ag and Al-surface for high temperature case are shown in Fig. 4.32 and 4.33 respectively. Figure 4.32 shows that, for hydrophilic case, at t = 2.5 ns liquid cluster has moved away from the solid surface. For Al-surface, the cluster is at 20-25 nm height, for Pt-surface it is at 30-35 nm height and for Ag-surface it is at 38-43 nm height. The temperature distributions show that for the three cases, at these regions where the 'liquid cluster' is present, the temperature of argon is below the critical temperature (150 K). Below the liquid cluster region the temperature of argon atoms are higher than the critical temperature which suggests that they are in vapor phase. For the hydrophobic case, evaporation takes place and at time, t = 2.5 ns,

significant number of liquid atoms remain adjacent to the solid surface. Thus, the temperature of argon atoms is lower in this region as shown in Fig. 4.33.

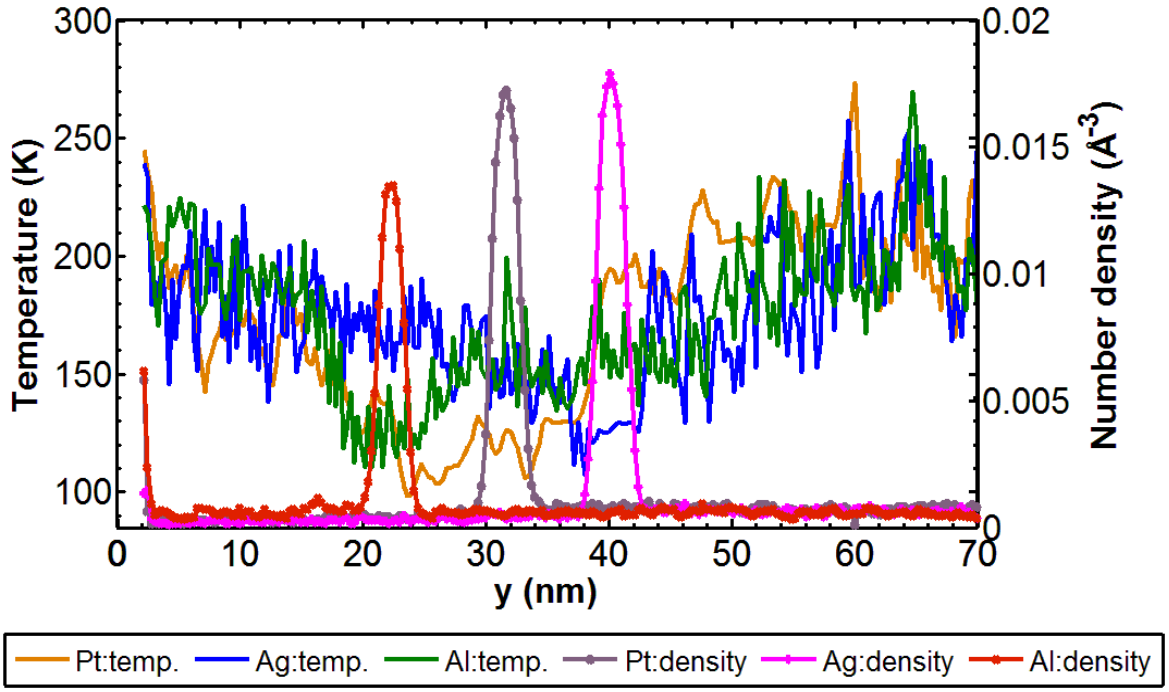

Fig. 4.32. Spatial distribution of temperature and density of argon for hydrophilic Pt, Ag, and Al-surface respectively for high temperature case at 2.5 ns.

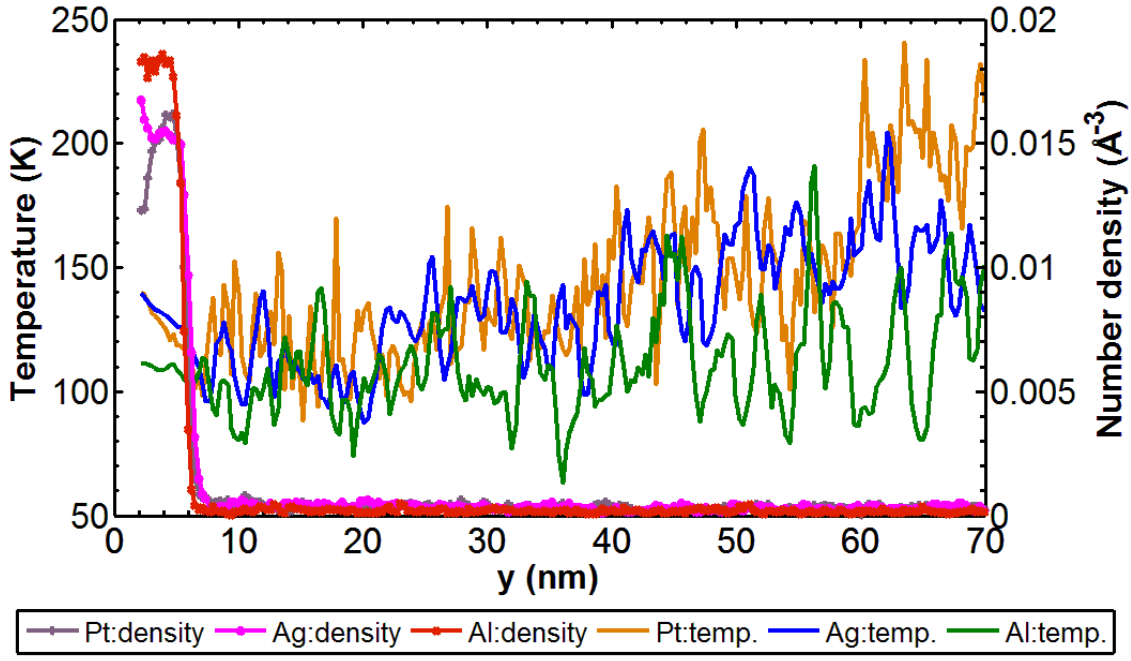

Fig. 4.33. Spatial distribution of temperature and density of argon for hydrophobic Pt, Ag, and Al-surface respectively for high temperature case at 2.5 ns.

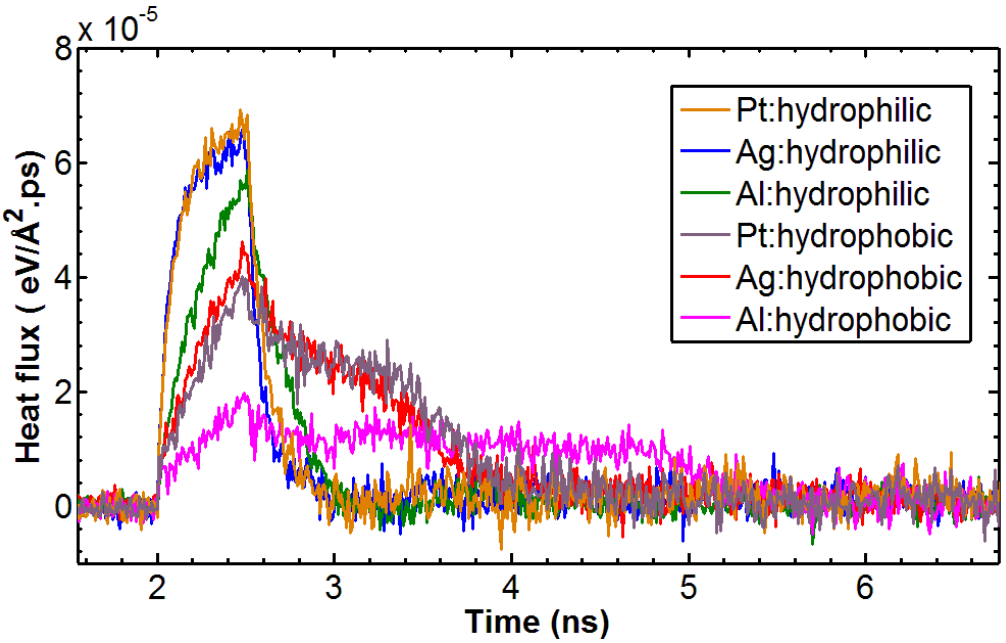

Fig. 4.34. Heat flux normal to solid wall for high temperature case.

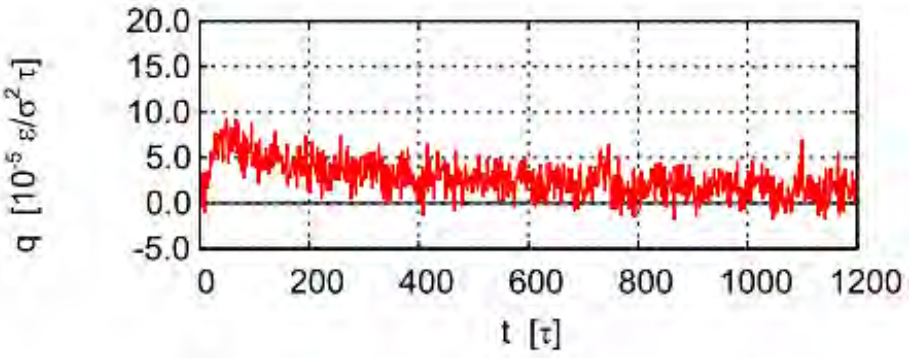

(a)

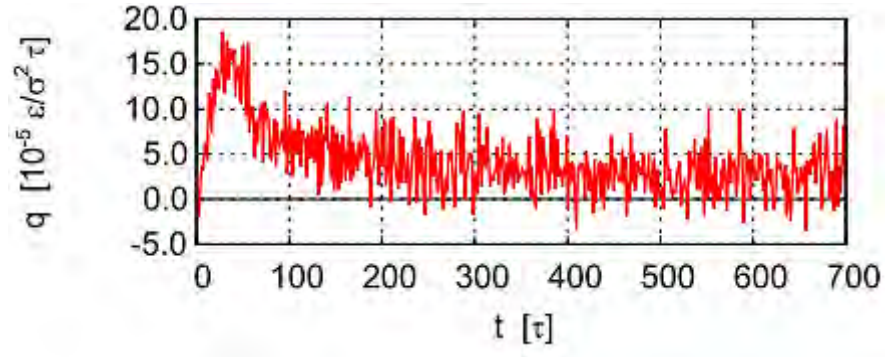

(b)

Fig. 4.35. Comparison of heat flux for different surface wetting conditions as shown in Yamamoto and Matsumoto [38], (a) for, $\varepsilon_{liquid\text{-}solid} / \varepsilon_{liquid\text{-}liquid} = 0.5$, hydrophobic case, (b) for, $\varepsilon_{liquid\text{-}solid} / \varepsilon_{liquid\text{-}liquid} = 1.5$, hydrophilic case.

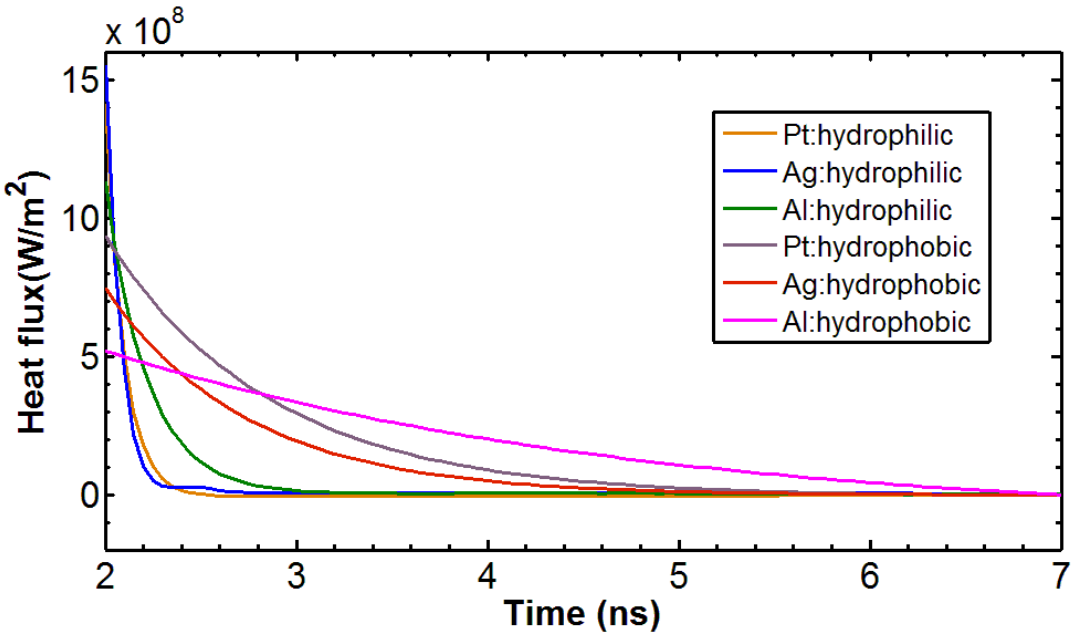

Fig. 4.36. Heat flux calculated from energy of the liquid for high temperature case.

Figure 4.34 depicts the heat flux normal to the solid wall for all the cases for the high temperature case. The trend of the heat flux profiles are similar to that of the low temperature case but magnitudes are much higher. For hydrophilic case, at the moment when the explosive boiling starts to take place, a huge amount of heat is transferred to the liquid adjacent to solid and after that there is a large drop of heat flux as indicated in Fig. 4.34. For hydrophobic case, similar profiles are observed but with smaller peaks and heat flux decreases more slowly. As expected, the value of heat flux is higher in case of hydrophilic surface and maximum in case of Pt-surface, which is around 7×10^{-5} eV/A^{2}ps or 1120 MW/m^2 which is about 2 times greater than the magnitude of heat flux calculated during low temperature case (Fig. 4.20). For hydrophobic surface, the maximum magnitude of heat flux for high temperature case is around 4.2×10^{-5} eV/A^{2}ps or 672 MW/m^2 for Ag-surface which is about 2.8 times than the maximum value of heat flux for low temperature case. As shown in the snapshots of Fig. 4.24, in case of hydrophilic case, explosive boiling occurred in case of Pt, Ag and Al surface. From Fig. 4.34, it is observed that, when explosive boiling occurs the magnitude of heat flux increases considerably and the value reaches one order of magnitude higher than the theoretical maximum value of heat flux, $q_{max,max}$ as proposed by Gambill and Lienhard [47]. The profiles of heat flux of Fig. 4.34 shows excellent agreement with the study performed by the Yamamoto and Matsumoto [38] as depicted in Fig. 4.35. Similar to this study Yamamoto and Matsumoto [38] observed that, heat flux increases with the increase of solid-liquid interaction potential i.e. surface wetting condition.

Heat flux calculated from the energy added to liquid for high temperature case is shown in Fig. 4.36. These profiles also shows that the hydrophilic surface transfers energy more effectively, however, the magnitudes of heat flux for both hydrophilic and hydrophobic cases is much larger compared to the result of Fig. 4.34. This anomaly occurs because, a very high heat flux is suddenly added within a very short time when explosive boiling begins and thus the energy profile consists a large jump of magnitude of energy in this region and when the heat flux is calculated from the slop of the energy profile it fails to capture the true nature of the phenomena. Similar to the Fig. 4.34, the magnitudes of heat flux during explosive boiling which occurs in case of hydrophilic surface found to be one order of magnitude higher than the theoretical maximum of heat flux, $q_{max,max}$ as defined by Gambill and Lienhard [47], but for hydrophobic case the magnitudes of the heat flux are in the order of $q_{max,\ max}$. In hydrophobic case, as shown in the snapshots of Fig. 4.25, explosive boiling did not occur and instead normal boiling or evaporation took place but at a higher rate. Therefore, heat flux profiles of both Figs. 4.34 and 4.36 show that, for hydrophilic surface the rate of decrease of heat flux is very rapid and within 3 ns the magnitude of heat flux reaches to zero due to the occurrence of explosive boiling phenomena. But for hydrophobic surface, as evaporation takes place the profiles of heat flux as depicted in Figs. 4.34 and 4.36 are similar to the profiles of low temperature case as shown in Figs. 4.20 and 4.21.

Figure 4.37 shows the net evaporation number for high temperature case. As expected, the number of argon atoms in vapor region remains constant during equilibrium period. When the temperature of the solid wall is increased from 90 K to 250 K, for hydrophilic surface explosive boiling takes place and as soon as the liquid cluster moves away from the solid surface, the number of argon atoms increases almost instantaneously to a higher value. From the figure, it is clear that, for hydrophilic surface the explosive boiling takes place first in case Ag-surface, second in case of Pt-surface and last in case of Al-surface. For hydrophobic surface evaporation takes place, therefore the number of atoms in vapor region increases slowly or rather gradually. For the hydrophobic case the rate of evaporation follows the same sequence, highest in case of Ag-surface and lowest in case of Al-surface. The number of atoms for all the cases after 7 ns is same, which suggests that there is no existence of non-evaporating layer in case of high temperature case.

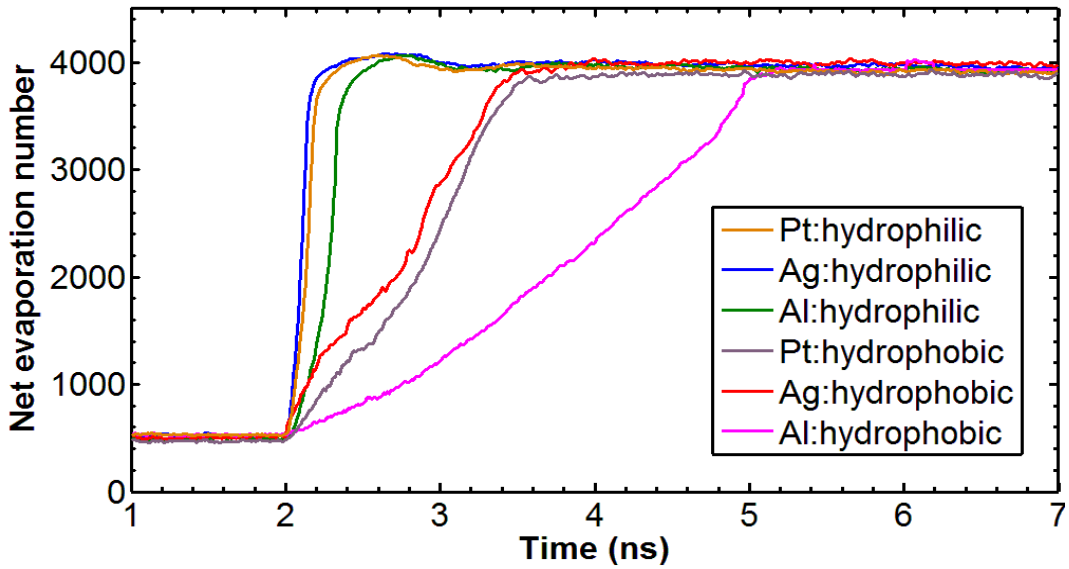

Fig. 4.37. Net evaporation number for high temperature case.

4.1.4 Summary

By performing molecular dynamics (MD) simulation the boiling phenomena for a thin liquid argon film over a solid surface were closely studied for different solid surface material namely platinum, silver and aluminum and wetting conditions (hydrophilic and hydrophobic) by considering two different degree of superheat.

The heat transfer rate from a solid surface to the liquid significantly increases with the increase of solid-liquid interaction potential or in other words, with the increase of the surface wettability for both low and high temperature case.

The effect of solid surface material on evaporation and explosive boiling is less significant compared to the effect of the surface wettability. Among the three materials that have been considered in this study, aluminum was the least effective. Platinum and silver showed similar characteristics.

For low temperature case, non-evaporating layer has been observed in all the cases but for high temperature case no non-evaporating layer was observed.

For high temperature case, explosive boiling was observed in case of hydrophilic surface, but for hydrophobic surface evaporation was observed.

From heat flux point of view, the transfer of heat in case of hydrophilic surface was much higher than the hydrophobic surfaces for both low and high temperature cases.

4.2. NEMD Simulation of Thin Film Liquid on Nanostructured Surface

Use of nanotextured surface or nanostructures in boiling phenomena has received significant attention from the researchers in recent times as many research have revealed the fact that nanostructures can be a very effective way for enhancing heat transfer during boiling. Thus studies performed by NEMD simulation involving nanostructured surface with different patterns, size, and shape could illustrate the behavior of boiling phenomena from nanoscale point of view.

In this study, argon is used as the liquid and platinum is used as the solid wall material. Two different cases are considered based on the surface wetting condition; hydrophilic ($\varepsilon_{Ar\text{-}Pt}/\varepsilon_{Ar\text{-}Ar}$ = 2) and hydrophobic ($\varepsilon_{Ar\text{-}Pt}/\varepsilon_{Ar\text{-}Ar}$ = 0.5) surface. Also two different jump temperature are considered, for low temperature case, temperature of the solid wall was increased from 90 K to 130 K and for high temperature case, it was increased from 90 K to 250 K. Nanostructures which are placed on top of the flat surface have the shape of protruded rectangular block. Three different heights (1.5 nm, 3.0 nm and 4.5 nm) were considered for the nanostructures to study the effect of nanostructure on boiling phenomena. Fig. 4.38 shows the wall configurations considered in the present study by incorporating the nanostructures. The three phase molecular system considered in this study has a dimension of 7.4 nm × 60.0 nm × 7.4 nm (x × y × z). The methodology which was followed to construct the simulation domain and validation of the model were achieved in the same manner as it is discussed in section 4.1.1

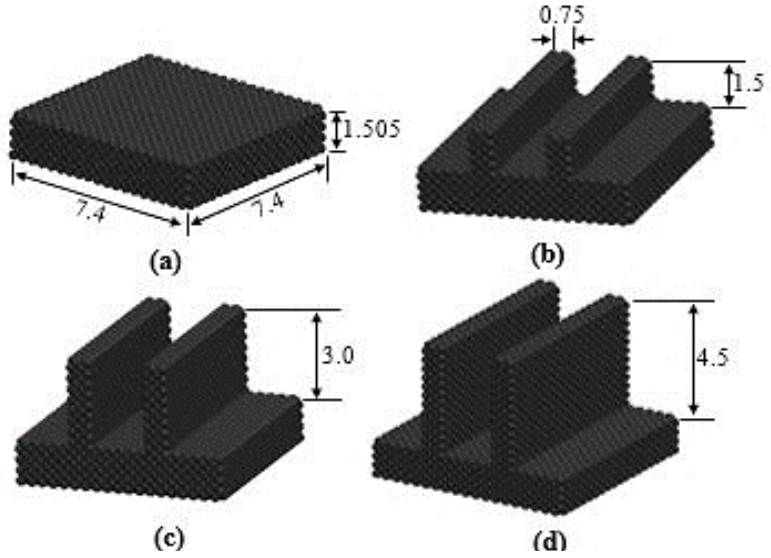

*all dimensions are in nm

Fig. 4.38. Solid wall configurations, (a) flat surface; (b) nanostructured surface-1; (c) nanostructured surface-2; (d) nanostructured surface-3

4.2.1 Low Temperature Case

When the temperature of the solid wall is suddenly increased from 90 K to 130 K, in case of both hydrophilic and hydrophobic surface liquid argon atoms leave the solid surface and enter the vapor region as individual atoms and evaporation takes place as shown in the snapshots of the simulation domain of Fig. 4.39 and 4.40 respectively. For the hydrophilic surface as shown in Fig. 4.39, addition of nanostructures decreases the number of argon atoms in the vapor region than the flat surface. As the height of nanostructures are increased from 1.5nm to 3 nm and then to 4.5 nm, the number of atoms leaving the liquid layers and entering the vapor region decreased significantly. The reason behind this fact is that as hydrophilic surface has more solid-liquid interaction potential, the liquid atom layer just adjacent to solid surface sticks with it forms a crystal like layer termed as the 'non-evaporating layer'. From Fig. 4.39, it is observed that, as height of the nanostructures are increased, more and more argon atoms contribute to form the non-evaporating layer just adjacent to the solid surface. For hydrophilic surface, the scenario is just opposite to that of hydrophilic surface as shown in Fig. 4.40. As the height of the nanostructures are increased, more argon atoms moves away from the liquid layer to the vapor region. As solid-liquid interaction potential is low in case hydrophobic surface, the energy transfer rate from solid to liquid surface is less than hydrophilic surface, therefore, for flat hydrophobic surface, after 7 ns still significant number of argon atoms remain in liquid layer as shown in Fig. 4.40(a). But because of low solid-liquid interaction, argon atoms do not stick or stay adjacent to the solid surface as much as it was the case of hydrophilic surface, therefore, no non-evaporating layer is formed in this case. Thus, addition of nanostructure in case of hydrophobic surface means there is more solid surface area in contact with liquid layers and more energy is transferred than the flat surface. Also due to the absence of non-evaporating layer, more argon atoms entered into vapor region and more evaporation takes place as the height of the nanostructure is increased.

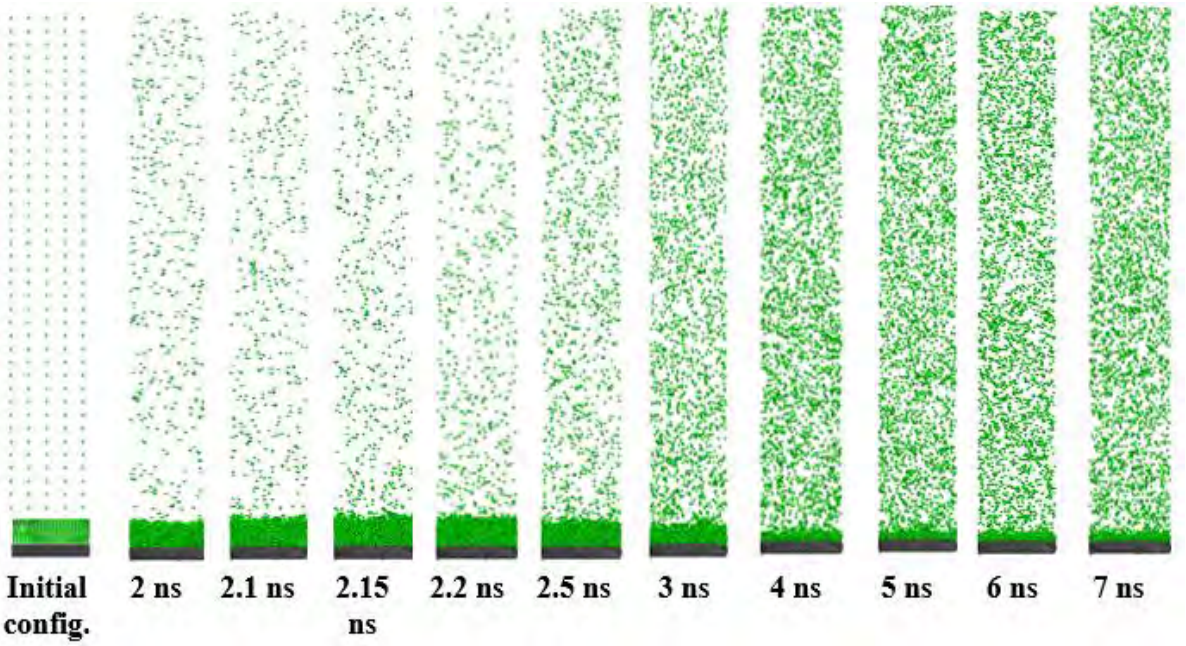
Initial config.
2 ns
2.1 ns
2.15 ns
2.2 ns
2.5 ns
3 ns
4 ns
5 ns
6 ns
7 ns

(a)

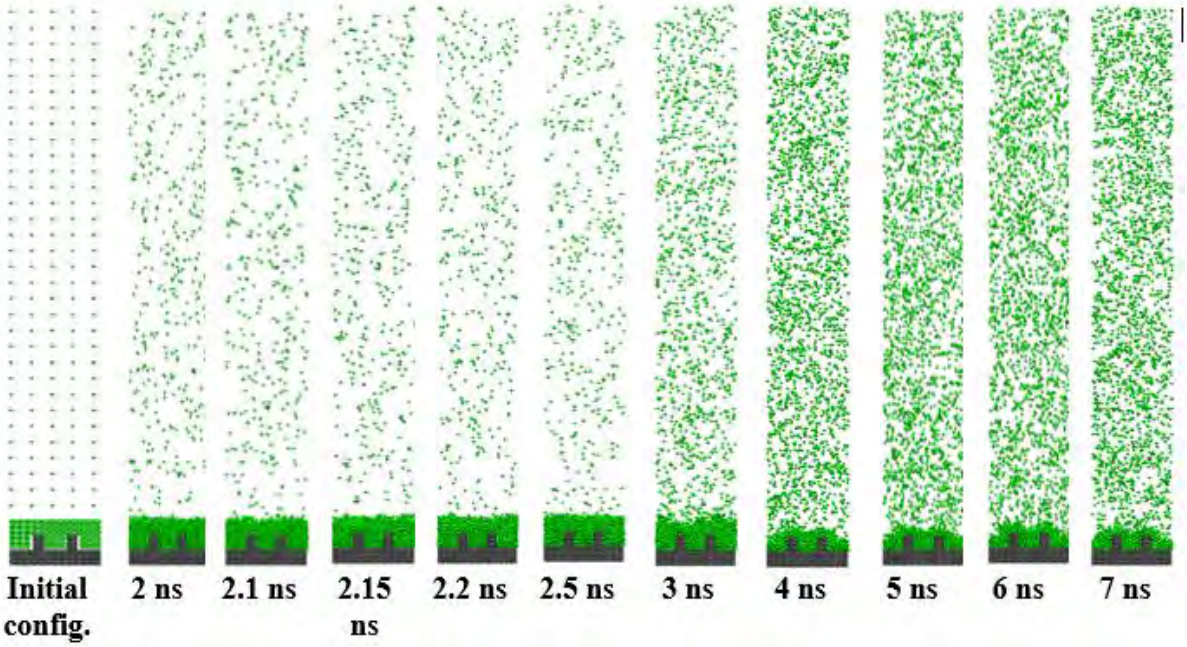
Initial config.
2 ns
2.1 ns
2.15 ns
2.2 ns
2.5 ns
3 ns
4 ns
5 ns
6 ns
7 ns

(b)

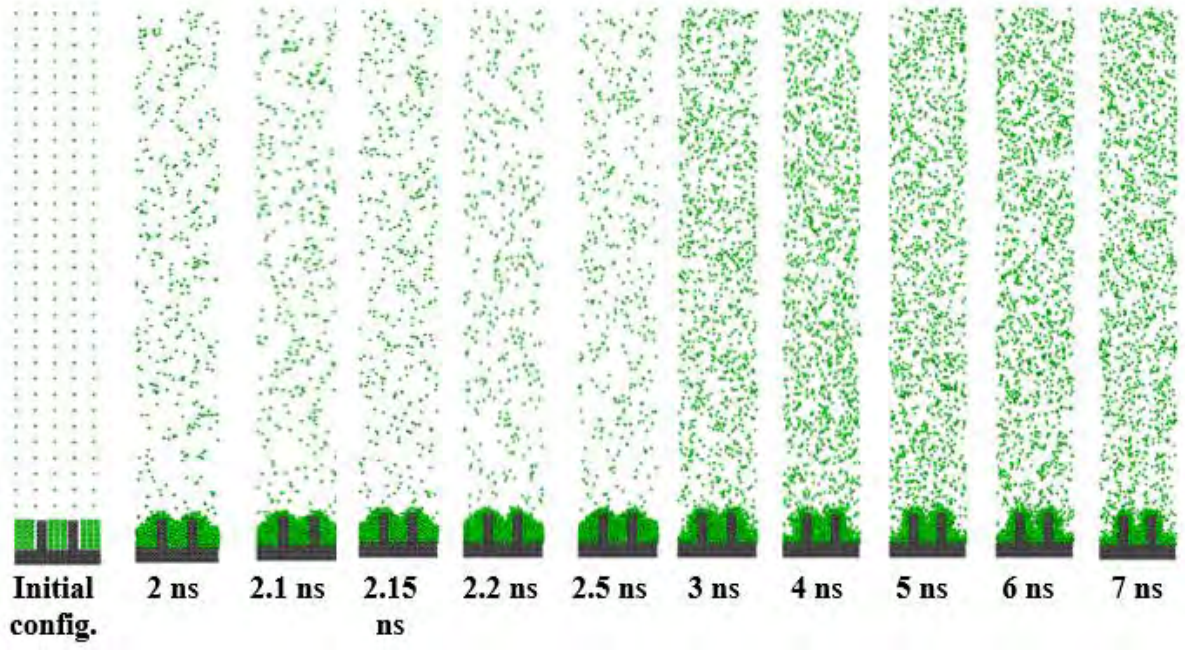

(c)

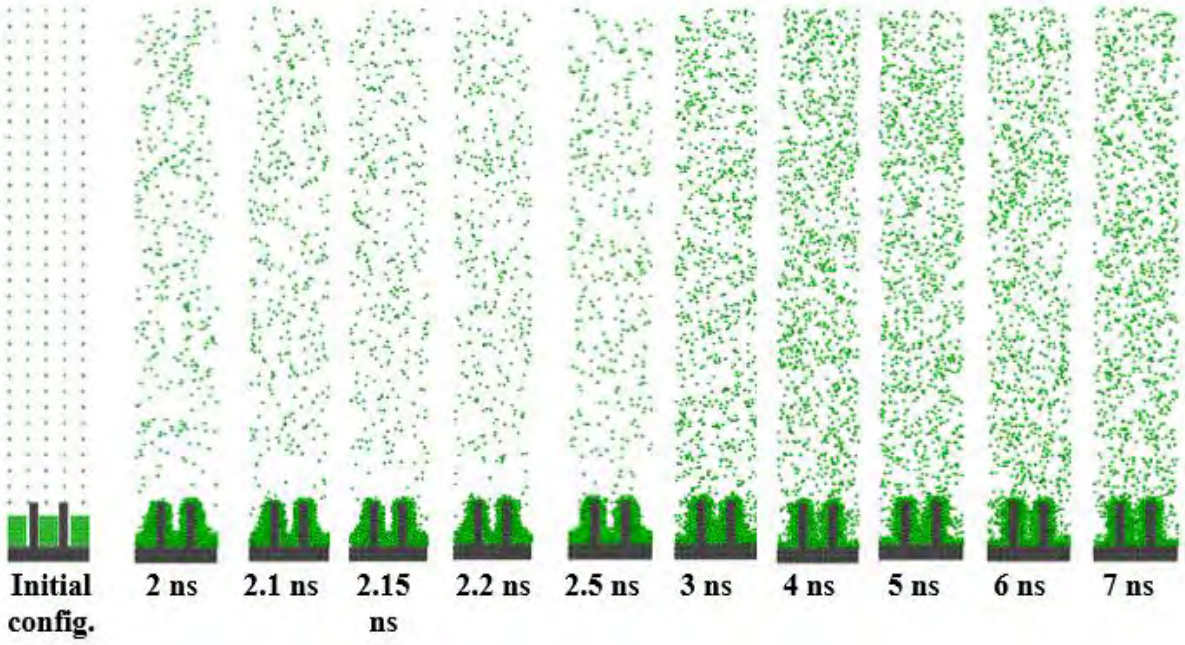

(d)

Fig. 4.39. Snapshots from the simulation domain for hydrophilic surface, (a) flat surface, (b) surface-1, (c) surface-2, (d) surface-3 for low temperature case

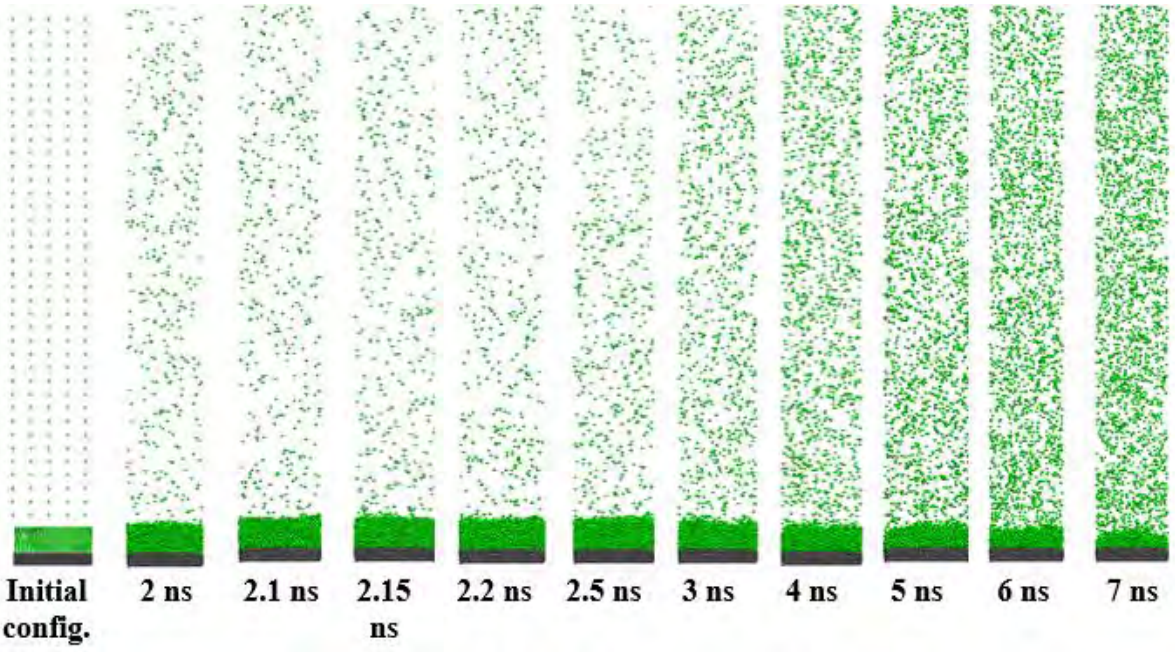
Initial config.
2 ns
2.1 ns
2.15 ns
2.2 ns
2.5 ns
3 ns
4 ns
5 ns
6 ns
7 ns

(a)

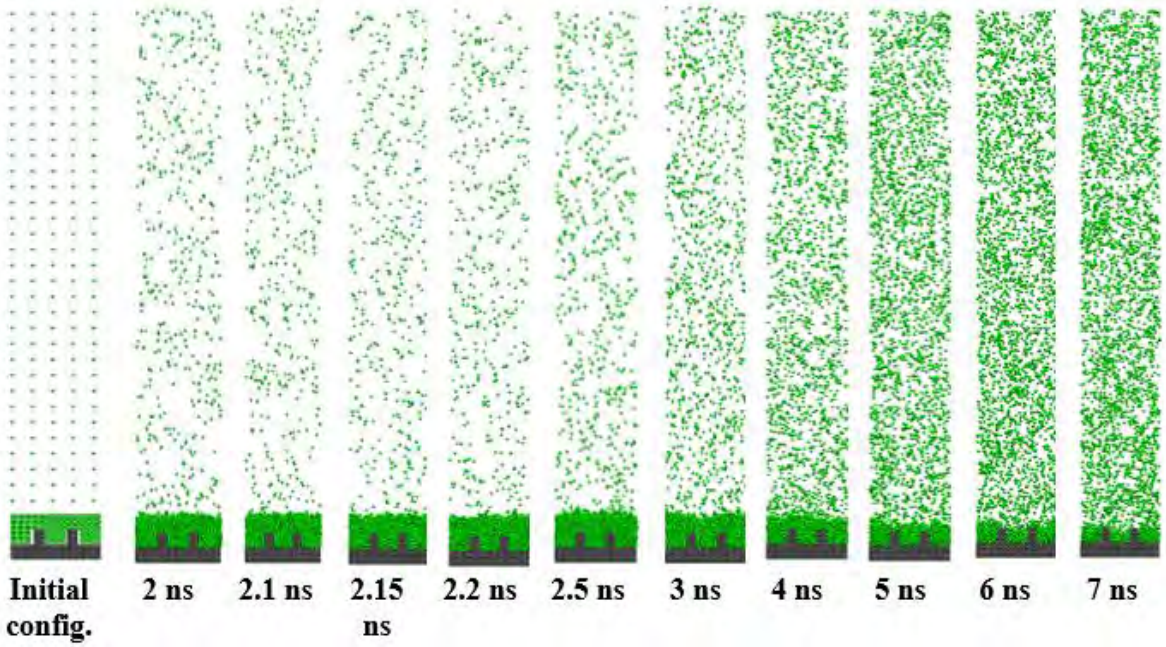
Initial config.
2 ns
2.1 ns
2.15 ns
2.2 ns
2.5 ns
3 ns
4 ns
5 ns
6 ns
7 ns

(b)

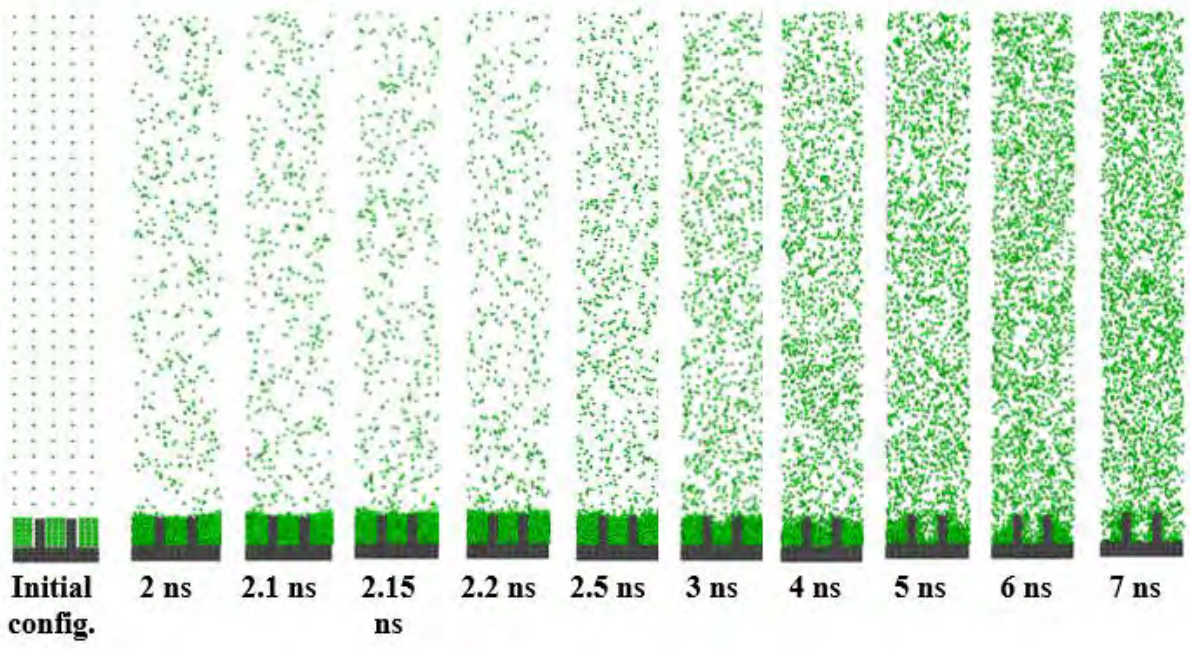

(c)

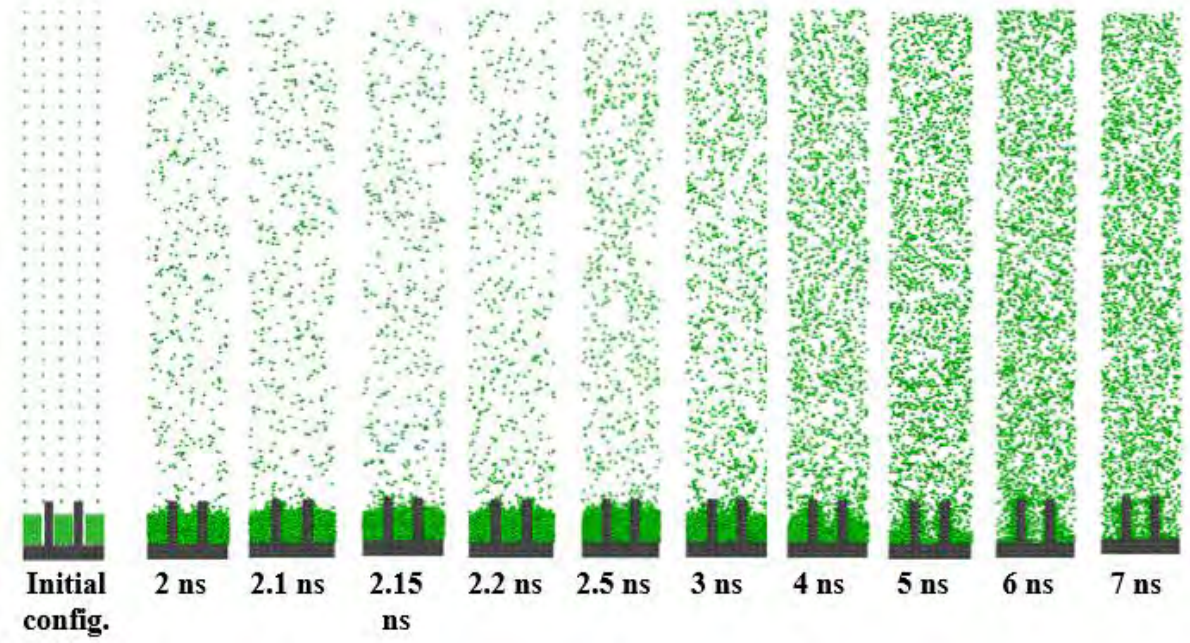

(d)

Fig. 4.40. Snapshots from the simulation domain for hydrophobic surface, (a) flat surface, (b) surface-1, (c) surface-2, (d) surface-3 for low temperature case

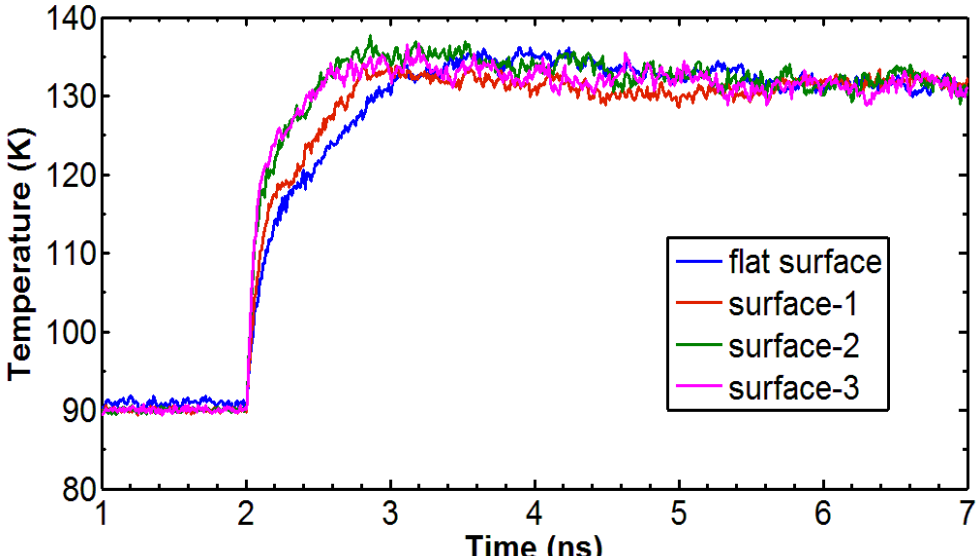

Fig. 4.41. Temperature history of argon (Ar) for hydrophilic surface for low temperature case.

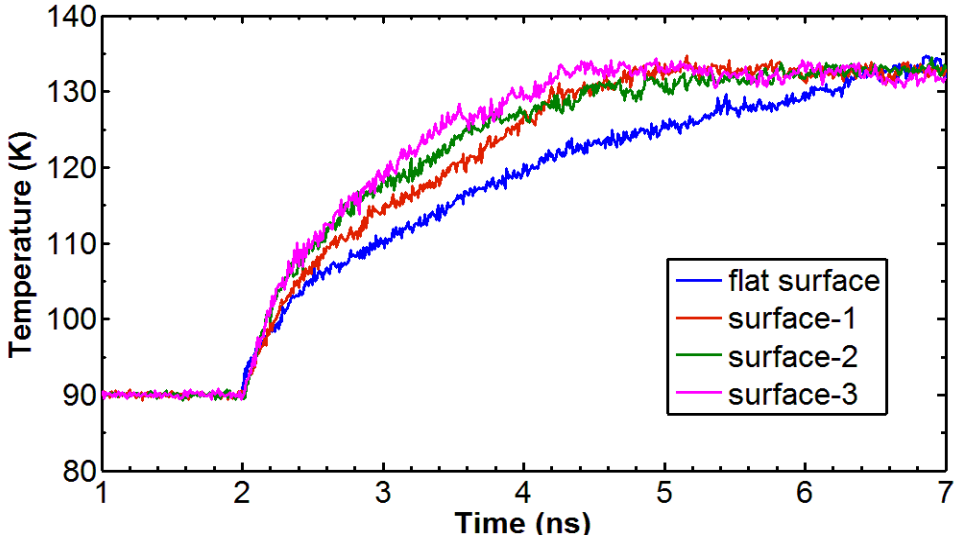

Fig. 4.42. Temperature history of argon (Ar) for hydrophobic surface for low temperature case

The temporal variation of temperature of argon for hydrophilic and hydrophobic surface are shown in Fig. 4.41 and 4.42 respectively. It can be readily observed from Fig. 4.41 and 4.42 that the temperature of liquid argon reaches to equilibrium with the solid wall much quicker in case of hydrophilic surface than hydrophobic surface which suggests that the energy is transferred from the solid surface to the liquid argon layer much quickly in case of hydrophilic surface due to the higher solid-liquid interactions. Figure 4.41 and 4.42 also suggests that, for both hydrophilic and hydrophobic cases, as the height of the nanostructure is increased, the temperature of argon reaches to equilibrium with the solid surface more quickly. The interaction between the solid and liquid atoms increases due to the presence of nanostructures, which results faster energy transfer from the solid wall to the liquid molecules that increases the temperature.

Figures 4.43 and 4.44 show the pressure history of the simulation domain for hydrophilic and hydrophobic surface respectively. The volume of the system is constraint, thus with the increase of the temperature pressure of the domain increases and pressure profiles follow the trend of the temperature profile. Figure 4.43 shows that, for hydrophilic surface like temperature profile, the pressure of the simulation domain reaches to equilibrium quickly as the height of the nanostructure is increased. For hydrophobic surface as shown in Fig. 4.44, pressure profiles do not reaches to equilibrium rather continue to increase with time.

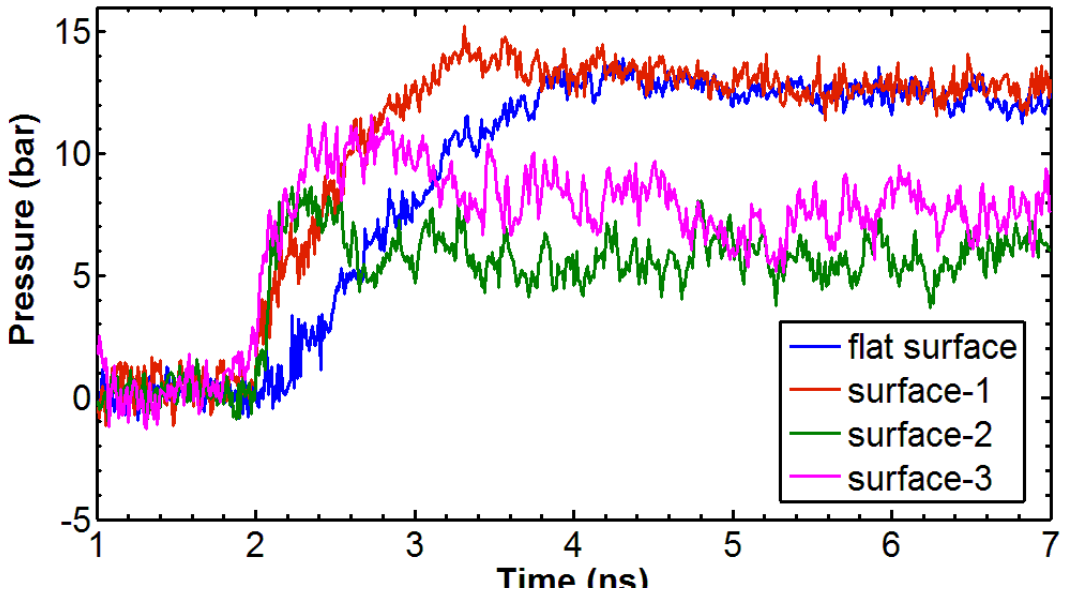

Fig. 4.43. Pressure history of the simulation domain for hydrophilic surface for low temperature case

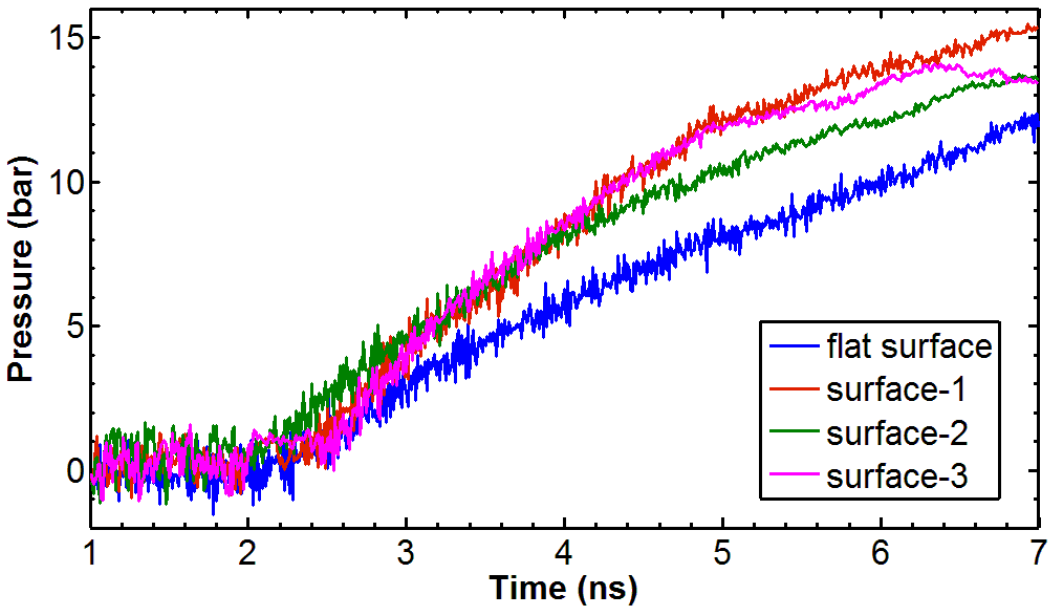

Fig. 4.44. Pressure history of the simulation domain for hydrophobic surface for low temperature case

The number density profile for hydrophilic and hydrophobic case respectively for flat Pt-surface at different simulation time has been discussed in detail in the previous section. As time progresses argon atoms leave the liquid layers and number density profiles near the liquid layer get flatter. Similar profiles can be found for nanostructured surface-1, surface-2 and surface-3. Figures 4.45, 4.46 and 4.47 show the number density profiles for hydrophilic surface at time, t = 3 ns, 5 ns and 7 ns respectively. The existence of non-evaporating layer can be observed from these figures in case of hydrophilic surface. The thickness of the number density profile increases with the height of the nanostructure at the region where liquid layers are adjacent to the solid surface. From t = 3 ns to 5 ns, for nanostructured surface-1, surface-2 and surface-3, there is a growth of argon atoms adjacent to the solid surface as the number density profiles get thicker. From t = 5 ns to 7 ns, there is very little change of number density, thus the non-evaporating layer has become completely settled adjacent to the solid surface. As mentioned earlier, because of the existence of non-evaporating layer in case of nanostructured surface, number of atoms in the vapor region is higher in case of flat hydrophilic surface.

For hydrophobic case, the number density profile at t = 3 ns, t = 5 ns and t= 7 ns are shown in Figs. 4.48, 4.49 and 4.50 respectively. Argon atoms leaves the liquid layers more as the height of nanostructures are increased. So, increase of nanostructure height increases the rate of evaporation, because of higher solid-liquid interaction. From t = 3 ns to 5 ns, the thickness of density profiles adjacent to solid surface are decreased for all the cases. Observing the number density profile at t = 7 ns, it can be said that there is no non-evaporating layer in case of hydrophobic surface.

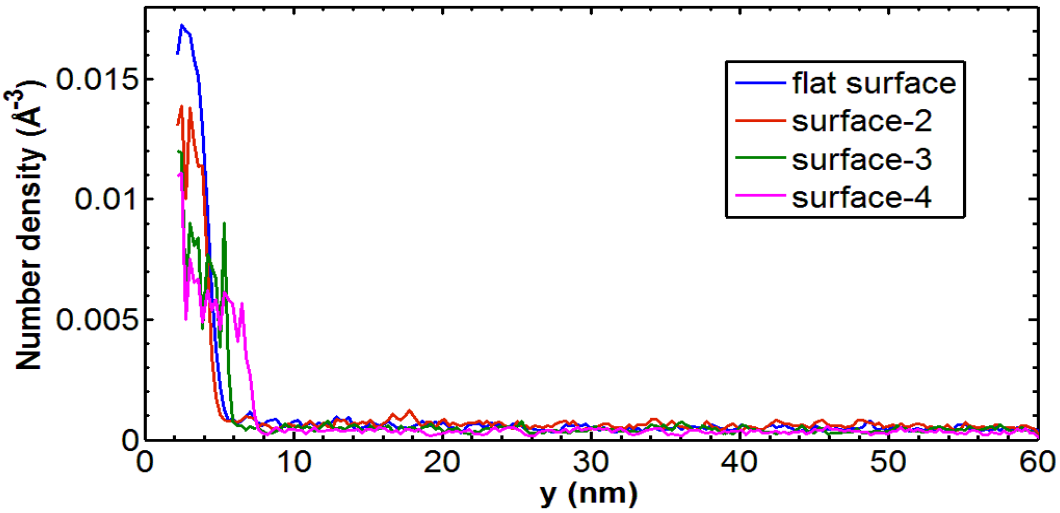

Fig. 4.45. Number density profile of argon at 3 ns for hydrophilic surface for low temperature case

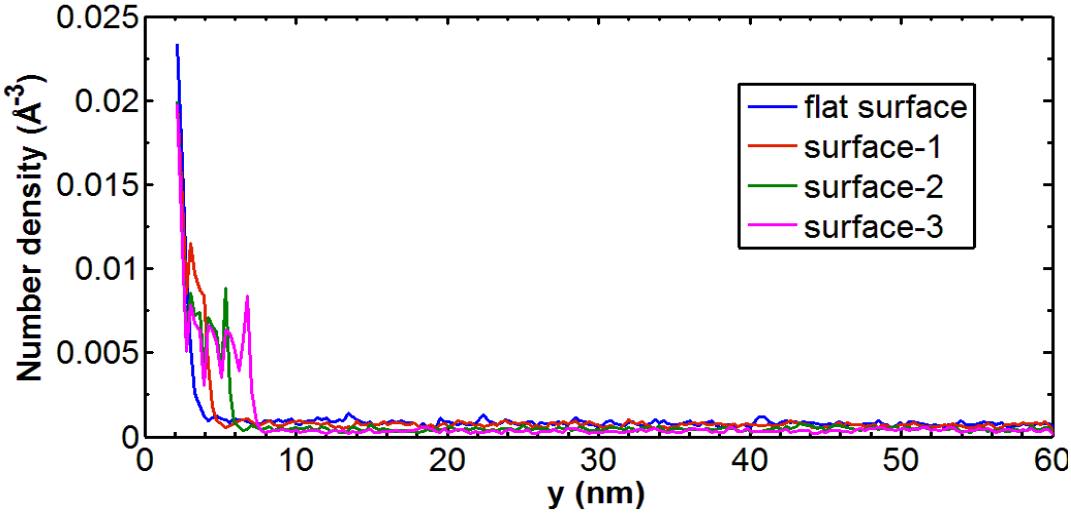

Fig. 4.46. Number density profile of argon at 5 ns for hydrophilic surface for low temperature case

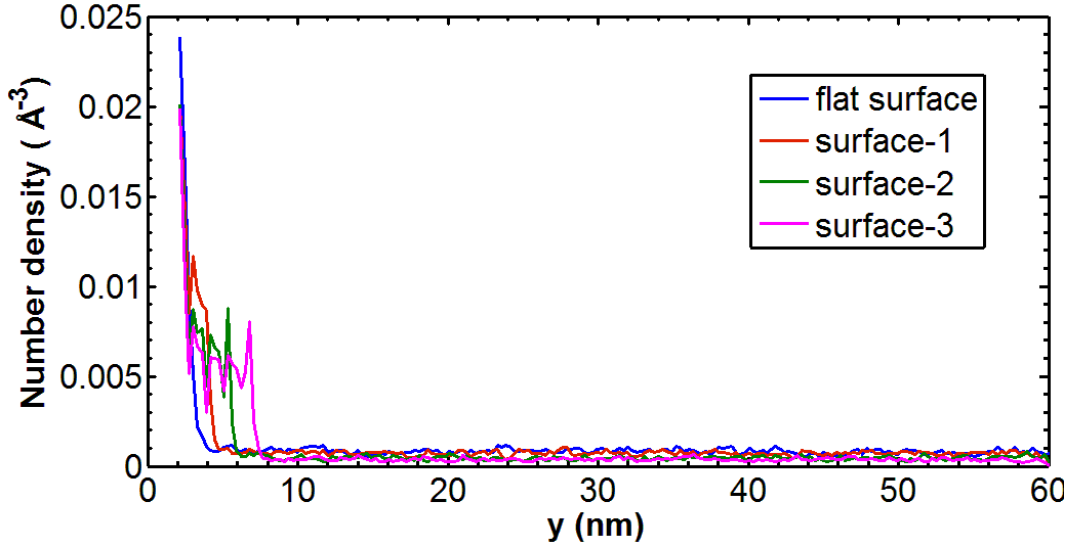

Fig. 4.47. Number density profile of argon at 7 ns for hydrophilic surface for low temperature case

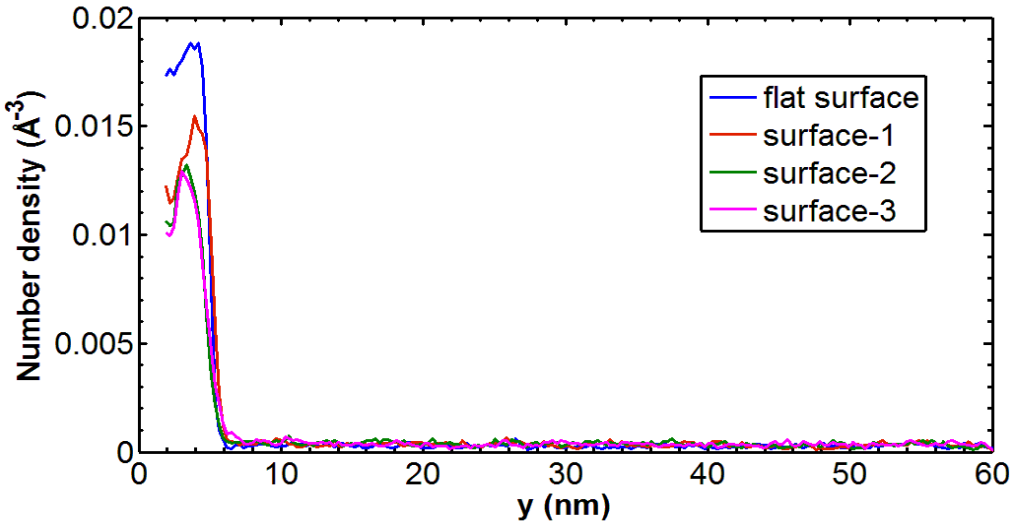

Fig. 4.48. Number density profile of argon at 3 ns for hydrophobic surface for low temperature case

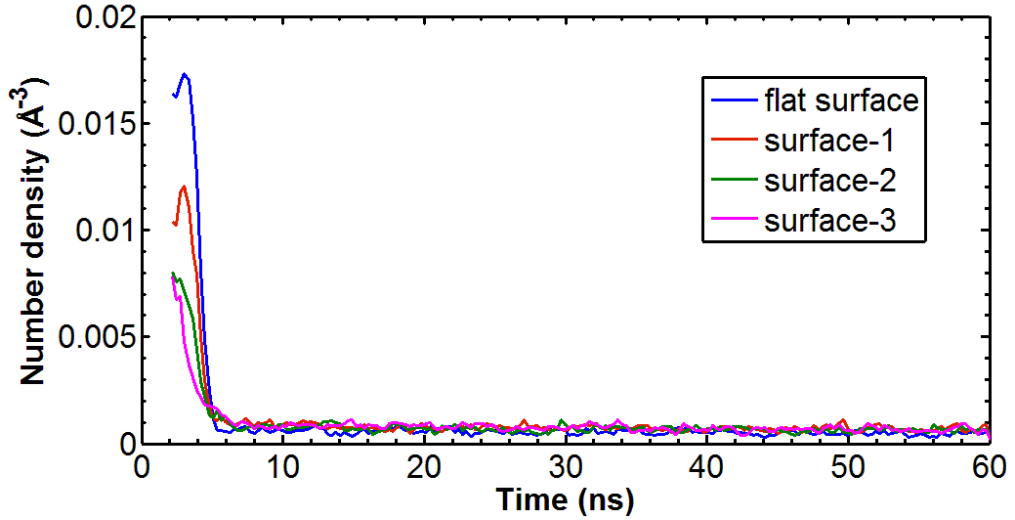

Fig. 4.49. Number density profile of argon at 5 ns for hydrophobic surface for low temperature case

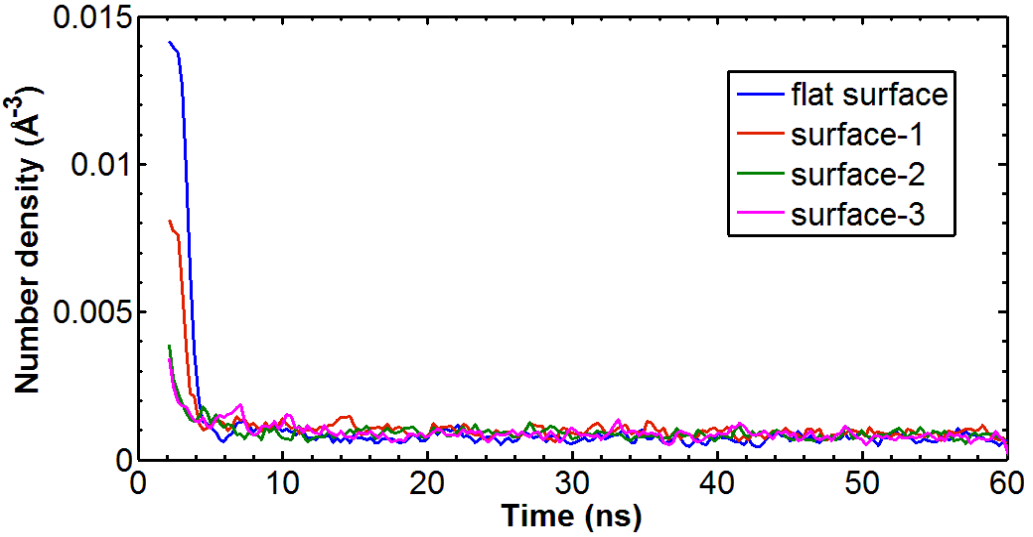

Fig. 4.50. Number density profile of argon at 7 ns for hydrophobic surface for low temperature case

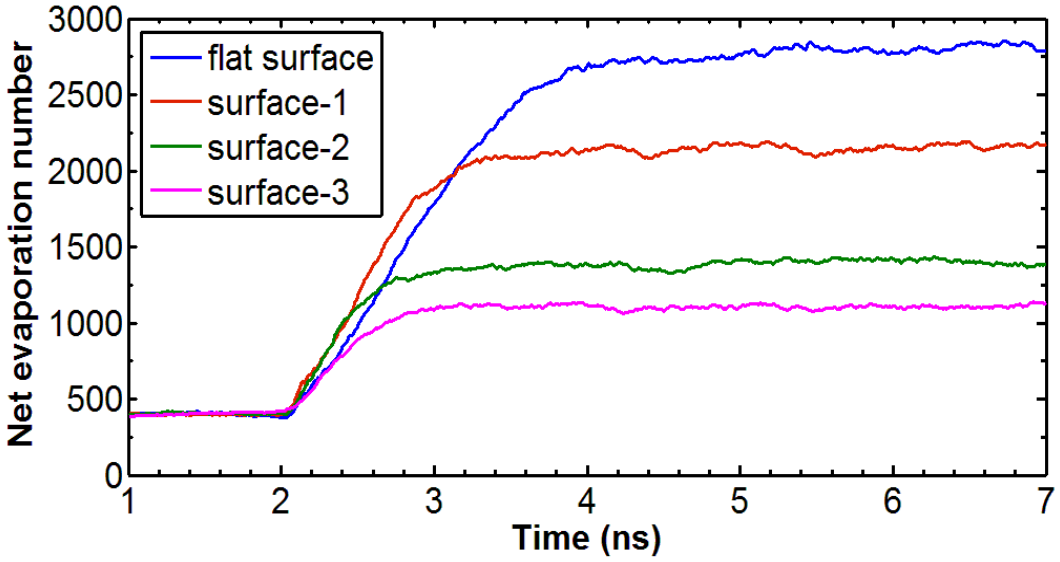

Fig. 4.51. Net evaporation number for hydrophilic surface for low temperature case

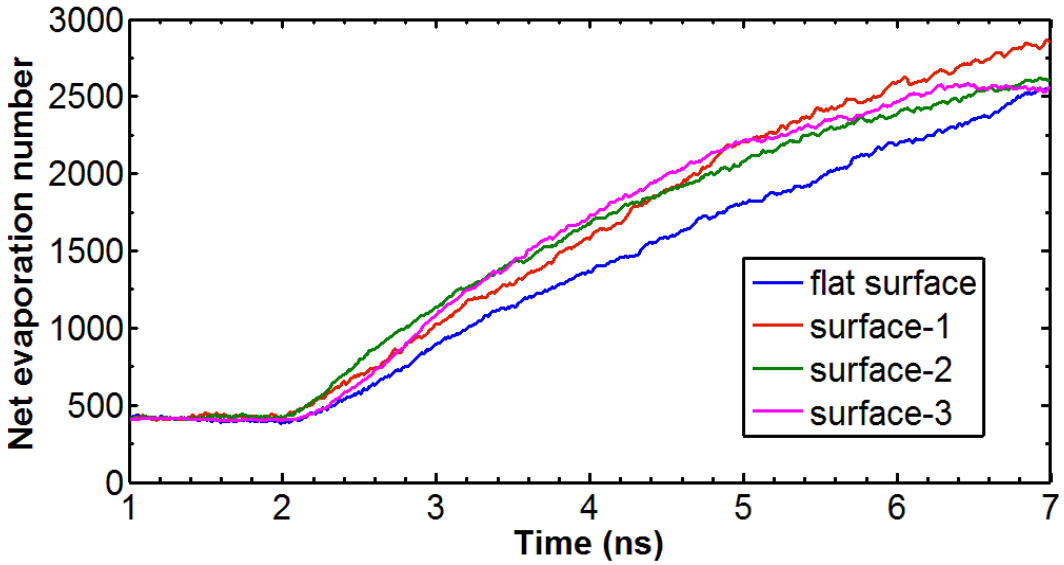

Fig. 4.52. Net evaporation number for hydrophobic surface for low temperature case

Figure 4.51 and 4.52 shows the net evaporation number in case hydrophilic and hydrophobic surface respectively. The increase of number of vapor atoms provides useful information about the rate of evaporation and non-evaporating layer. The rate of change of net evaporation number increases with the height of the nanostructures in case of both hydrophilic and hydrophobic surface. For hydrophilic case, the net evaporation number increases quite rapidly after the equilibrium period and reaches to constant value after some time, which suggests that there is no movement of argon atoms from the liquid layer to vapor region. As sown in Fig. 4.51, the value of net evaporation number after evaporation decreases with the height of nanostructure. Initially, the number of argon atoms in liquid layers was

different for different surface. But, the nanostructured surface-2 and surface-3 had same number of argon atoms in

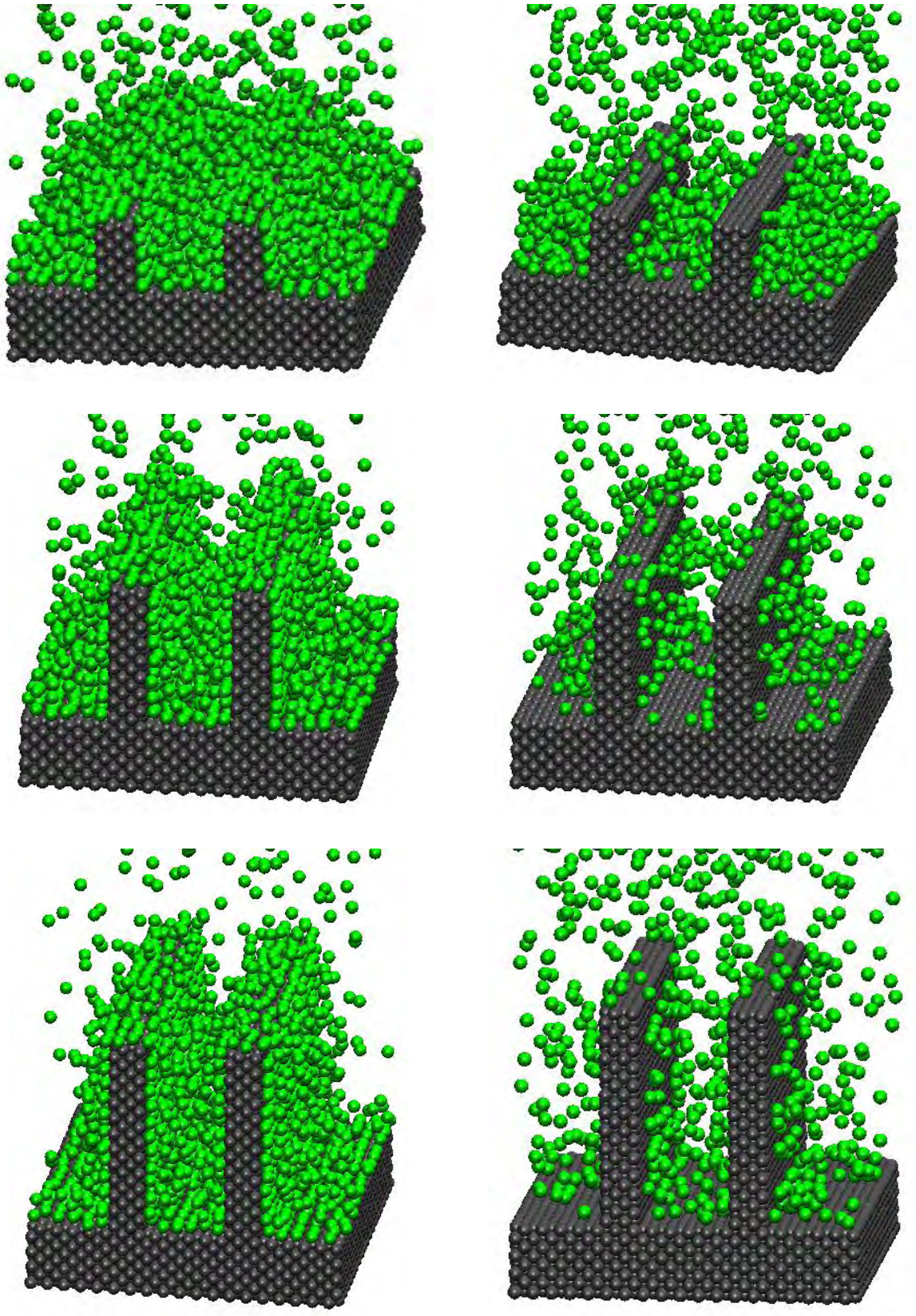

Fig. 4.53. Non-evaporating layer in case of hydrophilic (left column) and hydrophobic (right

column) surface, for (a) surface-1(row-1), (b) surface-2 (row-2) and (c) surface-3 (row-3) for low temperature case.

liquid layers initially. But after evaporation, from Fig. 4.51 it can be observed that, the value of net evaporation number is far less in case of nanostructured surface-3. With the increase of height of the nanostructure, the number of argon atoms in the non-evaporating layer increases. Therefore, a decrease in the net evaporation number has been found. Figure 4.53 shows the existence of non-evaporating layer in case hydrophilic surface and for 4.5 nm nanostructure highest number of argon atoms are present in the non-evaporating layer.

For hydrophobic case, as shown in Fig. 4.52 the net evaporation number increases almost linearly for all the cases. Because of low solid-liquid interaction potential in this case the argon atoms do not stay around the solid surface as shown in Fig. 4.53. So, the non-evaporating layer is not observed in case of hydrophobic surface.

Figures 4.54 and 4.55 show the heat flux profiles normal to the solid wall in case of hydrophilic and hydrophobic case respectively. The trend of the profiles are exactly similar to the previous study as discussed in the previous section. But addition of nanostructures increases the heat flux significantly and with the increase of the height of the nanostructures the heat flux increases. For hydrophilic case, the value of heat flux for nanostructured surface-3 (6×10^{-5} eV/Å^2.ps $\approx$ 960 MW/m^2) is almost 1.7 times the value heat flux observed in case of flat surface (3.5×10^{-5} eV/Å^2.ps $\approx$ 560 MW/m^2). On the other hand, for hydrophobic surface, the value of heat flux in case of nanostructured surface-3(4.5×10^{-5} eV/Å^2.ps $\approx$ 720 MW/m^2) is three times the value of heat flux found in case of flat surface (1.5×10^{-5} eV/Å^2.ps $\approx$ 240 MW/m^2). So, from the heat flux point of view, the increase of the height of the nanostructures has been more effective in case of hydrophobic surface. Another important point to note is that, the values of the heat flux for all cases are in order of the theoretical maximum value of heat flux, $q_{max,\max}$ as defined by Gambill and Lienhard [47].

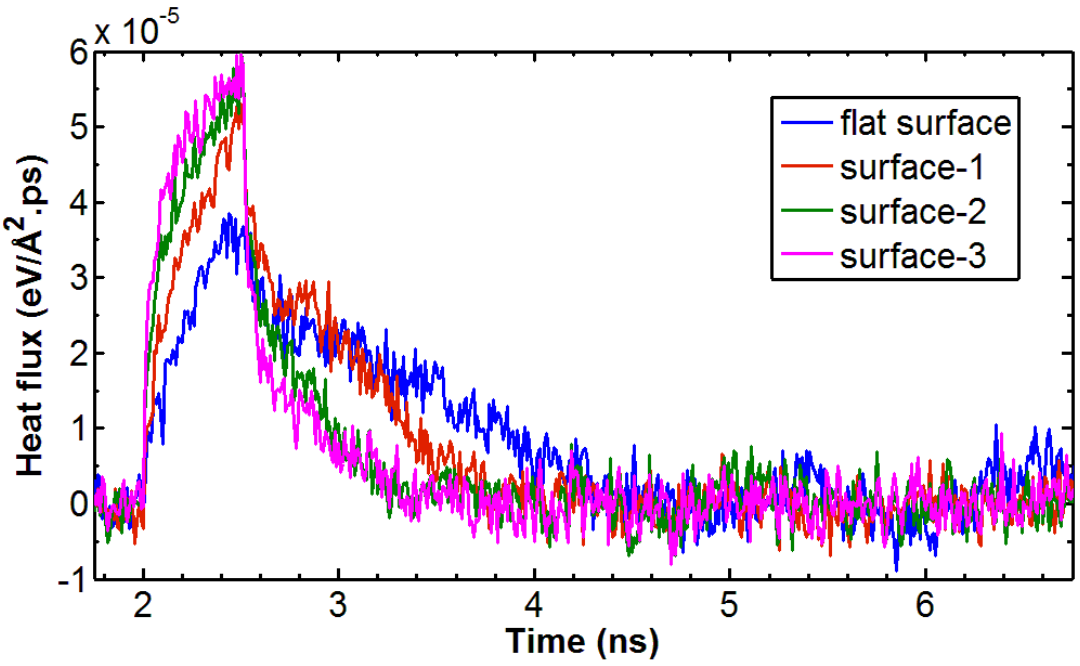

Fig. 4.54. Heat flux normal to solid wall for hydrophilic surface for low temperature case

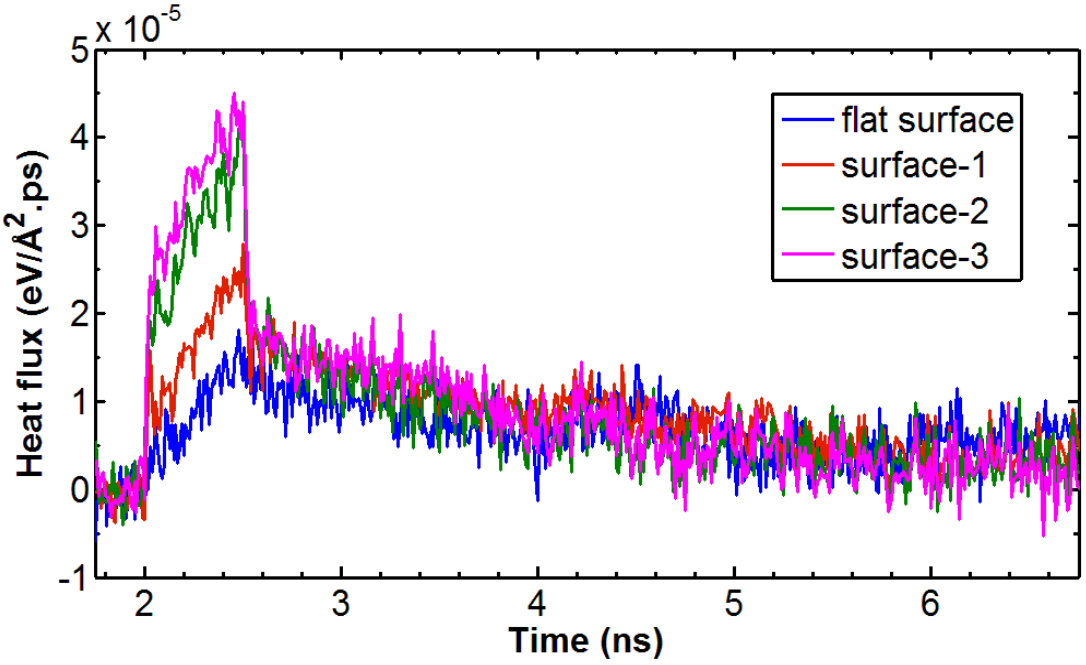

Fig. 4.55. Heat flux normal to solid wall for hydrophobic surface for low temperature case

4.2.2 High Temperature Case

When the temperature of the solid wall is suddenly increased from 90 K to 250 K, in case of hydrophilic surface liquid argon changes phase rapidly or explosive boiling occurs. Figures 4.56 and 4.57 show the snapshots of the simulation domain at different times for hydrophilic and hydrophobic cases respectively. For the flat hydrophilic surface as shown in Fig. 4.56, liquid layers start to leave the solid surface as a large liquid cluster as mentioned earlier at around 150 ps. For nanostructured surface-1 vaporization and separation of the liquid layers are observed in the same manner but the separation occurs a bit earlier (at around 100 ps). For nanostructured surface-2, due to the further increase of height of the nanostructure the solid-liquid interface area provides more heating of the liquid layer not only from the bottom surface but also from the sides of the nanostructures. Therefore, liquid escapes from the solid surface as individual or a well dispersed tiny cluster. In case of surface-3, liquid leaves the solid surface with more well dispersed tiny cluster and the phase transition takes place earlier than surface-2. But in case of hydrophobic surface as depicted in Fig. 4.57, as the time progresses liquid argon atoms gradually escapes from the top layer into the vapor region as individual atom and the number of atoms which reach the vapor region from liquid layer is quite few compared to hydrophilic surface even after 3 ns for flat surface. Because of reduced interaction between the solid and liquid atoms, in case of hydrophobic surface energy transfer is less and in case of nanostructured surface 2 and surface-3 a hint of liquid cluster is found.

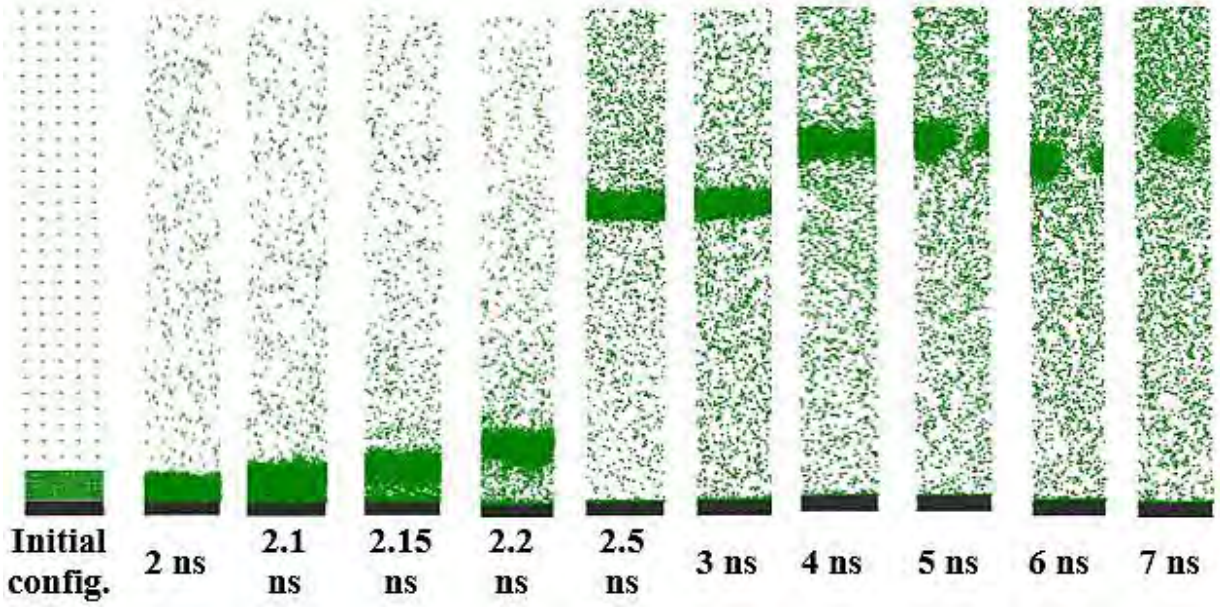
Initial config.
2 ns
2.1 ns
2.15 ns
2.2 ns
2.5 ns
3 ns
4 ns
5 ns
6 ns
7 ns

(a)

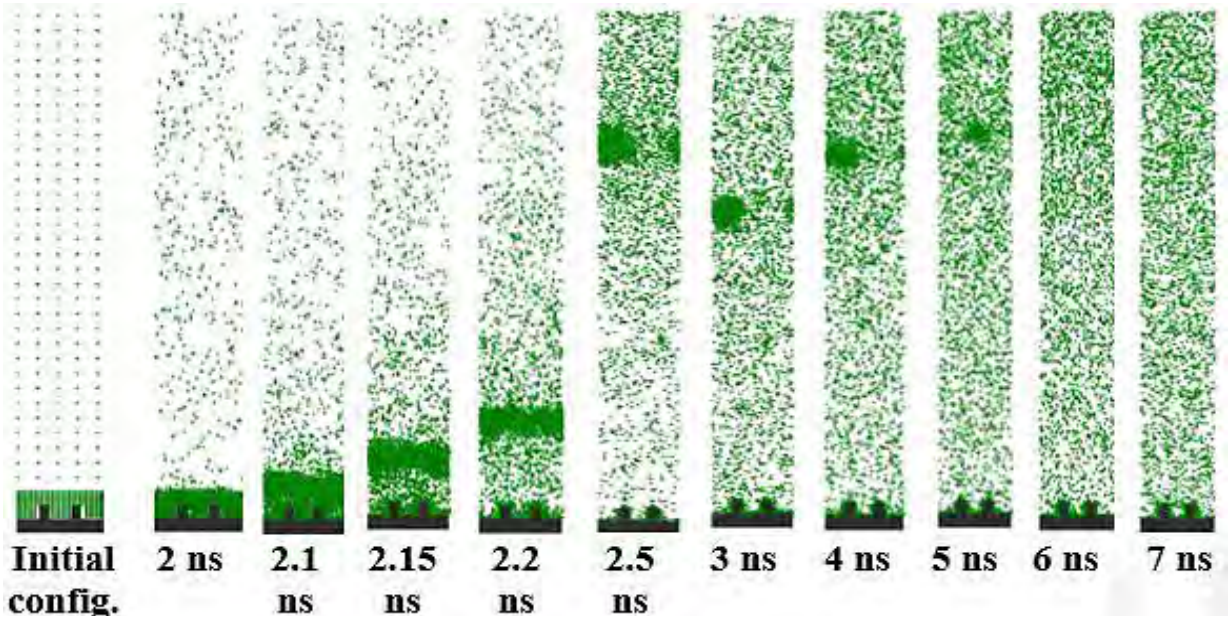
Initial config.
2 ns
2.1 ns
2.15 ns
2.2 ns
2.5 ns
3 ns
4 ns
5 ns
6 ns
7 ns

(b)

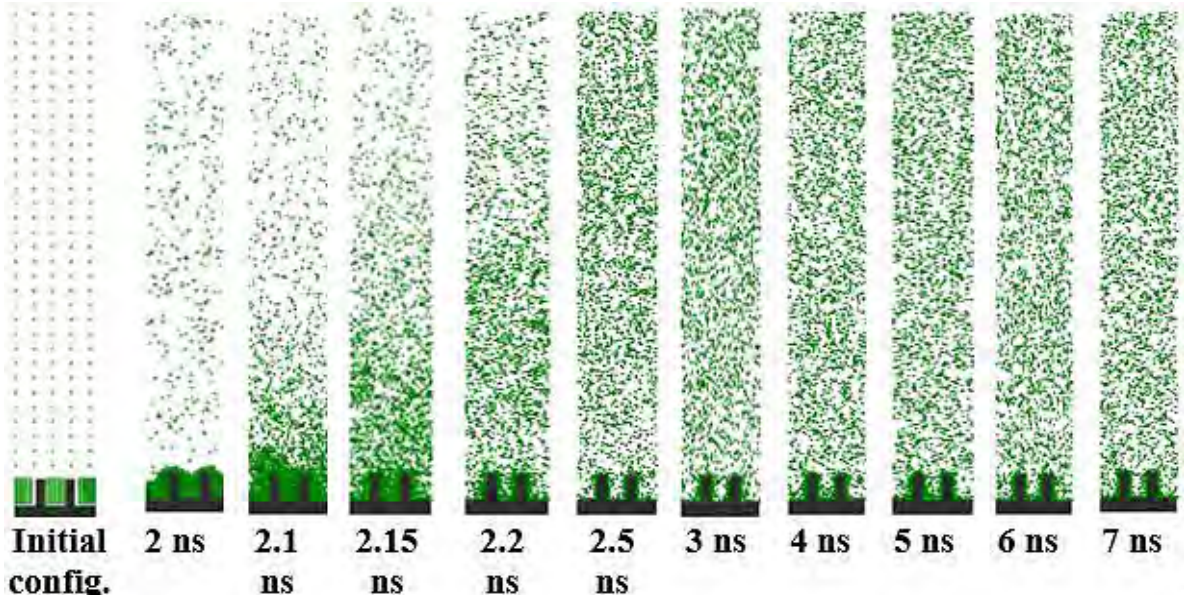

(c)

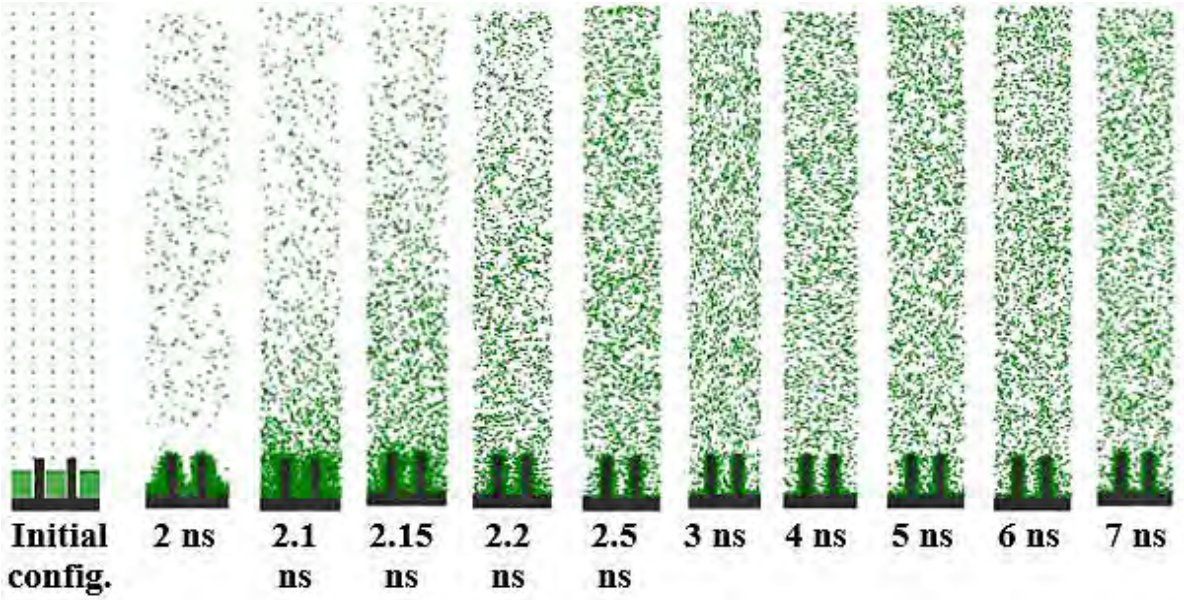

(d)

Fig. 4.56. Snapshots from the simulation domain for hydrophilic surface case, (a) flat surface, (b) surface-1, (c) surface-2, (d) surface-3

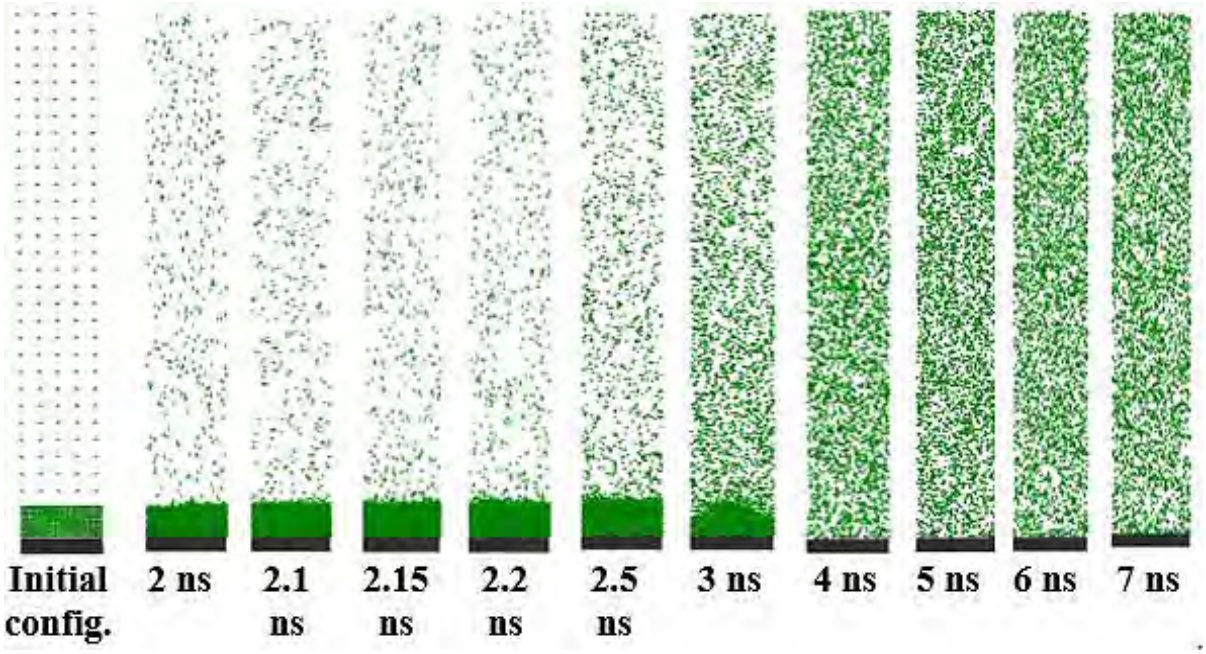
Initial config.
2 ns
2.1 ns
2.15 ns
2.2 ns
2.5 ns
3 ns
4 ns
5 ns
6 ns
7 ns

(a)

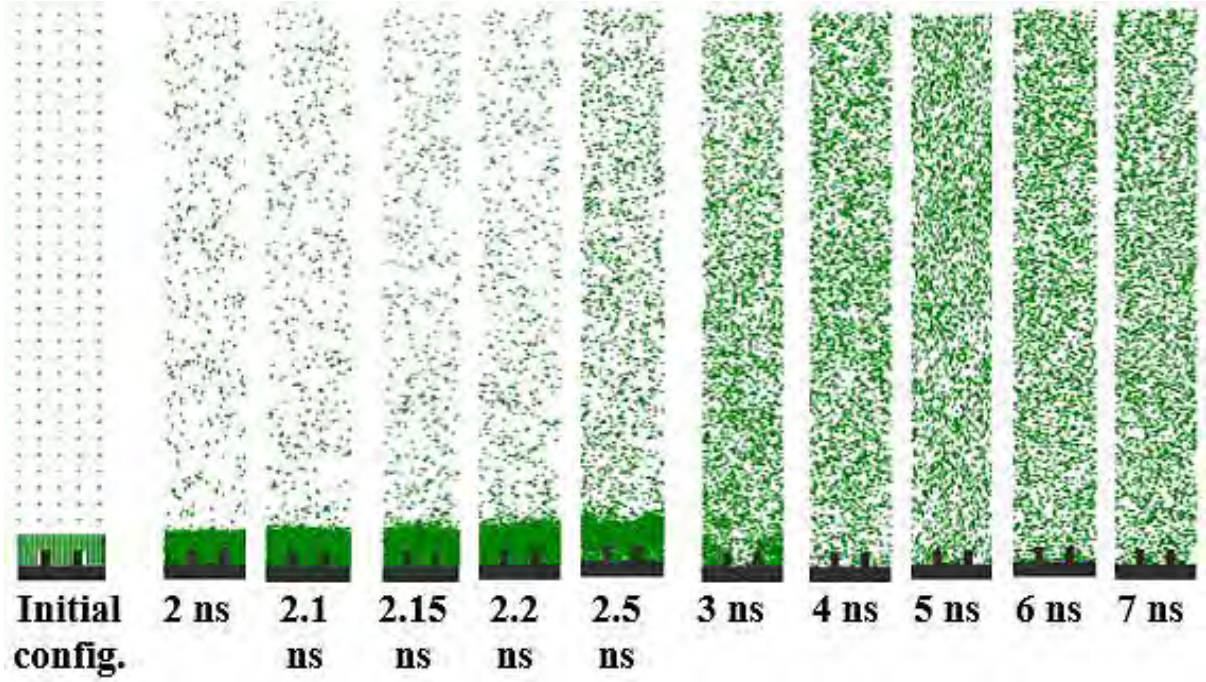
Initial config.
2 ns
2.1 ns
2.15 ns
2.2 ns
2.5 ns
3 ns
4 ns
5 ns
6 ns
7 ns

(b)

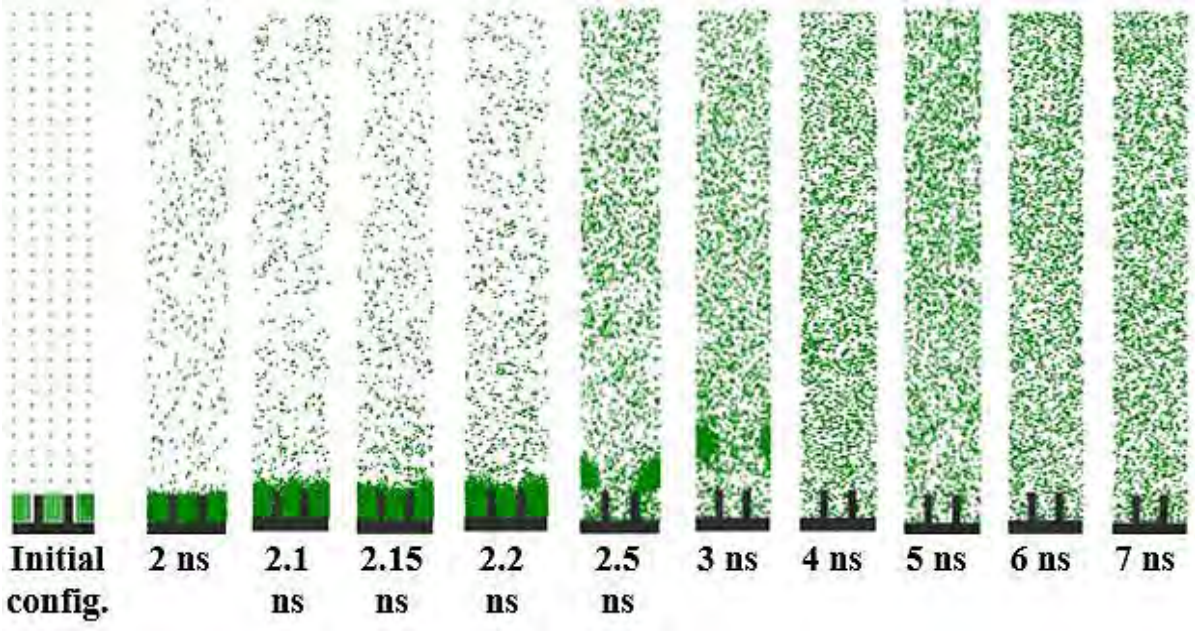

(c)

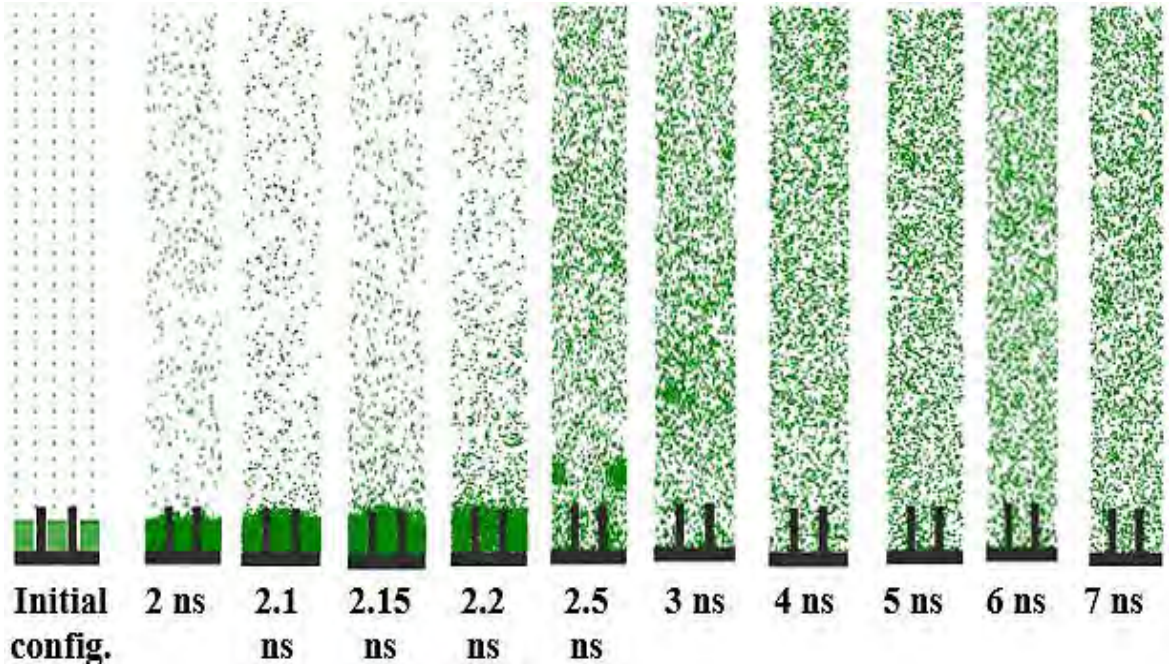

(d)

Fig. 4.57. Snapshots from the simulation domain for hydrophobic surface case, (a) flat surface, (b) surface-1, (c) surface-2, (d) surface-3

The temperature history of the system for hydrophilic surface case is shown in Fig. 4.58. Initially the temperature of the liquid increases very sharply, as liquid layer adjacent to the solid wall exceeds the critical temperature and instantly vaporizes while other layers above are still in the liquid phase. The pressure of this vaporized layer pushes the liquid above it and therefore, liquid layers separate from the solid wall. The energy flow from the solid wall to the liquid is hindered by this low density vapor region adjacent to the solid wall, therefore, the temperature of the liquid region falls temporarily. When nanostructures are added over the flat surface, the

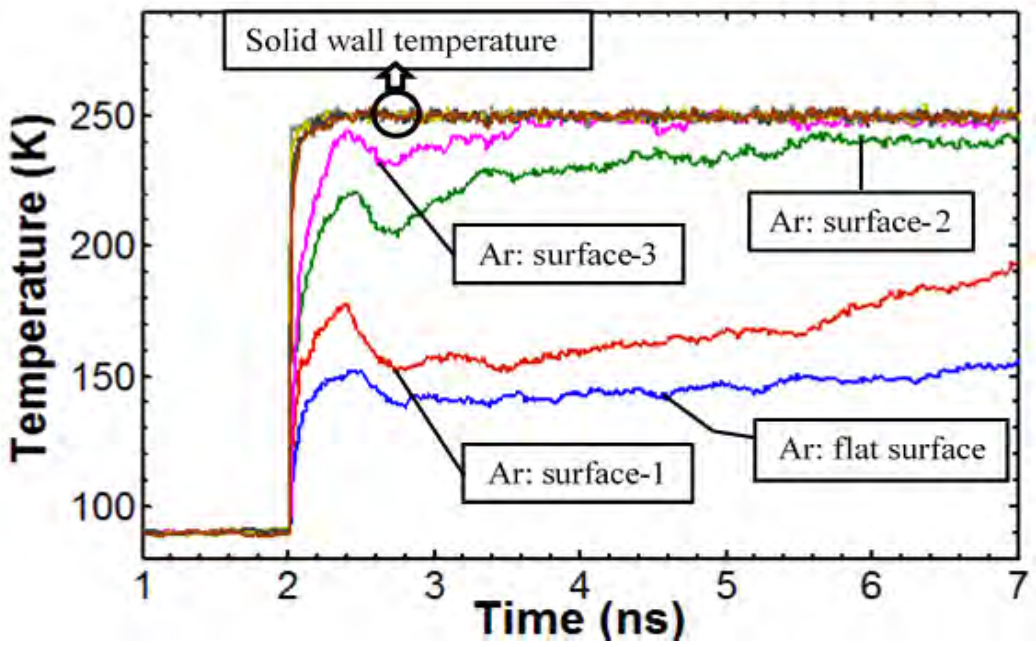

Fig. 4.58. Temperature history of argon (Ar) and solid wall for hydrophilic surface case

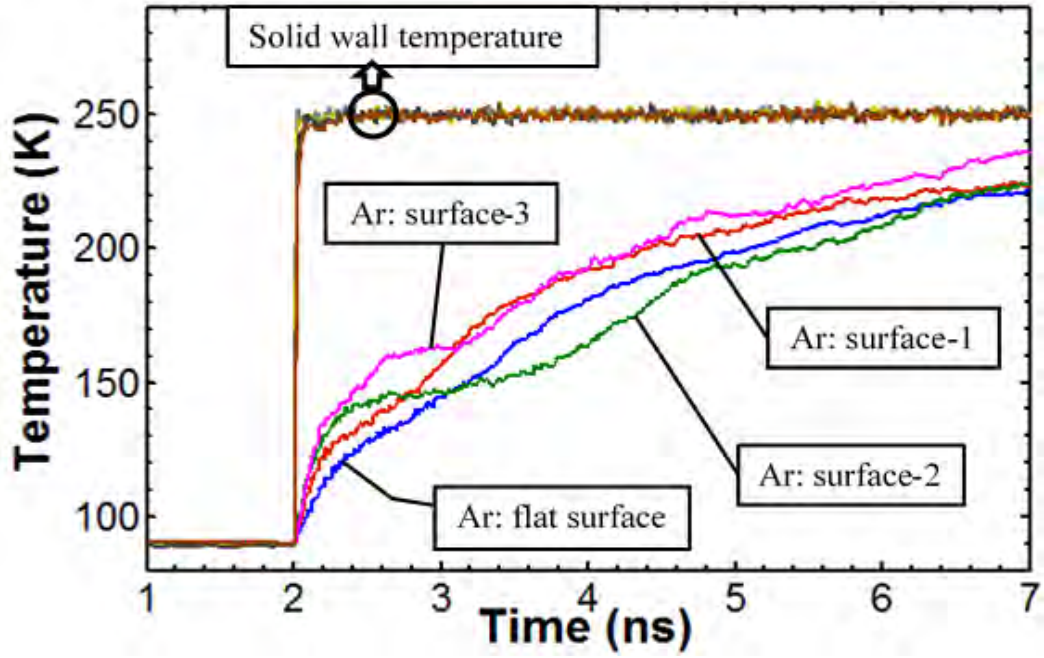

Fig. 4.59. Temperature history of argon (Ar) and solid wall for hydrophobic surface case

solid-liquid interfacial area increases and due to this larger interface area nanostructures lead to higher argon temperature as shown in Fig. 4.58. Unlike flat surface case, the liquid layers which were located above the vapor layer (which occurs adjacent to wall) get more heated from the nanostructures which increases the overall separation temperature. Another obvious fact is that, the separation temperature increases rapidly when the nanostructure's height is equal or more than the liquid layer's thickness. The temperature of argon starts increasing again after temporary drop as discussed earlier, and for the nanostructured surface-3, it reaches equilibrium at around 4.0 ns. For other surfaces, the argon temperature does not reach equilibrium within the simulation time.

Figure 4.59 shows the temperature history of the system for hydrophobic surface case. In case of hydrophobic surface, solid-liquid interaction is low; as a result energy transfer from the solid surface to liquid layer is much lower compared to hydrophilic surface. For flat hydrophilic surface, explosive boiling does not occur and therefore temperature of the liquid gradually increases with time like evaporation. Addition of nanostructures increases the energy transfer from solid surface to liquid argon which increases the bulk temperature of argon but the effect of nanostructures are not as significant as it was in case of hydrophilic surface. When the nanostructure's height is equal or more than the liquid layer's thickness in case of hydrophobic surface, the system showed a glimpse of explosive boiling; as a result the temperature of argon showed decreasing trend for some time for nanostructured surface-2 and surface-3 as shown in Fig. 4.59 which suggests that there must be vapor layer adjacent to solid wall and below the liquid layers. In case of hydrophobic surface, the temperature of argon does not reach equilibrium for any of the surfaces within the simulation time.

Figures 4.60 and 4.61 show the pressure history of the simulation domain for hydrophilic and hydrophobic surface respectively. The pressure increases with the increase of temperature as the volume of the system is constraint. For the hydrophilic case, the pressure profiles exactly follows the trend of the temperature of the simulation domain and for the cases with nanostructure, the pressure is higher than that of the case of flat surface. In case of hydrophobic surface pressure in case of flat surface and nanostructured surface-1 is higher than the nanostructured surface-2 and surface-3 because in case of latter two, small trace of explosive boiling are found and therefore pressure shows decreasing trend at that time just like the temperature profiles.

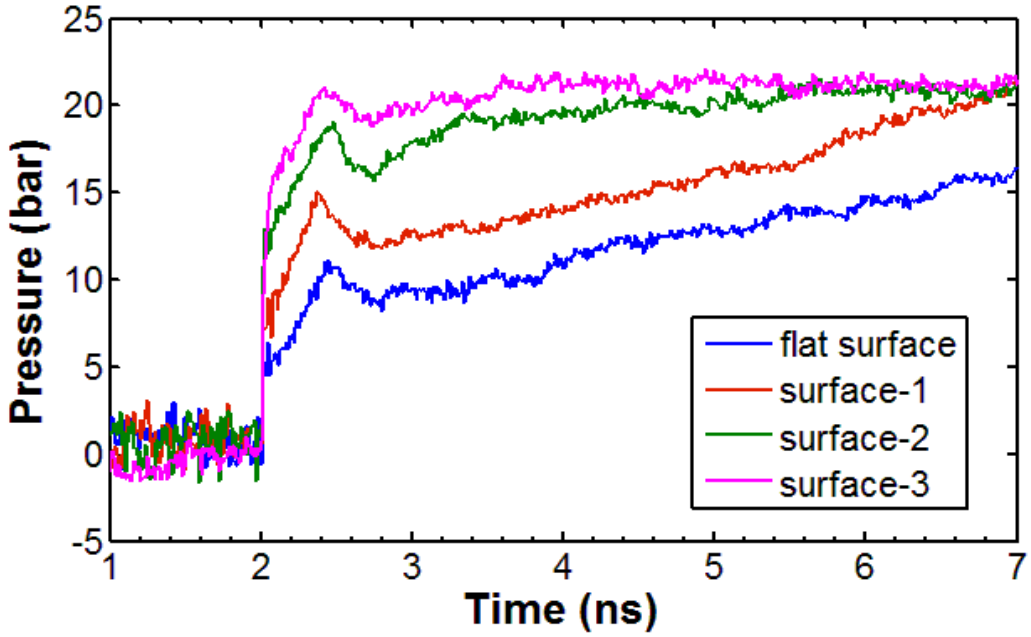

Fig. 4.60. Pressure history of the simulation domain for hydrophilic surface case

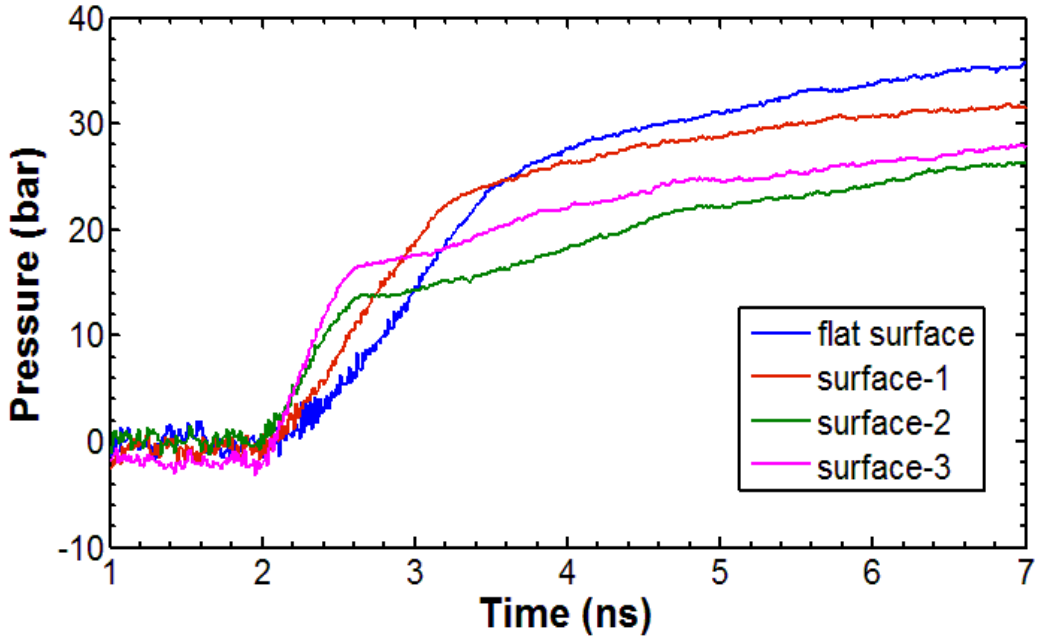

Fig. 4.61. Pressure history of the simulation domain for hydrophobic surface case

Figure 4.62 shows the spatial temperature distribution of argon atoms in case of flat hydrophilic surface at different time. Just at the end of the equilibrium period (t = 2 ns), the temperature of argon atoms is around 90 K. At 2.2 ns, temperature of argon atoms at a height of 10-15 nm is lower than the other regions. As mentioned in earlier discussion, at 2.2 ns liquid clusters move upward and reaches to a height of around 10 nm as depicted in the snapshots of Fig. 4.56(a) and number density profile of Fig. 4.65. In this 'liquid cluster'

region, the argon atoms are close to each other and their kinetic energy is lower than other regions, therefore, the temperature of argon atoms in this region is low. It should be noted that, the temperature of argon atoms in this region is below the critical temperature of argon, which is 150 K. From the thermodynamic point of view, the temperature of liquid phase should not exceed the critical temperature, therefore, the argon atoms in this region can be described as liquid clusters. At 2.5 ns similar characteristics are found, but liquid clusters in this case reaches at a height of around 35 nm. From the snapshots of Fig. 4.56(a), it can be observed that, from around 2.5 ns and onwards, argon atoms from the liquid clusters disperse to other regions and number of atoms in the clustered region decreases gradually as shown in number density profile of Fig. 4.65. Therefore, from 3 ns and onwards, the spatial temperature distribution has a decreasing trend; the kinetic energy of argon atoms close to solid surface is higher and decreases with the height of the simulation domain. But at the height of 35 nm and above, the liquid clusters are still visible as shown in Fig. 4.56(a), therefore, temperature at this region remains below the critical temperature (150 K) as shown in Figs. 4.62. Figure 4.63 shows the spatial temperature distribution of argon atoms at 3 ns for hydrophilic surface; the effect of nanostructure on the spatial temperature can be closely studied from this figure. As the height of the nanostructure is increased the temperature of argon atoms in all region increases. For nanostructured surface-2 and surface-3, at 3 ns the argon atoms in the simulation domain remains as individual atoms as depicted in the snapshots of Fig. 4.56(c) and (d) and number density profile of Fig. 4.66. The energy transfer rate significantly increases with the increase of height of the nanostructure, therefore, argon atoms gain higher kinetic energy which results higher temperature as shown in Fig. 4.63. From the spatial temperature distribution of Fig. 4.63 and number density profile of Fig. 4.66, it can be said that, there is no trace of liquid clusters for nanostructured surface-2 and surface-3 at 3 ns as temperature of the argon atoms is well above the critical temperature.

For the hydrophobic surface, as shown in Fig. 4.64, increase of nanostructure height enhances energy transfer rate and the temperature of argon atoms increases. Because of higher energy transfer rate, for nanostructured surface-2 and surface-3, a trace of explosive boiling was found as shown in Fig. 4.57(c) and (d) and number density profile of Fig. 4.67 at 3 ns. Therefore, for nanostructured surface-2 and surface-3, there is a drop of temperature (below the critical temperature of 150 K) in the corresponding region where the argon atoms remains close to each other or as ‘liquid clusters’ as shown in Fig. 4.67.

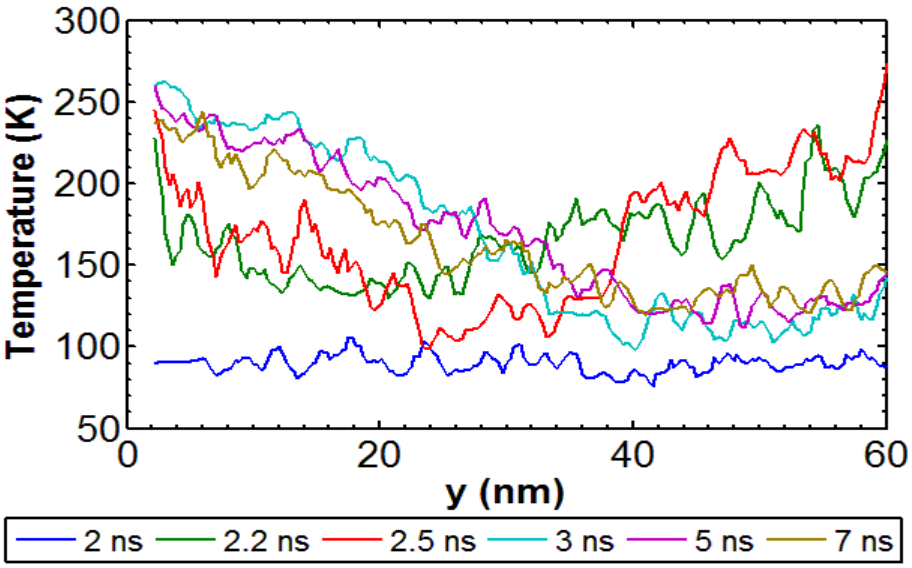

Fig. 4.62. Spatial temperature distribution of argon in case of flat hydrophilic surface at different time

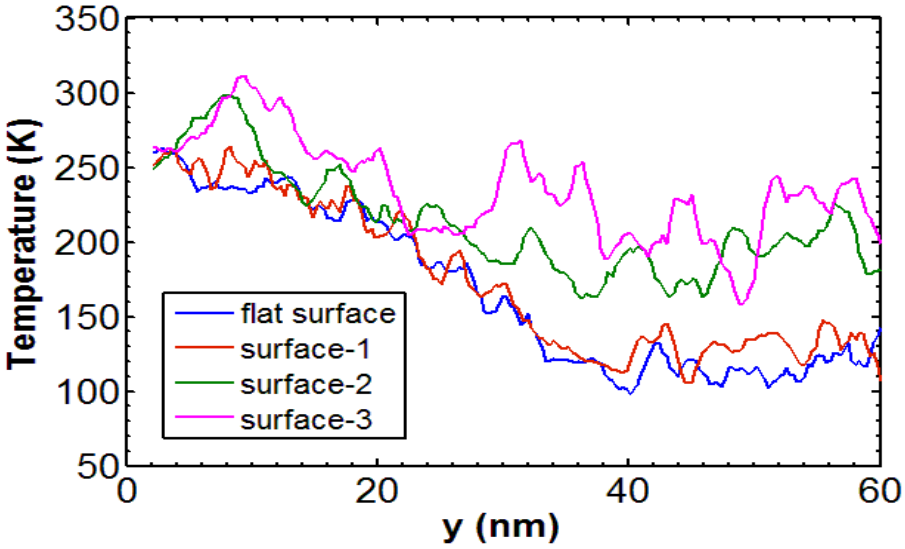

Fig. 4.63. Spatial temperature distribution of argon at 3 ns for hydrophilic surface

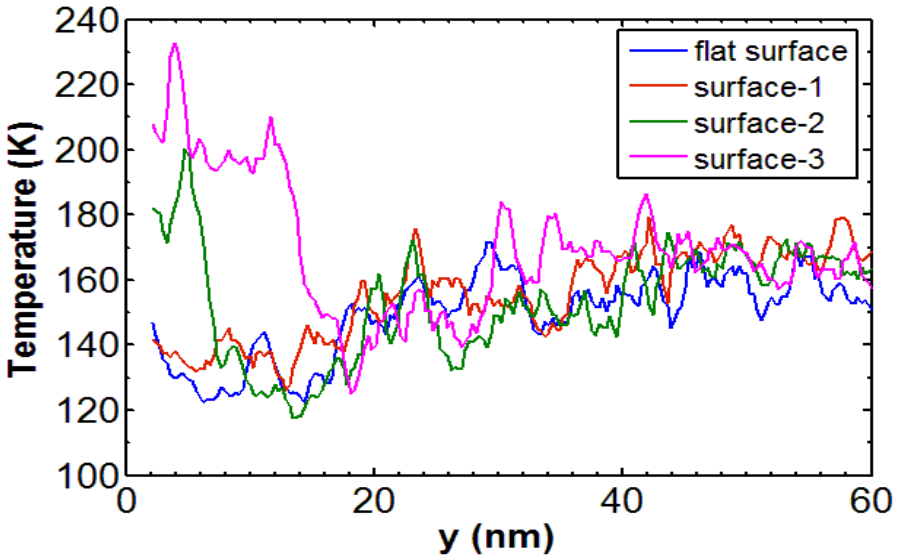

Fig. 4.64. Spatial temperature distribution of argon at 3 ns for hydrophobic surfaces

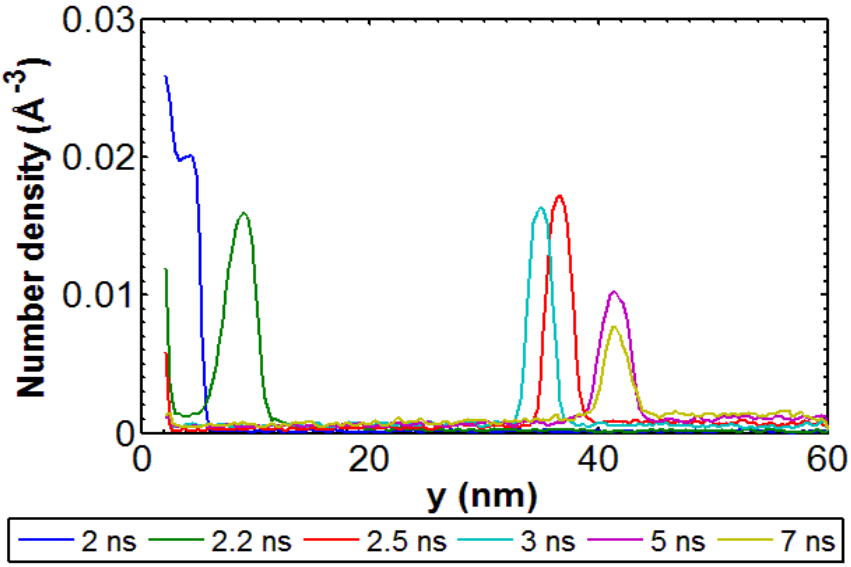

Fig. 4.65. Number density profile of argon in case of flat hydrophilic surface at different times.

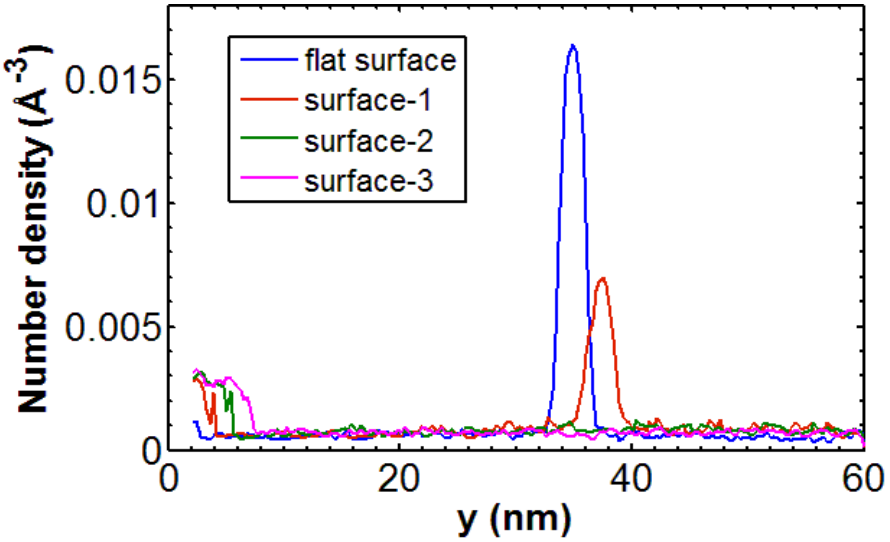

Fig. 4.66. Number density profile of argon at 3 ns for hydrophilic surfaces.

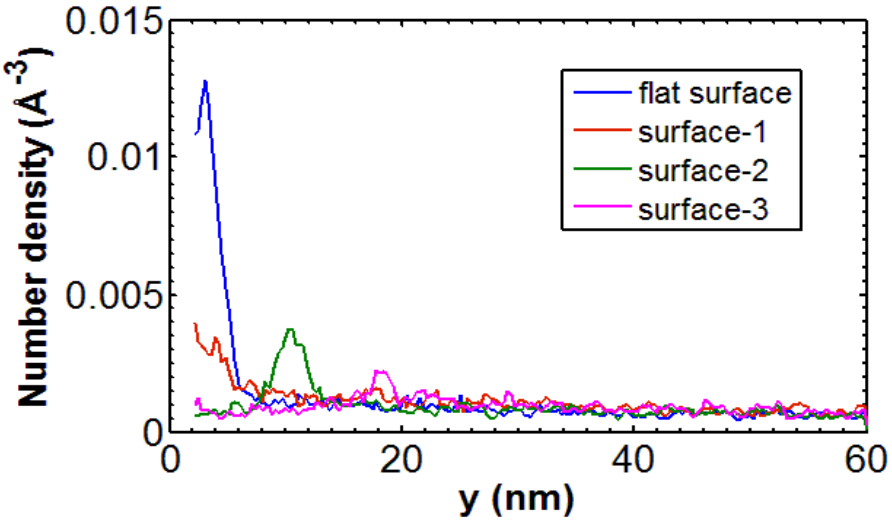

Fig. 4.67. Number density profile of argon at 3 ns for hydrophobic surfaces.

In this study, heat flux normal to the solid wall is calculated from the per atom potential energy, the per atom kinetic energy and per atom stress tensor as discussed earlier. Figures 4.68 and 4.69 depict the heat flux normal to the solid wall (xz plane) for hydrophilic and hydrophobic cases respectively. For all the cases the trend of the profiles are same. Just after the jump of temperature from 90 K to 250 K, a high heat flux is added within a short time. After this stage the heat flux drops sharply and oscillates around zero value. The profiles of the heat flux are in good agreement with previous study conducted by Yamamoto and Matsumoto [38]. As expected the hydrophilic case has larger values of heat flux compared to hydrophobic surface. With the increase of nanostructure height, the solid-liquid interface area increases, thus, heat flux normal to the solid surface increases and is maximum for nanostructured surface-3. In case of flat hydrophilic surface, the maximum value of the heat flux is about 7×10^{-5} eV/Å^2.ps or, 1100 MW/m^2 which is slightly higher than the magnitude of theoretical maximum value of heat flux, $q_{max,max} \approx 800$ MW/m^2 as defined by Gambill and Lienhard [47]. The maximum value of heat flux is obtained in case of hydrophilic nanostructured surface-3 which is about 17×10^{-5} eV/Å^2.ps or, 2724 MW/m^2, about 2.5 times the value found in case of flat surface. For hydrophobic case, in case of flat surface and nanostructured surface-1 heat energy is transferred for longer period time as depicted in Fig. 4.69. But in case of nanostructured surface-2 and surface-3 heat flux profiles drop sharply just like hydrophilic surface cases again suggesting that there is a hint of explosive boiling in these cases. The value of heat flux in case hydrophobic nanostructured surface-3(12×10^{-5} eV/Å^2.ps $\approx$ 1920 MW/m^2) is about 4 times the value of heat flux in case of flat hydrophobic surface(4×10^{-5} eV/Å^2.ps $\approx$ 640 MW/m^2).

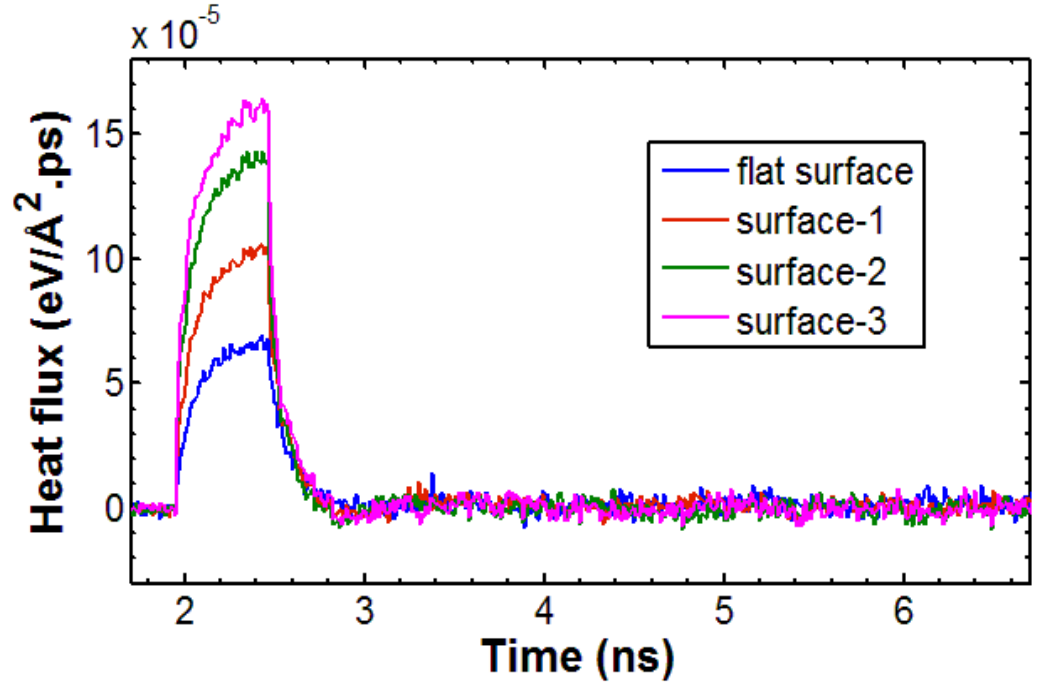

Fig. 4.68. Heat flux normal to solid wall for hydrophilic surface case

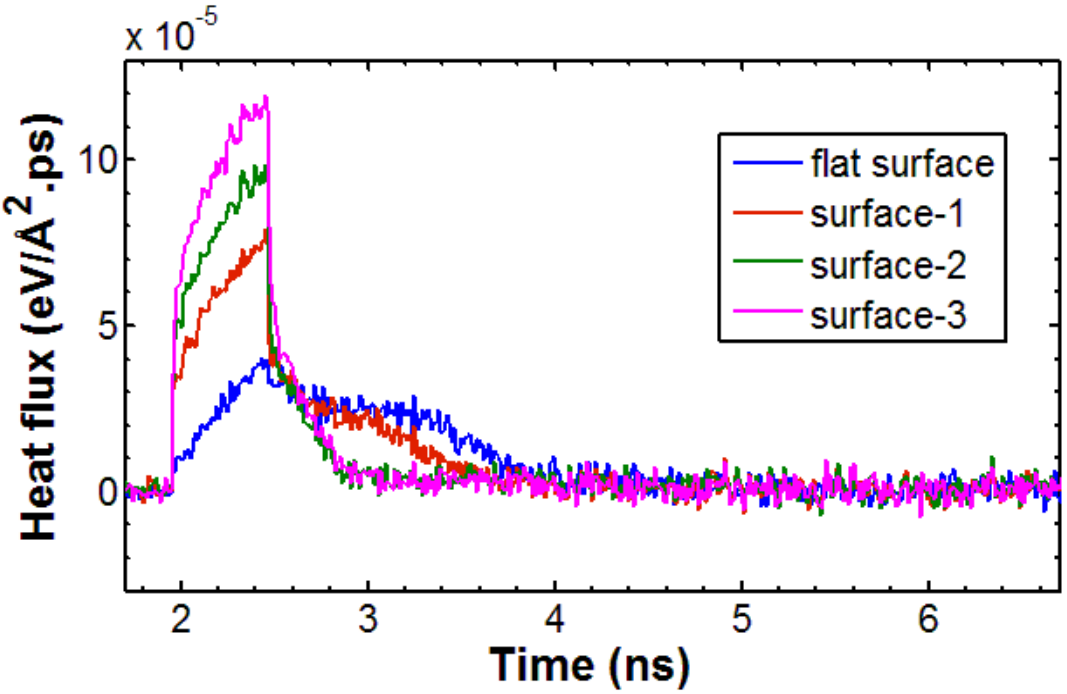

Fig. 4.69. Heat flux normal to solid wall for hydrophobic surface case

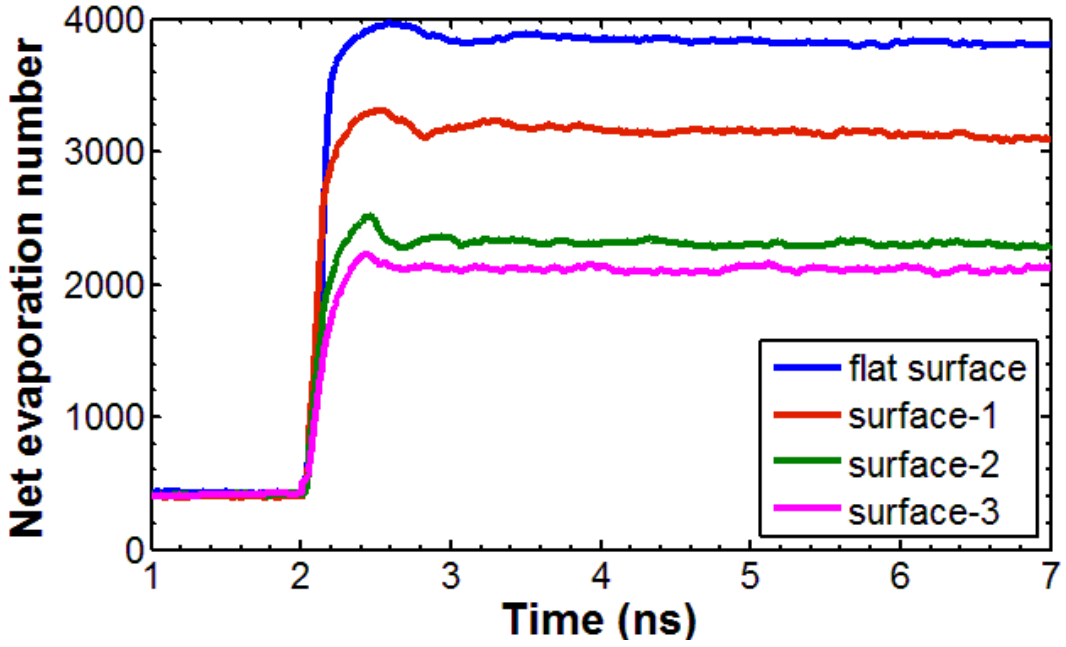

Fig. 4.70. Net evaporation number for hydrophilic surface case

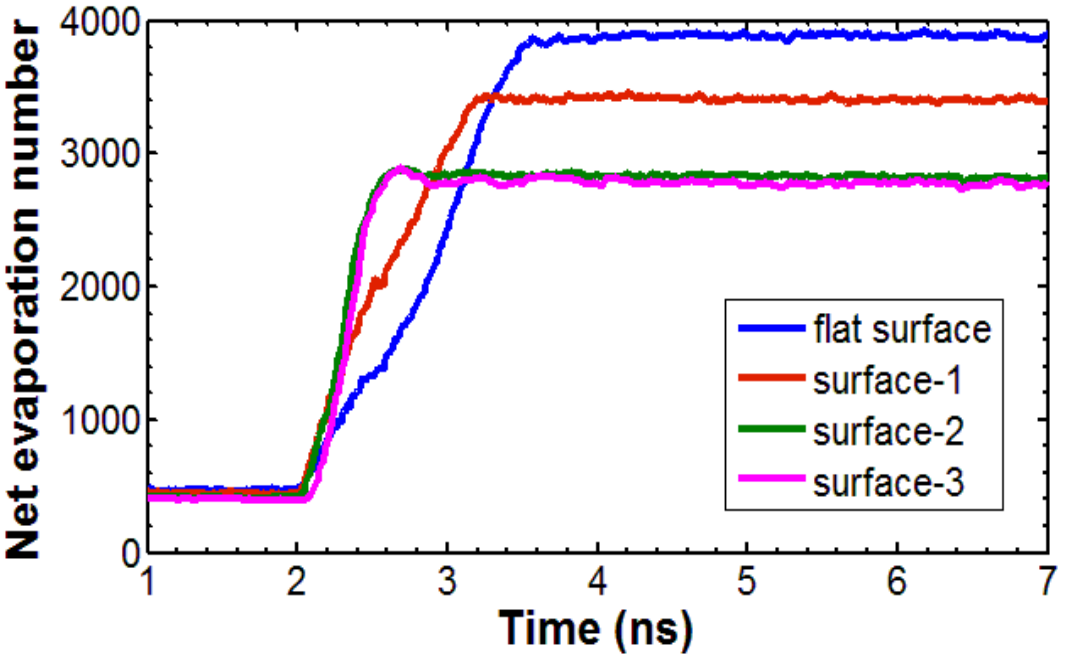

Fig. 4.71. Net evaporation number for hydrophobic surface case

Figures 4.70 and 4.71 show the net evaporation number in case of hydrophilic and hydrophobic surface respectively. The net evaporation number was calculated by counting the change of argon atoms in the vapor region. The evaporation numbers for all the surfaces in both cases remain constant up to 2 ns (during equilibrium period). For hydrophilic case as depicted in Fig. 4.70, for all surfaces under consideration, the net evaporation number increases almost instantaneously as soon as the wall temperature is increased from 90 K to

250 K. In all these cases, around the time t = 2.6 ns, the number of atoms in vapor region does not change much with time which indicates that no significant liquid atoms maintains direct contact with the wall i.e., the evaporation rate drastically drops after this. Note that, the total number of liquid atoms in the simulation domain was the maximum for the flat surface case and while nanostructures were incorporated over the flat surface, the simulation domain contains lesser number of liquid argon atoms. Therefore, for the case of surface- 1, the number of liquid argon atom was smaller than the flat surface case. However, in case of nanostructured surface- 2 and surface- 3, the total number of liquid atoms was same. This variation in the number of liquid argon atom has been found to have significant effect on the net evaporation number as shown in the Fig. 4.70. The number of atoms in vapor region for surface-3 is less than surface-2 after explosive boiling though they had same number of liquid atoms initially. This is because of the fact that, the height of the nanostructure in surface-3 is more than surface-2 which results in stronger solid-liquid interaction. It has been reported that, as hydrophilic surface has higher solid-liquid interaction potential, some argon atoms remains attached with the solid surface and form an ultra-thin layer of argon atoms termed as the non-evaporating layer [32, 40-42]. Similar phenomena have been found in the present study as depicted in Fig. 4.72. With the increase of height of the nanostructure, the number of argon atoms in the non-evaporating layer increases. Therefore, a decrease in the net evaporation number has been found as the surface pattern is changed from flat surface to nanostructured surface-4. In case of hydrophobic surface as shown in Fig. 4.71, the increase of net evaporation number with time after the equilibration period shows nearly linear behavior for flat surface and nanostructured surface-1 which suggests that the evaporation rate is nearly constant after the equilibration period until all liquid atoms is completely vaporized. But in case of nanostructured surface-2 and surface-3, net evaporation number increases sharply after the equilibration period just like hydrophilic surface as there is a trace of explosive boiling as shown in Fig. 4.57. It is noteworthy that, the net evaporation number in case of nanostructured surface-1, 2 and 3 is greater in hydrophobic case than the hydrophilic case. In case of hydrophobic surface, no non-evaporating layer is formed as shown in Fig. 4.72, because of less solid-liquid interaction. Therefore, number of atoms in the vapor region was obtained higher in case of hydrophobic surfaces.

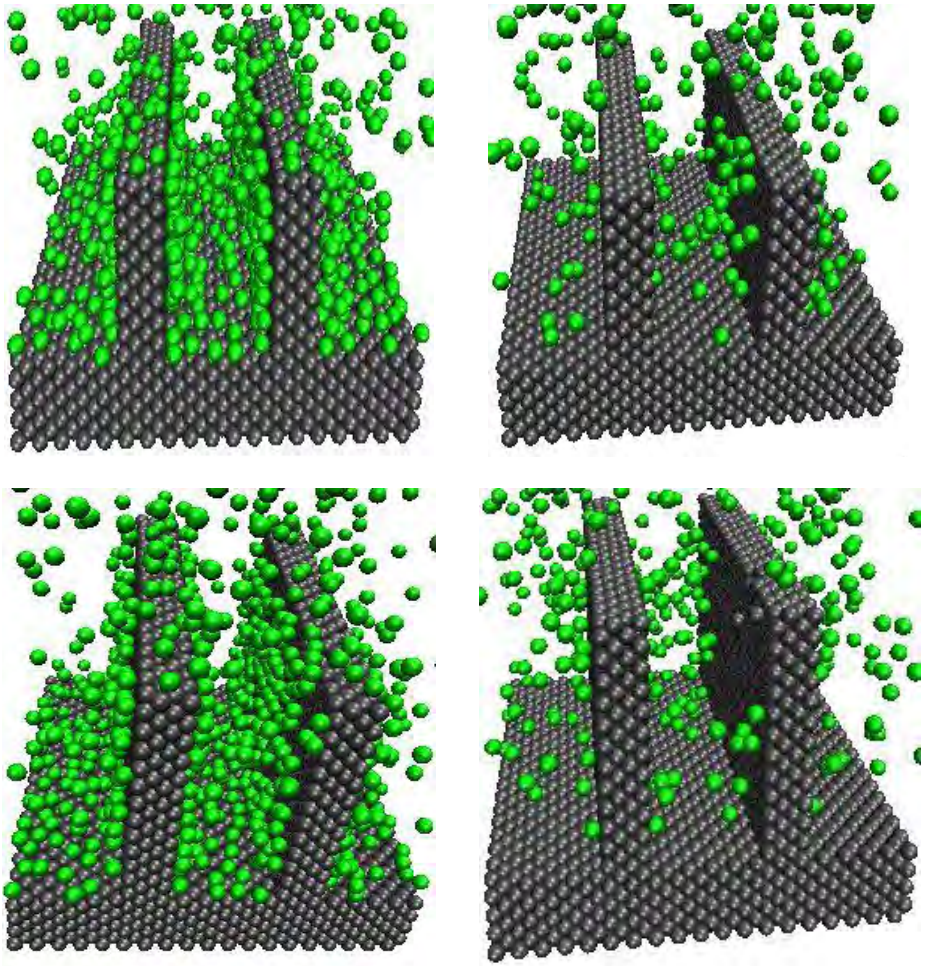

Fig. 4.72. Non-evaporating layer in case of hydrophilic (left column) and hydrophobic (right column) surface, for (a) surface-2 (row-1), (b) surface-3 (row-2).

4.2.3 Summary

Evaporation and explosive boiling phenomena for a thin liquid argon layer over nanostructured platinum surface has been closely studied by performing non equilibrium molecular dynamics (NEMD) simulations for different surface wetting conditions, namely hydrophilic and hydrophobic cases.

The effect of the height of nanostructure is more significant in case of hydrophilic surface and increase of nanostructure height enhances the evaporation and explosive boiling phenomena. On the other hand, in case of hydrophobic surface, increase of nanostructure height had much lesser effect on boiling phenomena.

For high temperature case, explosive boiling was observed in case hydrophilic surface and liquid cluster suddenly got separated from the solid surface and moved upward. The height of

the nanostructure strongly has strong effect on the size of the liquid cluster. The liquid atoms moved as individual molecules or a very tiny cluster instead of a large cluster of liquid when the nanostructures height was equal or more than the liquid film thickness. The separation temperature is also found to be strongly dependent on the height of the nanostructures and increased sharply when the nanostructures height was equal or more than the liquid film thickness.

For both low and high temperature case, non-evaporating layer was found in case of hydrophilic surface having nanostructures. But, for hydrophobic surface no such layer was found.

The heat flux profiles also confirmed that the energy transfer rate is much higher in case of hydrophilic surface for both low and high temperature case. Heat flux increased significantly with the increase of the height of the nanostructure.

CHAPTER 5

CONCLUSION AND FUTURE WORK

5.1 Conclusion

In this thesis, non-equilibrium molecular dynamics simulation on evaporation and explosive boiling of thin liquid film is carried out to investigate the effect of surface material and nanostructures with different surface wetting conditions. Argon was used as the working fluid while three solid materials i.e., platinum, silver and aluminum were selected as the wall material. The nanostructures having a shape of rectangular block with different heights (1.5 nm, 3.0 nm and 4.5 nm) were used in the simulation. Based on the surface wettability, two cases were considered (hydrophilic and hydrophobic). Two different degrees of superheat was selected: a moderately high temperature of 130 K for evaporation and much higher temperature of 250 K for explosive boiling. The results of the simulation were evaluated on the basis of net evaporation number, number density, argon and solid wall temperature histories, pressure history, profile of wall heat flux and trajectories of atoms for different cases. The main observations from the simulations of this study can be concluded as below:

1. The results of this study suggests that the surface wettability has very strong effect on both evaporation and explosive boiling of argon. For both evaporation and explosive boiling, the increase of surface wettability provided more solid-liquid interaction, which greatly affected the boiling phenomena. Therefore, the trajectories of atoms and other profiles including the heat flux suggested that, the hydrophilic surface provides more favorable condition for boiling than hydrophobic surface.
2. The effect of different wall material on boiling phenomena is less significant compared to the effect of surface wettability. The number density, temperature, net evaporation number and heat flux profiles show that among the three materials which are considered in this study, aluminum is less favorable for boiling phenomena than the other two. Silver and platinum show almost similar characteristics.
3. The size of the nanostructures has a significant effect on both evaporation and explosive boiling, and it has been observed that, increase of the height of the nanostructure significantly affect the trajectory or physics of the argon atoms. The

size of the liquid cluster depends on the size of the nanostructure in case of explosive boiling.

4. For high temperature case, explosive boiling is observed in case of hydrophilic surface and liquid layers move away from the solid surface as liquid cluster. Only trace of explosive is observed in case of hydrophobic surface when the height of the nanostructures were equal (3.0 nm) and greater (4.5 nm) than the liquid layers.
5. The increase of height of the nanostructure provides more solid-liquid contact surface, thus rate of energy transfer from solid surface to liquid increases significantly and affects the boiling phenomena which is confirmed by the heat flux profiles.
6. For low temperature case, the value of heat flux in case of nanostructured hydrophilic surface-3 (4.5 nm) is almost 1.7 times (≈960 MW/m^2) the value of heat flux in case of flat hydrophilic surface (≈560 MW/m^2). For hydrophobic surface, the value of the heat flux is three times higher in case of nanostructured surface-3 (≈720 MW/m^2) than the flat surface (≈240 MW/m^2). For all the cases, the values of the heat flux are in same order of the theoretical maximum value of heat flux as defined by Gambill and Lienhard [47].
7. For high temperature case, in case of hydrophilic surface, the value of the heat flux is 2.5 times higher in case of nanostructured surface-3 (≈2724 MW/m^2) than the flat surface (≈1120 MW/m^2). For hydrophobic surface, it is about four times (≈1920 MW/m^2) than the value of heat flux in case of flat surface (≈672 MW/m^2). Thus, from heat flux point of view, nanostructures proved to be more effective in case of hydrophobic surface. For high temperature case, the values of the heat flux are one order greater than the theoretical maximum value of heat flux as defined by Gambill and Lienhard [47].
8. For certain cases, in a specific time after beginning of boiling, the evaporation on the hot wall stops and a non-evaporating layer is formed on the surface. For the cases with nanostructures, the number of non-evaporative atoms is higher than the one for flat case; with the increasing height of nanostructure, the number of atoms in non-evaporating layer increases.

5.2 Future Work

In the present study, argon was used as the working fluid. In future, the simulations of this study could be extended by considering more complicated working fluid such as water. The investigation of the temperature and pressure histories, number density, net evaporation number, heat flux and etc. for evaporation and explosive boiling of water in presence of nanostructures would certainly provide more insight about the boiling phenomena.

The nanostructures which were considered in this study had rectangular shape. Different shape of nanostructure could be considered in future. The shape and size of the nanostructures should be realistic so that they could be manufactured and applied in practical situations. Some very recent studies considered nano-recess instead of nanostructures to explore its effect on boiling phenomena. So, nano-recess may become a common feature in upcoming NEMD studies on boiling phenomena.

In contemporary molecular dynamics research on boiling phenomena, the multiscale approach with an innovative three-region model (molecular dynamics, coarse-grained, continuum) is considered. As shown in Fig. 5.1, a multiscale three-region model is proposed where an additional microscale region will be sandwiched between the nano region and the continuum macro region to ensure a smooth transition for accurate results. Molecular dynamics simulation will be applied in the nano region, the coarse-grained (CG) approach will be applied in the micro region and continuum approaches like finite element method (FEM) or finite volume method (FVM) could be applied in the macro region.

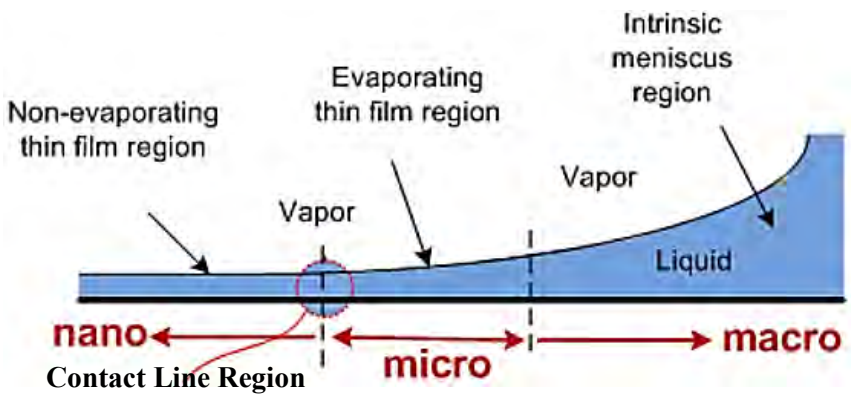

Fig. 5.1. Schematic showing multi-scale method of solution.

Though numerous studies on evaporation and explosive boiling of thin film liquid has been done in the past, unfortunately, still the exact mechanism(s) for these phenomena are not yet fully understood. Therefore, we would strongly suggest more extensive study of this problem using molecular dynamics simulation.

REFERENCES

1. P. L. Woodfield, M. Monde, A.K. Mozumdar, Observations of high temperature impinging-jet boiling phenomena, Int. J. Heat Mass Trans. 48(25) , pp. 2032-2041, 2005.
2. M. A. Islam, M. Monde, P. L. Woodfield, Y. Mitsutake, Jet impingement quenching phenomena for hot surfaces well above the limiting temperature for solid–liquid contact, Int. J. Heat Mass Trans. 51(5), pp. 1226-1237, 2008.
3. P. Argyropoulos, K. Scott, W. M. Taama, Carbon dioxide evolution patterns in direct methanol fuel cells, Electrochem. Acta, 44, pp. 3575–3584, 1999.
4. P. Argyropoulos, K. Scott, W. M. Taama, Gas evolution and power performance in direct methanol fuel cells, J. Appl. Electrochem., 29, pp. 661–669, 1999.
5. A. Asai, Application of nucleation theory to the design of bubble jet printers, Japan J. Appl. Phys., 28(5), pp. 909–915, 1989.
6. C. T. Avedisian, W. S. Osborne, F. D. McLeod, C. M. Curley, Measuring bubble nucleation temperature on the surface of a rapidly heated thermal inkjet heater immersed in a pool of water, Proc. R. Soc. Lond. A, 455, pp. 3875–3899, 1999.
7. Y. Hong, N. Ashgriz, J. Andrews, Experimental study of bubble dynamics on a micro heater induced by pulse heating, J. Heat Trans., 126, pp. 259–271, 2004.
8. V. P. Carey, Thermodynamic analysis of the intrinsic stability of superheated liquid in a micromechanical actuator with elastic walls, Microscale Thermophys. Eng., 4, pp. 109–123, 2000.
9. E. Zwaan, S. Le Gac, K.C. D. Ohl, Controlled cavitation in microfluidic systems, Phys. Rev. Lett., 98, pp. 254501, 2007.
10. K. Okuyama, R. Takehara, Y. Iida, J.H. Kim, Pumping action by boiling propagation in a microchannel, Microscale Thermophys. Eng., 9, pp. 119–135, 2005.
11. M. P. Brenner, S. Hilgenfeldt, D. Lohse, Single-bubble sonoluminescence, Rev. Mod. Phys., 74(2), pp. 425–484, 2002.
12. D. Hammer, L. Frommhold, Sonoluminescence: How bubbles glow, J. Mod. Optic., 48, pp. 239–237, 2001.
13. R. E. Aguilera, Passive CPU cooling and LCD heating for a laptop computer, Patent US 5606341 A, 1997.
14. V. G. Pastukhov, Y. F. Maidanik, C. V. Vershinin, M. A. Korukov, Miniature loop heat pipes for electronics cooling, Appl. Therm. Eng., 23, pp. 1125–1135, 2003.
15. J. C. Puckett, Two-phase constant pressure closed-loop water cooling system for a heat producing device, Patent US 5940270 A, 1999.
16. V.P. Skripov, Metastable Liquids, Halsted, New York, pp. 312, 1974.
17. O.A. Kabov, E. Ya, D.V. Zaitsev, Cooling technique based on evaporation of thin and ultra-thin liquid films, ITHERM 2008, pp. 520-527, 2008.

18. S. Georgiou, Laser cleaning methodologies of polymer substrates, Adv. Polym. Sci. 168, pp. 1-49, 2004.

19. T. Juhasz, X.H. Hu, L. Turi, Z. Bor, Dynamics of shock waves and cavitation bubbles generated by picosecond laser pulses in corneal tissue and water, Lasers Surg. Med. 15(1), pp. 91-98, 1994.

20. R. Bhardwaj, X. Fang, D. Attinger, Pattern formation during the evaporation of a colloidal nanoliter drop: a numerical and experimental study, New J. Phys. 11(7), pp. 075020 (2009).

21. T. Kunugi, Heat transfer enhancement by nano-scale structure formed on surface: experimental and molecular dynamics study, in: Proceedings of the First International Symposium on Micro and Nano Technology (ISMNT), No. XXV II-3-01, 2004.

22. T. Kunugi, K. Muko, New Heat-Exchange and Heat-transfer Methods between Solids and Fluids, Patent# 2002-297088, JP.

23. E. Hosono, S. Fujihara, I. Honma, H. Zhou, Superhydrophobic perpendicular nanopin film by the bottom-up process, J. American Chem. Society,127(39), pp.13458–13459, 2005.

24. G. Nagayama, S. Shi-iki, T. Tsuruta, Effects of naostructures on surface wettability: a molecular dynamics study, Trans. Japan Society of Mechanical Engg. B 73 (728), pp.1084–1091, 2007.

25. M. N. Hasan, M. Monde, Y. Mitsutake, Model for boiling explosion during rapid liquid heating, Int. J. Heat Mass Trans. 54, pp. 2844-2853, 2011.

26. M. N. Hasan, M. Monde, Y. Mitsutake, Homogeneous nucleation boiling during jet impingement quench of hot surfaces above thermodynamic limiting temperature, Int. J. Heat Mass Trans. 54, pp. 2837-2843, 2011.

27. K. Yasuoka, M. Matsumoto, Molecular dynamics of homogeneous nucleation in the vapor phase. I. Lennard-Jones fluid, J. Chem. Phys. 109 (19), pp. 8451–8462, 1998.

28. K. Yasuoka, M. Matsumoto, Molecular dynamics of homogeneous nucleation in the vapor phase. II. Water, J. Chem. Phys. 109 (19), pp. 8463–8470, 1998.

29. T. Kinjo, M. Matsumoto, Cavitation processes and negative pressure, Fluid Phase Equilibria 144 (1–2), pp. 343–350, 1998.

30. T. Kimura, S. Maruyama, Molecular dynamics simulation of heterogeneous nucleation of a liquid droplet on a solid surface, Microscale Thermophys. Engg. 6, pp. 3-13, 2002.

31. G. Nagayama, T. Tsuruta, P. Cheng, Molecular dynamics simulation on bubble formation in a nanochannel, Int. J. Heat Mass Trans. 49, pp. 4437–4443, 2006.

32. J. Yu, H. Wang, A molecular dynamics investigation on evaporation of thin liquid films, Int. J. Heat Mass Transfer 55, pp. 1218-1225, 2012.

33. M. Sekine, K. Yasuokaa,, T. Kinjob, M. Matsumoto, Liquid–vapor nucleation simulation of Lennard-Jones fluid by molecular dynamics method, Fluid Dyn. Research 40, pp. 597–605, 2008.

34. B. R. Novak, E. J. Maginn, M. J. McCready, Comparison of heterogeneous and homogeneous bubble nucleation using molecular simulations, Phys. Rev. B 75 (7),pp. (085413)1-11, 2007.

35. Y.W. Wu, C. Pan, Molecular dynamics simulation of thin film evaporation of Lennard–Jones liquid, Nanoscale Microscale Thermophys. 10, pp. 157–170, 2006.

36. P. Yi, D. Poulikakos, J. Walther, G. Yadigaroglu, Molecular dynamics simulation of vaporization of an ultra-thin liquid argon layer on a surface, Int. J. Heat Mass Trans. 45, pp. 2087–2100, 2002.

37. X. Gu, H.M. Urbassek, Atomic dynamics of explosive boiling of liquid-argon films, Appl. Phys. B 81, pp. 675–679, 2005.

38. T. Yamamoto, M. Matsumoto, Initial stage of nucleate boiling: molecular dynamics investigation, J. Therm. Sci. Technol. Jpn. 7, pp. 334–349, 2012.

39. S.C. Maroo, J.N. Chung, Molecular dynamic simulation of platinum heater and associated nano-scale liquid argon film evaporation and colloidal adsorption characteristics, J. Colloid Interface Sci. 328, pp. 134–146, 2008.

40. A.K.M.M. Morshed, Taitan C. Paul, Jamil A. Khan, Effect of nanostructures on evaporation and explosive boiling of thin liquid films: a molecular dynamics study, Applied Physics A 105, pp. 445-451, 2011.

41. H.R. Seyf, Y. Zhang, Molecular Dynamics Simulation of Normal and Explosive Boiling on Nanostructured Surface, ASME J. Heat Transfer 213 (135) 121503, pp. 1-8, (2013).

42. H.R. Seyf, Y. Zhang, Effect of nanotextured array of conical features on explosive boiling over a flat substrate: A nonequilibrium molecular dynamics study, Int. J. Heat Mass Transfer 66, pp. 613-624, 2013.

43. S. Maruyama, T. Kimura, A molecular dynamics simulation of a bubble nucleation on solid surface, Int. J. Heat Technol. 18, pp. 69–74, 2000.

44. S.H. Park, J.G. Weng, C.L. Tien, A molecular dynamics study on surface tension of microbubbles, Int. J. Heat Mass Transfer 44, pp. 1849–1856, 2001.

45. G. Nagayama, P. Cheng, Effects of interface wettability on microscale flow by molecular dynamics simulation, Int. J. Heat Mass Transfer 47, pp. 501–513, 2004.

46. A. Hens, R. Agarwal, G. Biswas, Nanoscale study of boiling and evaporation in a liquid Ar film on a Pt heater using molecular dynamics simulation, Int. J. Heat Mass Transfer 71, pp. 303-312, 2014.

47. W. R. Gambill, and J. H. Lienhard, An upper bound for the critical boiling heat flux, J. Heat Transfer, 111, pp. 815-818, 1989.

48. B. J. Alder, T. E. Wainwright, Phase transition for a hard sphere system, J. Chem. Phys. 27, pp. 1208, 1957.

49. B. J. Alder, T. E. Wainwright, Studies in molecular dynamics. I. General method, J. Chem. Phys. 31, pp. 459, 1959.

50. M.P. Allen, T.J. Tildesley, Computer simulation of liquids, Oxford Science Publications, 1989.

51. D. Frenkel, B. Smit, Understanding molecular dynamics simulation, Academic press. San diego, 2002.

52. RJ. Sadus, Molecular simulation of fluids, Amsterdam: Elsevier Science, pp. 552, 1999.

53. S. Plimpton, Fast parallel algorithms for short-range molecular dynamics, J. Comput. Phys. 117, pp. 1-19, 1995.

54. W. Humphrey, A. Dalke, K. Schulten, VMD: visual molecular dynamics, J. Mol. Graph. Model. 14(1), pp. 33-38, 1996.

55. J. M. Haile, Molecular dynamics dimulation, Wiley, New York, 1992.

56. S. Maruyama, Molecular dynamics method for microscale heat transfer, Adv. in Num. Heat Trans. 2, pp. 189-226, 2000.

57. T. Ohara, Molecular dynamics study in microscale thermophysical engineering: Current activities and future in Japan, Micro. Thermophys. Eng. 4(4), pp. 213-221, 2000.

58. A. Majumdar, Nanoengineering: Promises and challenges, Micro. Thermophys. Eng. 4(2), pp. 77-82, 2000.

59. J.E. Lennard-Jones, A.F. Devonshire, Philos. Trans. R. Soc. Lond. Ser. A, Math. Phys. Sci. 163, pp. 53-70, 1937.

60. B.A. Younglove, H.J.M. Hanley, The viscosity and thermal conductivity coefficients of gaseous and liquid argon, J. Phys. Chem. 15(4), pp. 1323-1335, 1986.

61. D. A. Kofke, Direct evaluation of phase coexistence by molecular simulation via integration along the saturation line, J. Chem. Phys. 98, pp. 4149-4162, 1993.

62. Y. Zou, X. Huai, L. Lin, Molecular dynamics simulation for homogeneous nucleation of water and liquid nitrogen in explosive boiling, App. Therm. Engg. 30, pp. 859–863, 2010.

63. Y. Mao, Y. Zhang, Molecular dynamics simulation on rapid boiling of water on a hot copper plate, App. Therm. Engg. 62, pp. 607-612, 2014.

64. Y. Dou, L. V. Zhigilei, N. Winograd, B. J. Garrison, Explosive boiling of water films adjacent to heated surfaces: A Microscopic Description, J. Phys. Chem. A, 105, pp. 2748-2755, 2001.

65. M. Baskes, S. Murray, Daw, Embedded–atom method; Derivation and application to impurities, surfaces, and other defects in metals, Phys. Rev. B 29(12), pp. 6443-6453, 1984.

66. S. Foiles, Daw, S. Murray, The embedded–atom method: A review of theory and applications, Mat. Sci. and Engr. Rep. 9(7-8), pp. 251, 1993.

67. F. Ercoslessi, M. Parinello, E. Tosatti , Simulation of gold in the glue model, Phil. Mag. A 58, pp. 213-226, 1998.

68. J. Tersoff, New empirical approach for the structure and energy of covalent systems, Phys. Rev. B 37, pp. 6991, 1988.

69. D. W. Brenner, Empirical potential for hydrocarbons for use in simulating the chemical vapor deposition of diamond films, Phys. Rev. B 42(15), pp. 9498, 1990.

70. R. Car, M. Parinello, Unified approach for molecular dynamics and density-functional theory, Phys. Rev. Let. 55(22), pp. 2471-2474, 1985.

71. P.M. Morse, Diatomic molecules according to the wave mechanics. II. Vibrational levels, Phys. Rev. 34, pp. 57-64, 1929.

72. R.A. Buckingham, The classical equation of state of gaseous helium, neon and argon, Proc. Royal Soc. London 168, pp. 264-283, 1938.

73. F. Stillinger, T.A. Weber, Computer simulation of local order in condensed phases of silicon, Phys. Rev. B 31, pp. 5262, 1985.

74. l. Verlet, Computer experiments on classical fluids. I. Thermodynamical properties of Lennard-Jones molecules, Phys. Rev. 159, pp. 98-103, 1967.

75. W.C. Swope, H.C. Andersen, P.H. Berens, K.R. Wilson, A computer simulation method for the calculation of equilibrium constants for the formation of physical clusters of molecules: Application to small water clusters, J. Chem. Phys. 76, pp. 637, 1982.